INFLUENCE OF THE TEST SECTION TYPE ON THE AIRFOIL TRAILING EDGE AEROACOUSTIC TEST.

MSc thesis, Chiel Koenjer.

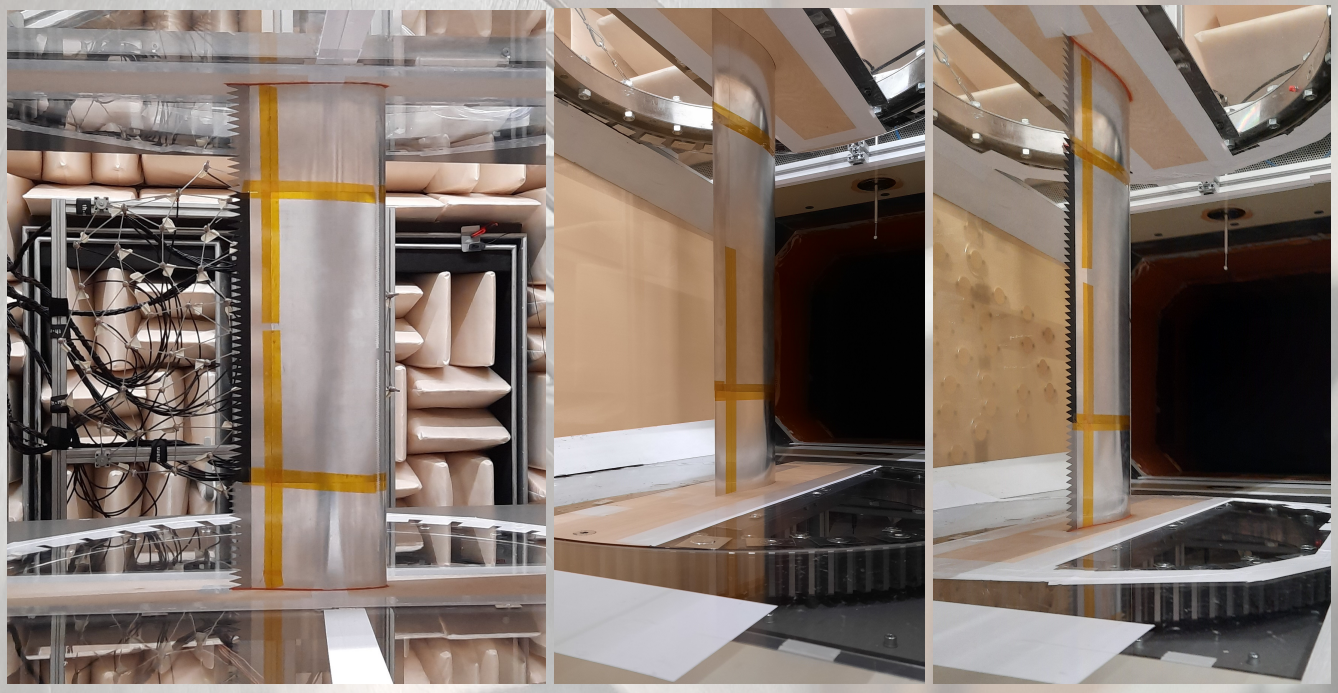

Document no. 395

UNIVERSITY
OF TWENTE.

INFLUENCE OF THE TEST SECTION TYPE ON THE AIRFOIL TRAILING EDGE AEROACOUSTIC TEST.

MSc thesis
Version 1

C. F. J. Koenjer
s2192047

A Master thesis is presented,
in fulfilment of the requirements for the degree of

Master of Science
in Sustainable Energy Technology

Supervisor: dr. L.D. de Santana[1]
Daily supervisor: ir. L. Botero Bolivar[2]

UNIVERSITY OF TWENTE.

University of Twente (NL)
Engineering Technology Faculty
Engineering Fluid Dynamics Research Group
August 2021

[1]Assistant Professor in the Engineering Fluid Dynamics Research Group, at the University of Twente.
[2]PhD candidate Engineering Fluid Dynamics Research Group, at the University of Twente.

Preface and Acknowledgements

This thesis is written to finalize my Master of Science in Sustainable Energy Technology (SET) at the University of Twente (UT), faculty of Engineering Technology in the Engineering Fluid Dynamics (EFD) group.

After finishing my Bachelor of Mechanical Engineering at the University of Applied Sciences, with an internship about drinking water installations in Nepal powered by sustainable energy resources. The opportunities for renewable energy intrigued me, enrolling via a pre-master program in the Master of SET. Here I was introduced to the engineering fundamentals for different sustainable energy technologies, among them wind energy. I chose my elective courses towards a path of a wind energy related thesis, eventually aeroacoustics (courses; Wind Energy, Fluid Mechanics of Turbo machines, Aeroacoustics, Acoustics Engineering).

The first ideas for a wind energy related MSc thesis was the design, manufacture, and testing of a new airfoil for the UT wind tunnel. Due to the opportunity to borrow a suitable airfoil from the University of Delft, a different approach for my thesis was set up. A thesis designed to assess the influence of the test sections in the UT wind tunnel, in executed airfoil experiments. This collaboration with the Delft University also gives the opportunity to compare the results of the same airfoil in multiple aeroacoustic wind tunnels. This project started on the 30th of November 2020 during the corona pandemic, the first step was to make a plan of approach and set the activities. Then an in depth literature study was executed related to the aerodynamic and aeroacoustic principles, followed by some simulation in XFOIL. After some trouble with the shipping of the airfoil from Delft, experiments could be executed. From the 22d of February up to the 6th of April, trailing edge noise experiments are conducted with three airfoil in the aeroacoustic wind tunnel at the UT. With these far - and near field noise levels, the influence of the test section is assessed during trailing edge noise measurements.

Furthermore I would like to thank all the people who helped me during this project. First of all my daily supervisor ir. Laura Botero Bolivar for her knowledge and guidance throughout the project, even when she was not in Netherlands and living in a different time zone. dr. Leandro de Santana for his time and effort to arrange this thesis and his overall supervision during this project. Marijn Sanders and ir. Fernanda Leticia Dos Santos for their support during the executed measurements and their knowledge regarding aeroacoustics. Furthermore I want to thank all the technical support staff members, and dr. ir. Jim Kok and prof. dr. ir Kees Venner for the opportunity to execute this MSc thesis within this faculty.

Abstract

Social resilience against wind energy asks for academic, aeroacoustic research to reduce noise emissions. Airfoil aeroacoustic tests, focused on trailing edge noise, are executed in aeroacoustic wind tunnels with multiple test section types. The methodology gives understanding about: aeroacoustic airfoil phenomena, underlying aerodynamics, fluid mechanics, and the parameters influencing the noise, supported by XFOIL simulations. Literature about noise reduction techniques is given, noise reducing methods are designed, and resulting in a maximum background noise reduction of 12 dB. Test section influence on the near - and far field noise is assessed, reduced and compared. Experiments are executed with three different airfoils (NACA0012, NACA0018, and NACA63018) in three test section types (Open-Jet -, Hybrid -, and Closed Test Section) in the A2 aeroacoustic wind tunnel of the University of Twente. In conclusion, the influence of the test section type in trailing edge noise measurements is small. Background noise may differ, but is not influencing the results for the near field in any way at zero Angle of Attack (AoA). Far field noise results at AoA=0° show minor deviations in the obtained noise reduction, mainly present in the Closed Test Section for higher free stream velocities. Regarding non-zero Angles of Attack, the test section influence is increased for both the near - and far field. The Closed Test Section is not suitable for serrated airfoil far field noise measurements, at non-zero Angles of Attack.

Keywords: Aeroacoustic - Airfoil - Noise - Test Section - Trailing Edge

Contents

Nomenclature

Capital letters

C_D	Drag coefficient [-]
C_L	Lift coefficient [-]
C_M	Momentum coefficient [-]
C_P	Pressure coefficient [-]
D	Drag force $[N]$
L	Lift force $[N]$
M	Momentum $[Nm]$
U	Velocity $[m/s]$
U_∞	Free stream velocity $[m/s]$
q_∞	Free stream dynamic pressure $[Pa]$

Small letters

c	Chord length $[m]$
c_o	Speed of sound $[m/s]$
f	Frequency $[Hz]$
p	Pressure $[Pa]$
p_∞	Free stream pressure $[Pa]$
s	Coordinate along the airfoil surface $[m]$
t	Time [s]
$\underline{v}$	Velocity vector $[m/s]$

Greek Symbols

α	Angle of attack [°]
δ	Boundary-layer disturbance thickness $[m]$
δ^*	Boundary-layer displacement thickness $[m]$
θ	Boundary-layer momentum thickness $[m]$
μ	Dynamic viscosity $[Pa \cdot s]$
ν	Kinematic viscosity $[m^2/s]$
ρ	Density $[kg/m]$
τ	Shear stress $[N/m^2]$
Φ	Wall pressure spectrum $[dB]$
ω	Angular frequency $[rad/s]$

Other

AoA	Angle of attack [°]
CSM	Cross Spectral Matrix
M	Mach number [-]
Re	Reynolds number [-]
ROI	Region Of Interest
SPI	Source Power Integration
SPL	Sound Pressure Level $[dB]$
SPW	Sound Power Level $[dB]$
St	Strouhal number [-]

1 Introduction

The transition from fossil fuels to renewable energy resources has led to a tremendous growth of the installed wind energy capacity. The cross sectional area of a wind turbine blade is designed in such way that the incoming flow diverts in such a way that it results in a force on the blade. The component of this force in the rotor plane is what makes the blade turn, and eventually electrical energy is harvested. As article two of the Paris Agreement states, the global average temperature must be hold well below 2 °C above pre-industrial levels [1]. There are many routes to decarbonisation, one of the routes given by the International Energy Agency (IEA) estimates a wind energy share of 29% in the regional electricity mixes for the 2 °C case in 2050 for Europe (portfolios to decarbonise the power sector depend on regional challenges and opportunities)[2]. The installed capacity of wind energy is growing rapidly, but despite a European growth of 27% in 2019 compared with 2018, the wind energy sector is not fully on track to reach the levels envisioned in the sustainable developments scenarios. In 2019 only 15% of the total electricity in Europe comes from wind energy [3]. This suggest that a lot more capacity for wind energy must be installed in the next decades to achieve these goals. This also means that onshore wind parks will and must be installed in the near future, also in urban areas.

However, the noise from wind turbines is an important hindrance for widespread application and causes social resilience. Research must be conducted on the noise propagated from a wind turbine blade. This to understand the aerodynamic - and acoustic phenomena occurring, relating different parameters to the acoustic noise sources, and apply noise reduction techniques in future prototypes and wind turbines. This to oblige with current and future legislation's, and to secure human health from excessive noise emissions. The aeroacoustic wind tunnel at the University of Twente is used for acoustic experiments on small scale blades (airfoils). The most dominant acoustic phenomena of an airfoil is trailing edge noise, coming from the downstream extremity and it widely studied in aeroacoustic wind tunnels. During previous so-called trailing edge noise measurements at the UT, results were contaminated by background noise coming from the wind tunnel itself, proper results could not be obtained. The origin of the unwanted noise source must be obtained, and noise reduction techniques must be applied to be able to execute accurate experiments. In this way, the influence of the test section in trailing edge noise measurements can be assessed and reduced. Further in-depth research regarding trailing edge noise and potential noise reducing techniques can be tested, lowering the barriers for application in urban areas.

The A2 aeroacoustic wind tunnel at the University of Twente has three different test sections, the Closed Test Section (CTS), where the flight conditions are the most optimal, but unwanted boundary layer noise is contaminating the experiments. The Open-Jet Test Section (OTS), circumvents this unwanted noise source but results in a diverged airflow reducing the aerodynamic performance. Third, the Hybrid Test Section (HTS), uses the CTS with an tensioned Kevlar cloth as side panels, allowing the sound waves to pass through this cloth but keeping the airflow inside. Trailing edge noise experiments will be conducted with three airfoils in all three test sections for zero - and non-zero angles of attack. Conclusions will me made to define the influence of the test sections, and prescribe the most optimal test section under certain conditions.

The outline of this MSc thesis is structured in four main parts; theoretical background, methodology, results and conclusions/discussion. Part I, gives relevant theoretical literature about fluid mechanics, airfoil aerodynamics and aeroacoustics. After that, the different airfoil self-noise types substantiated by aerodynamic simulations in XFOIL are shown. In the methodology (Part II), the experimental set up is explained, and noise reduction techniques for the unwanted noise source in the UT wind tunnel are designed. In the end, the post processing algorithm related to the beamforming technique is given. In Part III, all relevant results are given, including: background noise comparison, wall pressure spectrum and far field noise (for multiple angles of attack and different velocities). In this way, the influence of the test section type can be assessed and is summarized in Part IV, conclusion and discussion. All parts are structured by chapters and paragraphs.

PART I, Theoretical Background

2 Theoretical Background

As already mentioned, the background noise of the aeroacoustic wind tunnel at the UT was contaminating the so-called trailing edge noise measurements. Proper results could not be obtained. This MSc thesis is designed to assess the influence of the three different test sections from these experiments (test section types explained in Chapter 3.1). The cross sectional area of a blade is called an *airfoil*, experiments will be conducted on three different airfoils, namely the NACA0012, NACA0018 and NACA63018. These profiles originate from aircraft wings developed by the National Advisory Committee for Aeronautics (NACA). In the beginning, most of the airfoil geometries where based on empirical methods, where the airfoils where tested and adjusted repeatedly, but NACA took a different approach.

Furthermore, to understand the acoustic phenomena occurring on an airfoil, first of all the aerodynamic principles and underlying fluid mechanics must be know. When this is summarized, the different types of airfoil self-noise can be related to the aerodynamic principles and the parameters influencing these phenomena. In this way, the origin of the noise can be determined, and parameters can be adapted to stimulate certain desired aerodynamic phenomena, and reduce the noise. In this way the influence of the test section during trailing edge noise measurements can be assessed, understood and reduced. This will all be explained in the theoretical background. First, information about the airfoils will be discussed.

2.1 Airfoil Nomenclature

NACA used a more systematic way of designing a lot of airfoils (specifically for flows with a high Reynolds numbers), based on the combination of two concepts: the *mean camber line* and the *thickness distribution* . The mean camber line is the curved line between the front and back extremities (halfway between the top and bottom, see Figure 2). In aerodynamics better known as the *leading edge* (LE) and *trailing edge* (TE) respectively. The straight line between these points is called the *chord line*, and the dimension of this line is called the *chord* (c). In this case the bottom side is referred to as the *pressure side* and the top is called the *suction side*, this because the airfoil generates a positive lift (upwards) due to the incoming velocity (U_{ref}). The Angle of Attack (AoA or α), is defined as the angle between the incoming velocity and the chord line.

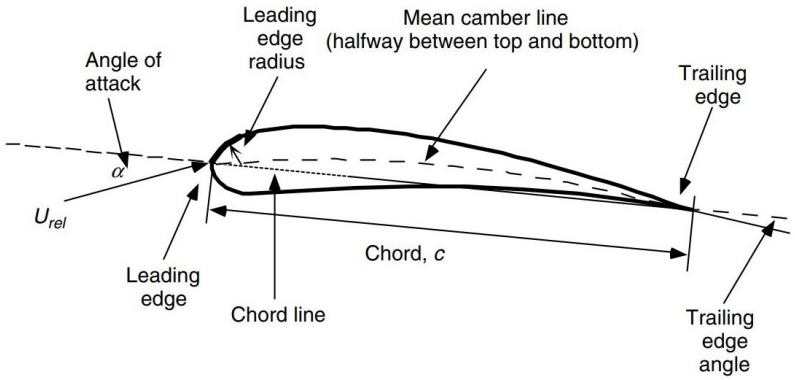

Figure 2: Airfoil nomenclature [4].

NACA 4-digit airfoils

Due to the iterative design process of airfoils by NACA, the airfoils are distinguished into different families. The four-digit series is the first family that has been designed, fabricated and tested by NACA. The first digit is describing the maximum camber as percentage of the chord, the second describes the distance of maximum camber from the airfoil leading edge in tenths of the chord. The last two digits are describing the maximum thickness of the airfoil as percent of the chord. The NACA0012 and NACA0018 are both four-digit airfoils, the notation indicates

that both are symmetrical airfoils with no camber, and a thickness of 12% and 18% of the chords respectively. The geometry of a four-digit symmetrical airfoil can be described as the relation in (2.1.1). Here y_t is the half thickness of the airfoil, t the the maximum thickness as a fraction of the chord (last two digits in this NACA type), and x the position along the chord. The geometry of the symmetrical airfoils are given in Figure 3.

$$y_t = 5t \left[0.2969\sqrt{x} - 0.1260x - 0.3516x^2 + 0.2843x^3 - 0.1036x^4\right] \tag{2.1.1}$$

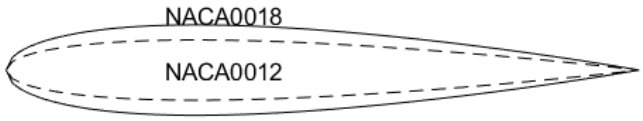

Figure 3: Contour of the NACA 4-digit airfoils.

NACA63$_3$-018
Experience with the 2- to 5 series showed undesirable effects, so improved airfoil geometries must be designed. Overall these early series generally showed relatively low C_L values, and in many cases were designed to maintain the laminar flow over the airfoil, what is not required up to that level in practice. Although these series showed relatively low drag coefficients near the designed lift condition ($C_{L.d}$) when the surface was considered as smooth. When rough, the C_D values became disadvantageously large, particular when $C_L > C_{L.d}$. Revisions of the previously generate airfoil families where designed, with the goal to obtain a desirable drag, critical Mach number, and maximum lift characteristics [5]. The notation of this airfoil series consists out of six integers; • the 1^{st} indicates the series number, • the second the position of minimum pressure, in tenths of the chord, • a possible subscript gives the range of C_L in tenths above and below $C_{L.d}$ in which favorable pressure gradients exist (on both surfaces), • the third integer gives the lift coefficient, • and the last two numbers indicate the maximum thickness as percentage of the chord. The 63018 is a symmetrical, well studied airfoil. The contour of this airfoil is given in Figure 4, it is almost identical to the NACA0018 only the shape of the LE and TE deviates slightly. This airfoil is chosen because it shows some non-stationary behaviour, for example it has a not well determined hysteresis effect. Resulting from the transitional behavior of the downwind surface shear layer and its ability to re-attach to the airfoil surface affecting the location of turbulent separation. This could lead to a hysteresis loop in the lift curve.

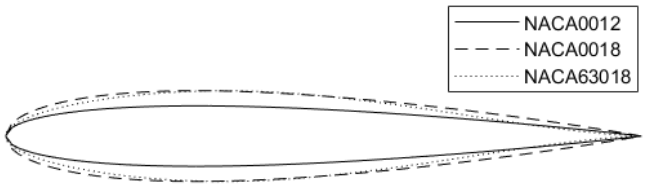

Figure 4: Contour of the NACA profiles.

Further information about the airfoils and the experimental set up are discussed in Chapter 2.7.

2.2 Trailing Edge Noise

The noise of a large wind turbine is dominated by the broadband noise of the blades outer parts interacting with the surrounded flowing medium [6]. The main noise source is trailing edge noise, occurring at high Reynolds numbers. This self noise mechanism is caused by a turbulent boundary layer which generates surface pressure fluctuations, because of the discontinuity at the TE this is scattered to the far field as noise. This boundary layer is developed along the blade surface and remains attached up to the the trailing edge. When these turbulent boundary layer structures (*eddies*) pass the trailing edge, their sound is scattered causing broadband noise (Figure 5). This turbulent-boundary-layer-trailing-edge noise or briefly trailing edge noise dominates the wind turbine noise for modern large scale wind turbines.

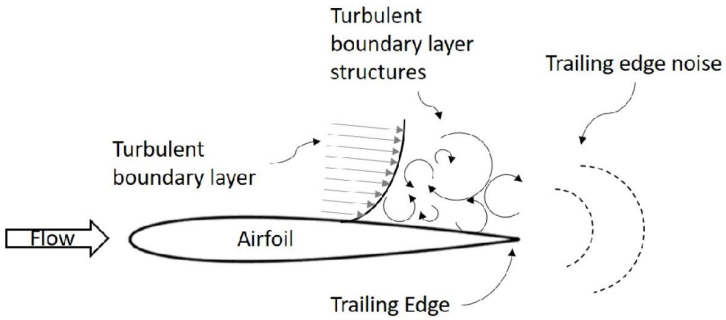

Figure 5: Schematic view of turbulent-boundary-layer-trailing-edge noise. [7]

2.3 Exit Nozzle Noise

In previously executed trailing edge noise measurements in the wind tunnel at the UT, results where poor due to the fact that the background noise was too high. Resulting in a contaminated output of the noise levels. This problem must be solved to quantify and locate the noise coming from the airfoil, and to assess the influence of the different test sections. Information about the experimental set up and the different test sections will be given in Chapter 3.1. With an acoustic camera, it was assessed that noise was coming from the flange coupling of the exit nozzle of the closed test section. Figure 6 shows the wooden flange coupling, connecting the test sections (marked in red). Multiple solution to circumvent this unwanted noise are designed.

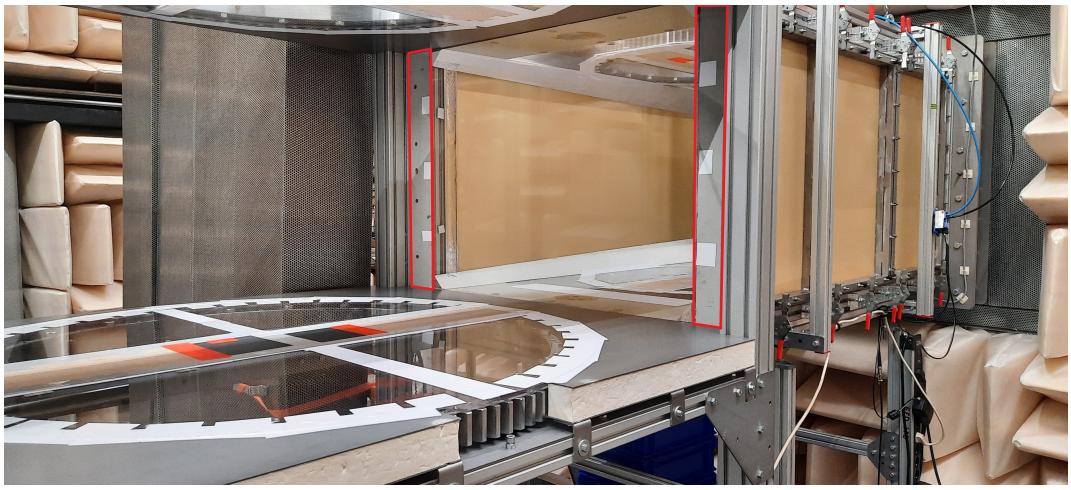

Figure 6: Photo of the UT wind tunnel, flange coupling marked in red connecting the test sections.

2.4 Fluid Mechanics

Fluid mechanics is the study of forces and flow within fluids. First, the general conservation laws are given, second the most important dimensionless numbers and their relevance are explained. Then, the boundary layer theory is explained, and important relations and corresponding jargon are given. At last, the principles of the transition from laminar to turbulent flow are discussed. Text books on fluid mechanics are [8] and [9], other relevant literature for this section is [10] and [11].

2.4.1 Conservation Laws

The *mass conservation law* in 3D and vector notation is given in (2.4.1), here ρ is the density and $\underline{v}$ the velocity vector in the x, y and z directions ($i, j, k \in [x, y, z]$). Here the capital D denotes the *material derivative*, the time derivative when following a particle. The material derivative consists of two terms, a local time derivative and a convective term $\left(\frac{D\rho}{Dt} = \frac{\partial \rho}{\partial t} + \underline{v} \cdot \nabla \rho\right)$ [10]. So the change of density over time (when following a particle), plus the density multiplied with the velocity divergence must be zero, then mass is conserved.

$$\frac{D\rho}{Dt} + \rho \nabla \cdot \underline{v} = 0 \tag{2.4.1}$$

The *momentum conservation law* is given in (2.4.2). Here ∇p is the gradient of the pressure, $\underline{\sigma}'$ the deviatoric stress tensor (Newtonian fluid [3]), and $\underline{g}$ the gravitational force. The deviatoric stress tensor excludes the hydrostatic part, the pressure. Here μ is the dynamic viscosity of the fluid, and δ_{ij} the Kronecker symbol where $\delta_{ij} = 1$ if $i = j$ and 0 otherwise.

$$\begin{aligned} \rho \tfrac{D\underline{v}}{Dt} &= -\nabla p + \nabla \cdot \underline{\sigma}' + \rho \underline{g} \\ \sigma_{ij} &= -p\delta_{ij} + \sigma'_{ij} \\ \sigma'_{ij} &= \mu \left(\tfrac{\partial v_i}{\partial x_j} + \tfrac{\partial v_j}{\partial x_i} - \tfrac{2}{3} \tfrac{\partial v_k}{\partial x_k} \delta_{ij} \right) \end{aligned} \tag{2.4.2}$$

The *angular momentum conservation law* is given in (2.4.3). Which indicate that the deviatoric stress tensor and the total stress (σ) are both symmetrical for a Newtonian fluid.

$$\underline{\sigma}' = \underline{\sigma}'^T \quad \sigma'_{ij} = \sigma'_{ji} \tag{2.4.3}$$

The *energy conservation law* is given in (2.4.4), here T is the temperature, $\frac{Ds}{Dt}$ the entropy time derivative (measure of irreversibility) and k the thermal conductivity. The term on the left deals with the entropy deviation, the first therm on the right with the thermal conductivity and the last term deals with the energy dissipation due to viscosity.

$$\rho T \frac{Ds}{Dt} = k \nabla^2 T + \sigma'_{ji} \frac{\partial v_i}{\partial x_j} \tag{2.4.4}$$

These conservation laws are the basis for many aeroacoustic and aerodynamic formulas.

[3] Fluids where the shear stress is directly proportional to the rate of deformation, cf. water, air and gasoline (under normal conditions).

2.4.2 Dimensionless numbers

The general use of non-dimensional values is useful in the comparison of similar experiments with distinct quantities. In fluid mechanics there are many significant dimensionless groups, in this section the most relevant dimensionless numbers are discussed. Understanding their physical significance also gives insight into the different phenomena in Fluid Mechanics.

Reynolds
The *Reynolds number* (Re) describes the ratio of inertial forces (the resistance of a body to a change in velocity) to viscous forces, indicating the amount of turbulence. The relation is given in (2.4.5), here U is the velocity of the flowing medium, L the characteristic length (for example the chord of an airfoil), μ the dynamic viscosity, and ν the kinematic viscosity.

$$Re = \frac{\rho U L}{\mu} = \frac{UL}{\nu} = \frac{\text{inertial forces}}{\text{viscous forces}} \tag{2.4.5}$$

The Reynolds number is an important indicator corresponding to the transition of the boundary layer over an airfoil, and gives an indication if the flow is laminar or turbulent. Flows with a high Re are often turbulent, explained in Chapter 2.4.4.

Strouhal
The *Strouhal number* (St) is a dimensionless number describing the oscillation in a flowing medium. It gives the ratio of inertial forces due to the unsteadiness of the flow, to the inertial forces due to the changes in velocity. The relation is given in (2.4.6), here f is the frequency of vortex shedding, and U_∞ the velocity denoted by infinity referring to an undisturbed stream.

$$St = \frac{fL}{U_\infty} \tag{2.4.6}$$

The vortex shedding frequency can be determined experimentally by hot wire measurements. So with the Strouhal number, the origin of the oscillation in the flow can be determined.

Mach
The *Mach Number* (M) gives the ratio of the flow velocity to the local speed of sound[4] (c_0), given in (2.4.7). Four different speed regimes can be identified using the Mach number, a *subsonic flow* has $M < 1$. A flow that is *supersonic* has $M > 1$, a *transonic flow* has mixed regions and a *hypersonic flow* is a highly supersonic flow where the rule of thumb is that $M > 5$.

$$M = \frac{U}{c_0} \tag{2.4.7}$$

Mach scaling is often used in noise prediction methods in aeroacoustics also used by Brooks [12], discussed in Section 2.7 in further depth. The next example is given to indicate the order of magnitude of the different dimensionless numbers related to airfoil experiments.

Example 1:
Regarding air at 25 °C this results in a value of $Re = 0.645 \cdot 10^6$ ($\rho = 1.184 kg/m^3$, $U = 10 m/s$, $L = 1m$ and $\mu = 18.37 \cdot 10^{-6} Pa \cdot s$)[a]. The frequency of vortex shedding (f) for a large range of Re, in a circular cylinder (tube) is approximately constant, so $St \approx 0.21$. Regarding to the flow over a solid body this is not true. With this velocity this results in a Mach Number of 0.0289 ($c_0 = 346.3 m/s$).

[a] Properties of air from https://www.engineeringtoolbox.com

[4] $c_0 = \sqrt{\gamma R T_\infty}$, where γ is the specific heat ratio $\left(\frac{c_p}{c_v}\right)$, R the specific gas constant, the denotation of zero refers to an ideal gas.

2.4.3 Boundary Layer Theory

When air is flowing over a solid wall, the interaction causes frictional forces on the surface, these tugging forces parallel to the surface are known as the *shear stress*. The fluid encounters a counter force resulting in a change of the velocity profile near the surface, decelerating the fluids motion. This is an important phenomena in viscous flows, the shear stress (τ) acting on a surface in a two dimensional plane can be given as the relation in (2.4.8) (Newton's law of friction).

$$\tau = \mu \frac{\partial u}{\partial y} \tag{2.4.8}$$

Characteristics of a boundary layer
To define the equations related to the behaviour inside of a boundary layer, certain steps and assumptions are made. Based on Abbot [5] the general Navier-Stokes Equations in 2D, with $\underline{u} = (u_x, u_y)^T$, for a steady motion, neglecting compressibility can be defined as,

$$\begin{aligned} u_x \frac{\partial u_x}{\partial x} + u_y \frac{\partial u_y}{\partial y} &= -\frac{1}{\rho}\frac{\partial p}{\partial x} + \frac{\mu}{\rho}\left(\frac{\partial^2 u_x}{\partial x^2} + \frac{\partial^2 u_x}{\partial y^2}\right) \\ u_x \frac{\partial u_y}{\partial x} + u_y \frac{\partial u_x}{\partial y} &= -\frac{1}{\rho}\frac{\partial p}{\partial y} + \frac{\mu}{\rho}\left(\frac{\partial^2 u_y}{\partial x^2} + \frac{\partial^2 u_y}{\partial y^2}\right) \end{aligned} \tag{2.4.9}$$

Hereby it assumed that $\frac{\partial p}{\partial y}$ is small, the influence of the second equation in (2.4.9) can be neglected. Prandtl states that the viscous effects can be assumed to be confined to a thin layer over the surface, this results in the *boundary layer equation for a laminar flow*,

$$u_x \frac{\partial u_x}{\partial x} + u_y \frac{\partial u_x}{\partial y} = -\frac{1}{\rho}\frac{\partial p}{\partial x} + \frac{\mu}{\rho}\frac{\partial^2 u_x}{\partial y^2} \tag{2.4.10}$$

Substituting relevant non-dimensionless variables in the previous equation, and simplification gives the simplified boundary layer equation. It seems that the viscosity is not directly present in this equation, but $\underline{u}(Re, \mu)$. It can be concluded that the shape of velocity distribution is independent of the Reynolds number (unless $p(Re)$).

$$\begin{aligned} x^* &= \tfrac{x}{c} & y^* &= \tfrac{y}{c}\sqrt{Re} \\ u_x^* &= \tfrac{u_x}{U_\infty} & u_y^* &= \tfrac{u_y}{U_\infty}\sqrt{Re} \\ p^* &= \tfrac{p}{\rho U_\infty^2} \end{aligned}$$

$$u_x^* \frac{\partial u_x^*}{\partial x^*} + u_y^* \frac{\partial u_x^*}{\partial y^*} = \frac{\partial p^*}{\partial x^*} + \frac{\partial^2 u_x^*}{\partial y^{*2}} \tag{2.4.11}$$

Boundary-layer disturbance thickness
A schematic representation of the boundary layer near a solid wall is given in Figure 7. The velocity at the surface always equals zero. The shear stress is at its largest at $x = 0$, where the gradient of the velocity in the y-direction is the highest, and is resulting in a thin *boundary-layer disturbance thickness* (δ). This is usually defined as the distance between the stationary surface, and the position where the velocity is within 1% of U_∞. The increase of δ over the surface occurs as the loss of momentum by the no-slip condition at the wall diffuses into the stream. In other words, as the fluid flows over the wall more and more fluid particles normal to the stream-wise direction (further away from the wall) are affected by the friction force of the stationary surface. Reducing $\frac{\partial u}{\partial y}$ and τ, which increase δ.

Because this boundary-layer disturbance thickness is experimentally hard to define, the thickness is often based on mass and momentum conservation. A first estimation (δ_{99}), and an approximate solution for the boundary layer disturbance thickness where the flow will be turbulent (δ_{tur}) is given in (2.4.12). In this relation x is the distance from the point where the boundary layer starts to develop.

$$\delta_{99} = 5.0\frac{x}{\sqrt{Re(x)}}, \quad \delta_{tur} \approx 0.37\frac{x}{Re(x)^{1.5}} \tag{2.4.12}$$

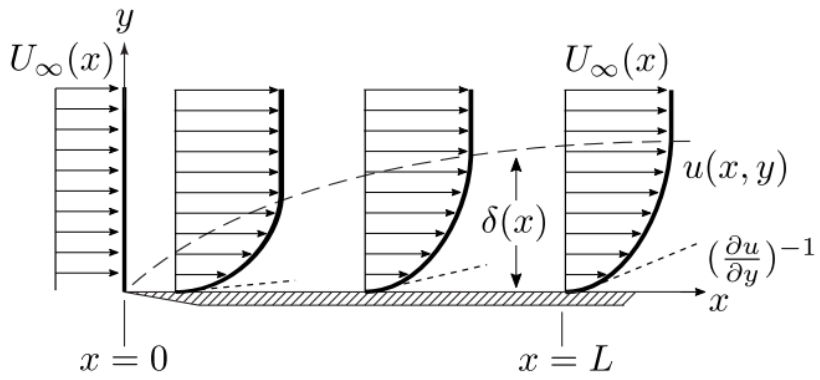

Figure 7: Representation of the boundary layer near a solid wall [13].

Boundary-layer displacement thickness
The presence of viscous forces results in a change of mass flow adjacent to the solid wall in comparison to the core mass-flow. This mass-flow (per unit depth) is given by $\int_0^\infty \rho u(x,y)\,dy$. The decrease in mass-flow rate, relative to the corresponding mass-flow rate of a uniform inviscid flow is given by $\int_0^\infty \rho[U(x)-u(x,y)]\,dy$. The *boundary-layer displacement thickness* (δ^*) is defined as the distance over which the solid wall must be displaced, to give the same mass-flow deficit as that which exists in the boundary layer, defined as

$$\rho U(x)\delta^* = \int_0^\infty \rho[U(x)-u(x,y)]\,dy \tag{2.4.13}$$

Boundary-layer momentum thickness
Another deficit is the loss of momentum in the boundary layer, this decrease in momentum can be denoted as $\int_0^\infty \rho u(x,y)[U(x)-u(x,y)]\,dy$. If the flow was inviscid, it would be necessary to move the solid wall outwards to obtain the moment deficit. This distance, is the *boundary-layer momentum thickness* (θ), defined as

$$\rho U(x)^2\theta = \int_0^\infty \rho u(x,y)[U(x)-u(x,y)]\,dy \tag{2.4.14}$$

Since both of these parameters are determined by the density and velocity of the flowing medium, this is experimentally much easier to obtain. With a constant ρ, the δ^* and θ can be written as (2.4.15) and (2.4.16). The non-dimensional parameter relating to the velocity profile inside of the boundary layer is the *shape factor* (H), calculated by $H = (\delta^*/\theta)$.

$$\delta^* = \int_0^\infty \left(1 - \frac{u(x,y)}{U(x)}\right) dy \tag{2.4.15}$$

$$\theta = \int_0^\infty \frac{u(x,y)}{U(x)}\left(1 - \frac{u(x,y)}{U(x)}\right) dy \tag{2.4.16}$$

With the input of δ^* and θ, a model for the the boundary layer disturbance thickness is made. This can be calculated by,

$$\delta = \theta * \left(3.15 + \frac{1.75}{(\delta^*/\theta) - 1} + \delta^*\right) \tag{2.4.17}$$

The boundary layer disturbance thickness (δ) is an important parameter in the prediction models for airfoil self noise, explained in Chapter 2.7.

2.4.4 Laminar and turbulent flow

Most of the flows in turbo machinery are *turbulent flows*, with laminar and transitional regimes occurring near the leading edge. Turbulence is characterised by irregular fluctuations, it originates from instabilities in the laminar flow where mass is interchanged between the boundary layers. In a *laminar flow* these irregular fluctuations are not present. The flow is ordered, with no mass interchanging between the boundary layers.

To take this turbulence into account often the so-called Reynolds averaging is used. The velocity is decomposed into a time-averaged value and a fluctuating part. Substituting these parts into the Navier-Stokes equations leads to an extra term, the Reynolds stress. Only this correlation is not directly related to the time-averaged velocity, resulting in a closure problem and certain assumptions must be made. This is known as Reynolds Averaging Navier Stokes (RANS) equations.

Transition

The *transition* between laminar and turbulent flow can be classified into four types. First, the phenomena during a transition process must be understood, F. M. White [11] distinguished this process into seven different steps before the flow becomes fully turbulent, a representation is given in Figure 8 and listed below.

1. Stable laminar flow near the leading edge.
2. Unstable two-dimensional Tollmien-Schlichting[5] (TS) waves when Re_{crit} is reached.
3. Development of three-dimensional unstable waves and hairpin eddies.
4. Vortex breakdown at regions of high localized shear.
5. Cascading vortex breakdown into fully three-dimensional fluctuations,
6. Generation of locally turbulent spots at intense fluctuations.
7. Merging of the turbulent spots into a fully turbulent flow at Re_{tr}.

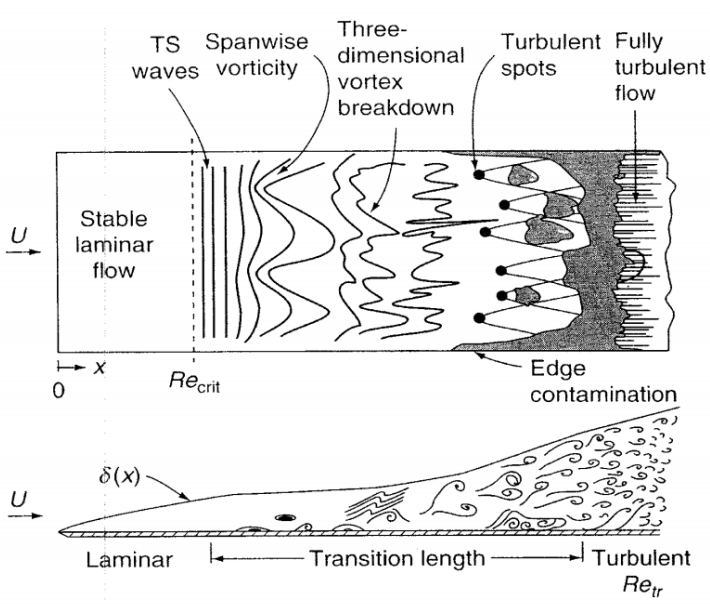

Figure 8: Representation of the boundary layer transition process over a flat plate [11].

[5]The first infinitely small indications of laminar-flow instabilities.

The transition can be distinguished into four different types [11][13], namely;

1. *Natural transition*, the gradual process presented in Figure 8 (assumptions: a quite flow and smooth walls).
2. *Bypass transition*, here the first few steps of the transition are bypassed. The first three or five stages are skipped due to rough walls, a noisy free stream, vibrating walls or incoming acoustic waves.
3. *Separate-flow transition*, when boundary layers are separating and a separation bubble is created, it is most likely that the boundary layer will reattach as a turbulent flow.
4. *Forced transition*, an intentionally added surface imperfections causes the boundary layers to trip and results directly in a fully turbulent flow.

Other factors affecting the transition are surface curvature and the level of turbulence in the freestream.

Tripped boundary-layer

Regarding wind turbines blades there is a constant presence of small contamination's on the surface, this due to insects and other foreign material lingering to the blades especially at the front. These small imperfections are causing the flow to transit from laminar to a turbulent flow. This is similar to the principle of a forced transition. This type of transition is often used to simulate this principle, therefore intentionally adding a surface imperfection to assess the influence. This influences the boundary layer, so there will be referred to as a *tripped boundary layer*. These surface imperfections near the leading edge are often imitated by a wire or cylinder stretched across the flow, a zigzag - or tubulator tape or a grain of sand. White [11] states that the height of the trip (k) must be larger that than 0.3 of the boundary layer displacement thickness ($\delta^*/k \geq 0.3$). An schematic example is given in Figure 9.

Tripping devices such as a zigzag tape are crucial in wind turbine experiments with airfoils. In this way, a turbulent boundary layer can be simulated. The transition from laminar to turbulent at a wind turbine blade is positioned near the leading edge, due to their geometry and/or the incoming velocity, resulting in a turbulent boundary layer structure. In this way the same phenomena occurs, and experiments comparable to real life can be executed.

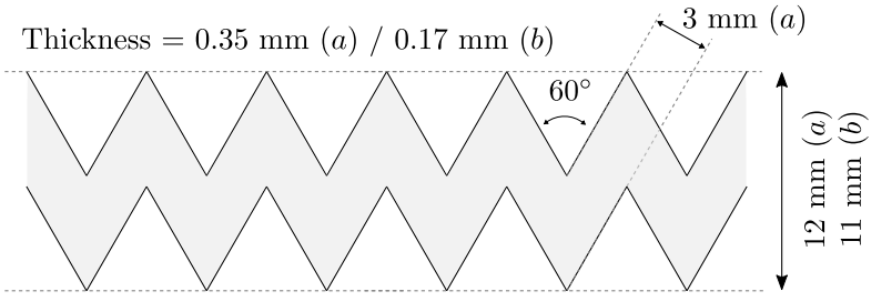

Figure 9: Zigzag tape [13].

2.5 Aerodynamics of an Airfoil

In the next section, the aerodynamic fundamentals and concepts of an airfoil are explained. A text book about the fundamentals of aerodynamics is [14], other relevant literature for this section are [4], [5] and [11]

2.5.1 Aerodynamic Fundamentals

Pressure and shear distribution

Although the interaction between a body and the surrounding moving fluid may seem complicated. The aerodynamic forces and moments on the body are entirely based on two rather basic concepts explained by Anderson [14] namely,

1. The *pressure distribution* (p) over the body surface, acting normal to the surface. Often given as the pressure coefficient distribution over the airfoil, corresponding to certain coordinates on the airfoils surface, see (2.5.9).
2. The *shear stress distribution* (τ) over the body surface, caused by friction between the body and the flowing medium acting tangential to the surface, also called tugging (Fig. 10a).

The interaction between the flow and the body (due to these phenomena) results in a moment (M) and a reaction force (R), this is shown in Figure 10b. This reaction force is often split into the lift force (L), perpendicular to the free stream, and the drag force (D) parallel to U_∞. This is given schematically in Figure 10c, and mathematically expressed in (2.5.1).

$$\begin{aligned} L &= N\cos(\alpha) - A\sin(\alpha) \\ D &= N\sin(\alpha) + A\cos(\alpha) \end{aligned} \tag{2.5.1}$$

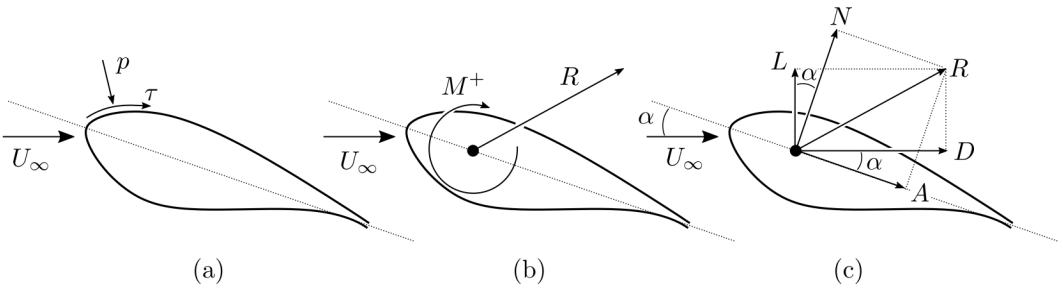

Figure 10: Pressure - and shear distribution, aerodynamic forces and moment acting on an airfoil [13].

The equations to determine the aerodynamic normal force (N), the axial force (A) and the momentum are given in (2.5.2), (2.5.3) and (2.5.5) respectively. The underscript l and u are referring to the lower and upper side of the airfoil. Here θ is the angle between the pressure at a specific chord length and the normal force, or the angle between the shear stress and the axial force ($p \perp \tau$ and $N \perp A$).

$$N = -\int_{LE}^{TE} \left[p_u\cos(\theta) + \tau_u\sin(\theta)\right]\, ds_u + \int_{LE}^{TE} \left[p_l\cos(\theta) - \tau_l\sin(\theta)\right]\, ds_l \tag{2.5.2}$$

$$A = \int_{LE}^{TE} \left[-p_u\sin(\theta) + \tau_u\cos(\theta)\right]\, ds_u + \int_{LE}^{TE} \left[p_l\sin(\theta) + \tau_l\cos(\theta)\right]\, ds_l \tag{2.5.3}$$

$$M = \int_{LE}^{TE} \left[p_u\cos(\theta) + \tau_u\sin(\theta) - p_u\sin(\theta) - \tau_u\cos(\theta)\right]\, ds_u \tag{2.5.4}$$

$$+ \int_{LE}^{TE} \left[(p_l\cos(\theta) - \tau_l\sin(\theta) + (p_l\sin(\theta) + \tau_l\cos(\theta)\right]\, ds_l \tag{2.5.5}$$

Example 2:
As Anderson describes in [14] with an example of a supersonic flow over a 5° half-angle wedge, with a chord of $2m$, $\alpha = 0°$, $P_\infty = 1.01 \times 10^5 N/m^2$, $M_\infty = 2.0$, and $\rho_\infty = 1.23 kg/m^3$. This resulted in a drag force 85% determined by the pressure/wave drag (D_p), and only 15% related to the so-called skin friction drag (D_τ).

$$D = \underbrace{1.052 \times 10^5}_{D_p} + \underbrace{0.1873 \times 10^4}_{D_\tau} = 1.24 \times 10^4 N$$

Because of the low influence of the skin fraction drag on the drag force, in some cases D_τ is neglected resulting in simplified versions of the equation for N, A and M. This will be evaluated later with an XFOIL simulation for the NACA0012.

Aerodynamic coefficients
The lift force, drag force and the momentum of an airfoil are often expressed as a dimensionless coefficient, hereby the free stream *dynamic pressure* (q_∞) is taken into account. This dimensional quantity is described as $q_\infty = \frac{1}{2}\rho U_\infty^2$, and gives the fluid's kinetic energy per unit volume. The *lift coefficient* (C_L), *drag coefficient* (C_D) and *momentum coefficient* (C_m) can be calculated with (2.5.6), (2.5.7) and (2.5.8) where c is the chord length.

$$C_L = \frac{L}{q_\infty c} \tag{2.5.6}$$

$$C_D = \frac{D}{q_\infty c} \tag{2.5.7}$$

$$C_M = \frac{M}{q_\infty c^2} \tag{2.5.8}$$

Furthermore other relevant coefficients are the *pressure coefficient* (C_P) and the friction coefficient (C_F), given in (2.5.9) and (2.5.10). To calculate C_P, the pressure difference between the surface and the freestream ($p(x/c) - p_\infty$) is divided by the dynamic pressure (q_∞). Further in depth theory about the fundamentals of aerodynamics are given in [14].

$$C_P = \frac{p - p_\infty}{q_\infty} \tag{2.5.9}$$

$$C_F = \frac{\tau}{q_\infty} \tag{2.5.10}$$

2.5.2 Aerodynamic Concepts

In the next section, the most important aerodynamic concepts are explained.

Flow separation
When air is flowing around an airfoil, the same principles occur similar to the case of a solid wall (Figure 7). The flowing medium causes for different pressure values around the airfoil, and frictional forces are decelerating the fluids motion near the surface. When moving from the LE in streamwise direction over the surface of the suction side (top), at first the pressure gradient is positive/favorable ($\partial p/\partial s > 0$), and no boundary layer separation is occurring. This also results in $\left(\frac{\partial^2 u}{\partial y^2} > 0\right)$, resulting from Equation (2.4.11). When moving in streamwise direction over the surface (denoted by s in Figure 11), viscous forces are influencing the velocity at the surface more and more, and the velocity profile near the surface is affected. Around the point of maximum airfoil thickness, the gradient in the pressure switches from positive to negative ($\partial p/\partial s < 0$) and *boundary layer flow separation* is occurring. Here the flow near the surface is reversed in direction, this is called the *separation point*. After that point a large wake is created. This is schematically shown in Figure 11, pressure and velocity distribution near the surface is given Figure 12.

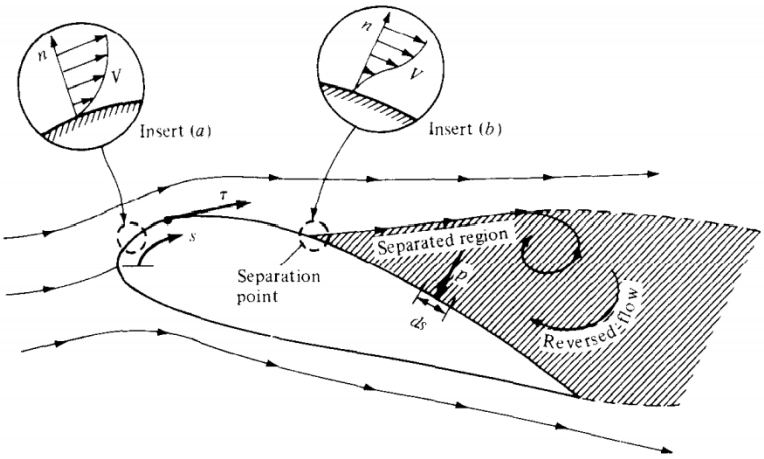

Figure 11: Boundary layer separation occurring on an airfoil [14].

After the separation point (where $\frac{\partial u}{\partial y}|_{y=0} = 0$), the velocity profile curvature becomes more S-shaped and results in more and more reversed flow. A large wake with recirculation zone is the result, here the flow is so-called *stalled*. Determining the separation point can be done by simplifying the boundary layer equations (2.4.11), this results in (2.5.11). As mentioned the velocity distribution profile is not affected by Re, so this is also true for the separation point. The separation point can also be easily detected by the pressure coefficient distribution. When the boundary layer is separated and not reattached, this results in a constant negative C_P at the suction side after the separation point. The flow is now completely stalled, and the Pressure Coefficient profile is not a closed loop anymore.

$$\left.\frac{\partial^2 u_x^*}{\partial y^{*2}}\right|_{y=0} = \frac{\partial p^*}{\partial x^*} \tag{2.5.11}$$

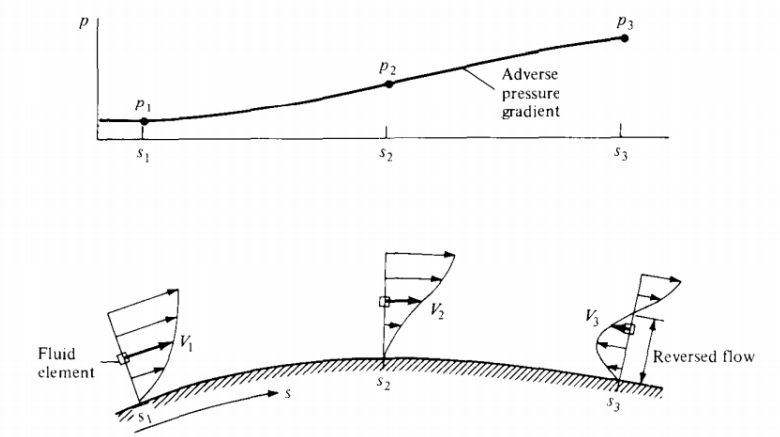

Figure 12: Pressure and velocity distribution near the surface of an airfoil, flow separation occurs after s2 [14].

Laminar separation bubble

Regarding laminar flows with a low Re, a so called *laminar separation bubble* can occur (Figure 13). Flow separation occurs when there is an adverse pressure gradient and the flow separates at point S. Turbulent structures are generated inside of this bubble at point T, due to an unstable shear layer. Mixing of the particles inside of this bubble with the flowing freestream is allowing the flow to reattach at point R. As the angle of attack increases R moves further downstream, and the separation bubble becomes larger. This recirculation zone pushes the free streamlines outwards, resulting in a thickening of the boundary layer and an increased induced drag at this position of the chord. Little mass or momentum exchange is occurring between the bubble and the freestream, preventing the bubble from bursting. This laminar separation phenomena is influencing the pressure and its coefficient, resulting in a small bump in the C_P vs. x/c curve (Figure 13b), explained in depth in section 2.8.

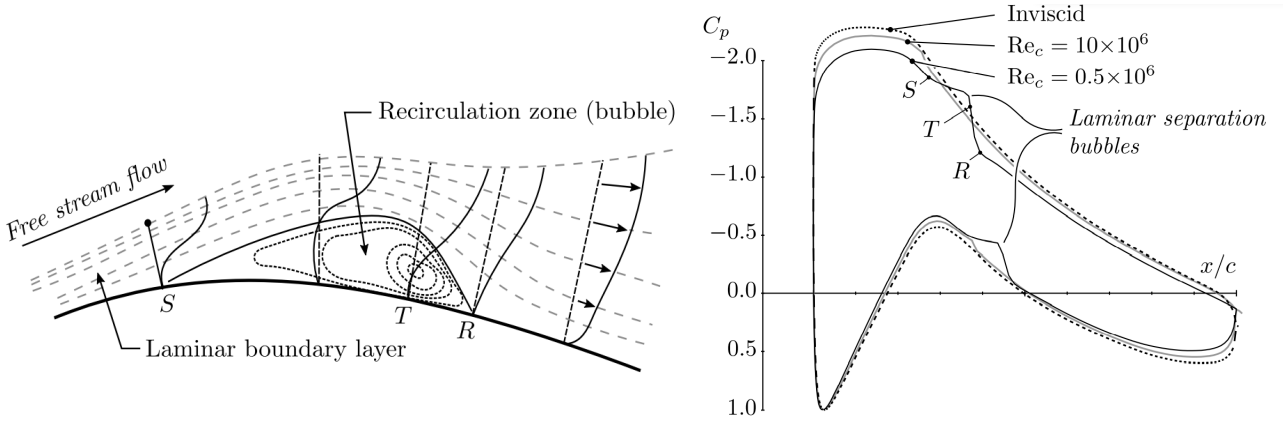

(a) Schematic representation. **(b) Pressure Coefficient.**

Figure 13: Laminar separation bubble occurring at low Reynolds numbers [13].

2.6 Aeroacoustics

Hansen et al. [15] identified noise as, a disagreeable or undesired sound. From an acoustics point of view sound and noise constitute the same phenomena, but what is sound to one person can be noise to another, so it is greatly subjective. In this case, there will be dealt with undesired sound from an airfoil, so there will be referred to noise. Relevant literature regarding aeroacoustics are [15], [16] and [17].

2.6.1 Acoustic Fundamentals

Noise originates from small pressure fluctuations or oscillations in a viscous medium, this due to a vibrating surface or turbulent structures in the flow (Figure 14). Noise propagates as a longitudinal wave, consisting of regions with compression and rarefactions (small changes in density).

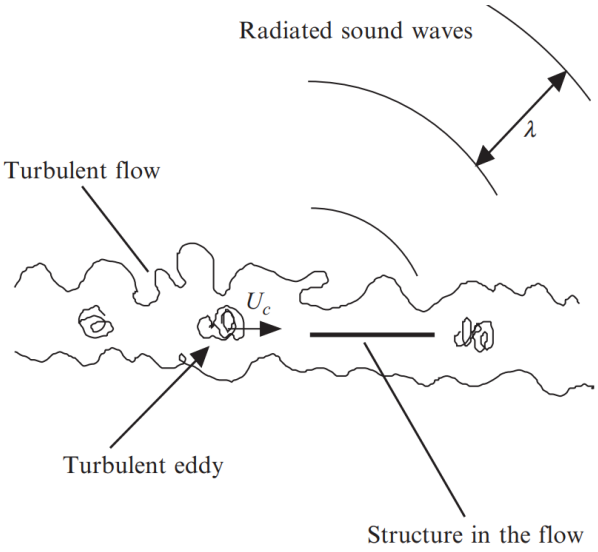

Figure 14: Radiated sound wave, due to a turbulent structure in the flowing medium [16].

Wave characterisation
Every traveling harmonic wave can be represented as a set of $sin(kx - \omega t)$ and $cos(kx - \omega t)$ of the same wave number, frequency, and velocity. The *wave number* (ν) is the spatial frequency of a wave and can be calculated with (2.6.1), the wave number is the inverse of the wavelength (λ).

$$\nu = \frac{1}{\lambda} \tag{2.6.1}$$

The *angular wave number* (k) is more often used and can be calculated with (2.6.2). Where the frequency is the number of waves per unit time, the wave number is the number of waves per unit distance. Furthermore, the wave number is equivalent to the angular frequency (ω) divided by the speed of sound (c_0) and is also called the angular frequency (in the spatial domain).

$$k = \frac{2\pi}{\lambda} = \frac{\omega}{c_0} \tag{2.6.2}$$

Using de-Moivre's formula the representation of a harmonic traveling wave can be simplified to (2.6.3). Here both the real and imaginary parts represent the wave, only with a phase shift (ϕ) between the two ($i = \sqrt{-1}$).

$$\begin{aligned} u(x,t) &= A[cos(kx - \omega t) + i \cdot sin(kx - \omega t)] &= Ae^{i(kx-\omega t)} \\ u(\omega,t) &= A[cos(\omega t + \phi) + i \cdot sin(\omega t + \phi)] &= Ae^{i(\omega t+\phi)} \end{aligned} \tag{2.6.3}$$

Sound Pressure Level

In acoustics this pressure difference is often defined as the *Sound Pressure Level* (SPL). The SPL is the local pressure deviation from the average atmospheric pressure, caused by a sound wave (and can be measured at any given observer location). The relation is given in (2.6.4), where $p(t)' = p(t) - p_{atm}$. To obtain the root mean square pressure levels (p_{rms}), all pressure values in the specified time interval (T) are squared, then integrated, divided by T and multiplied by $1/2$, before taking the square root to find p_{rms}.

$$\begin{aligned} SPL &= 20 \cdot log_{10}\left(\frac{p_{rms}}{p_0}\right) \\ \langle p^2 \rangle = p_{rms} &= \sqrt{\frac{1}{2T}\int_0^T p'(t)^2 dt} \end{aligned} \tag{2.6.4}$$

The SPL is expressed in $[dB]$, to get to this quantity the logarithm operator and the introduction of a reference pressure is required. Decibel refers to a ratio, so often the reference of the normal (average) threshold of the human hearing at $1.8kHz$ is used ($p_0 = 20\mu Pa$). A log scale is used because the human ear has a very large dynamic range for hearing. A representation of a sound wave with its compression and rarefaction is given in Figure 15a, Figure 15b shows the value of p_{rms} of a sound wave.

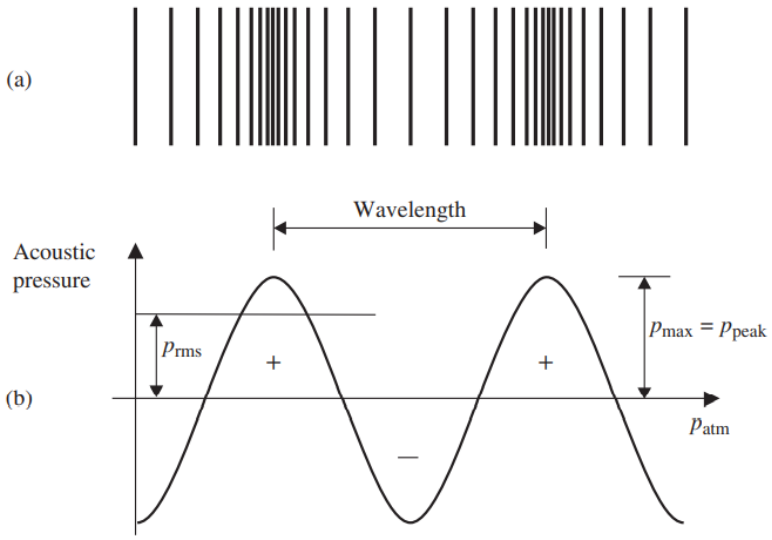

Figure 15: Representation of a sound wave: (a) compressions and rarefactions caused by the sound wave; (b) pressure variations above and below p_{atm} [15].

Sound Power Level

Another aeroacoustic parameter is the *Sound Power Level* (SPW). The intensity (I) is defined as $I = p'v'$, so a multiplication of the derivatives of the pressure and particle velocity. The power related to the acoustic wave in a certain area can be calculated with an integral of the intensity over a certain region. This results in the relation for the SPW given in (2.6.5), with the use reference of $P_{ref} = 10^{-12}W$.

$$\begin{aligned} SPW &= 10 \cdot log_{10}\left(\frac{P}{P_0}\right) \\ P &= \oint_A (I \cdot n) dA \end{aligned} \tag{2.6.5}$$

Fourier Transform
Regarding pressure fluctuations there will be referred to as $p'(t)$, the derivative of the pressure over time. A tilde sign such as $\tilde{p}(\omega)$, denotes the *Fourier Transform* and is one of the most important mathematical tools in aeroacoustics. This Fourier transform gives a better identification of complex noise sources. With the Fourier transform, parameters can be related from the time or spacial domain, to the time or spacial frequency domain. The relation for the *time dependant Fourier transformation* is given as,

$$\tilde{p}(\omega) = \mathcal{F}[p'(t)] = \frac{1}{2\pi}\int_{T_0}^{T_\infty} p'(t)e^{i\omega t}\,dt \tag{2.6.6}$$

Where T tends to infinity, the *time dependant inverse Fourier transform* follows as,

$$p'(t) = \mathcal{F}^{-1}[\tilde{p}(\omega)] = \int_{-\infty}^{\infty} \tilde{p}(\omega)e^{-i\omega t}\,d\omega \tag{2.6.7}$$

The *spacial Fourier transform*, in 1D, is given in (2.6.8) (denoted by two tildes). Where R tends to infinity this results in the *inverse spacial Fourier transform* given in (2.6.9).

$$\tilde{\tilde{f}}(k_1) = \mathcal{F}[f(x_1)] = \frac{1}{2\pi}\int_{R_1}^{R_2} f(x_1)e^{ik_1x_1}\,dx_1 \tag{2.6.8}$$

$$f(x_1) = \mathcal{F}^{-1}[\tilde{\tilde{f}}(k_1)] = \int_{-\infty}^{\infty} \tilde{\tilde{f}}(k_1)e^{ik_1x_1}\,dk_1 \tag{2.6.9}$$

Regarding the results, they will often be shown as the Sound Power Level, so integrated over a certain region. Time data is acquired and will be converted to the frequency domain by the use of Equation (2.6.6).

2.6.2 The wave equation

The wave equation gives the propagation of an acoustic wave through a medium. It is assumed that there is no significant flow and the time average properties are uniform throughout. The derivation of the wave equation considers three important formula: the mass balance (2.6.10), momentum equation (2.6.11) and the equation of state (2.6.12).

$$\frac{\partial \rho'}{\partial t} + \rho_0\frac{\partial u}{\partial x} = 0 \tag{2.6.10}$$

$$\rho_0\frac{\partial u}{\partial t} + \frac{\partial p'}{\partial x} = 0 \tag{2.6.11}$$

$$p' = c_0^2\rho' \tag{2.6.12}$$

Rewriting the equation of state as ρ' and substituting it in the mass balance (2.6.10) gives,

$$\frac{1}{c_0^2}\frac{\partial p'}{\partial t} + \rho_0\frac{\partial u}{\partial x} = 0 \tag{2.6.13}$$

Taking the time derivative of this equation, and taking the spacial derivative of the momentum equation (2.6.11), and subtracting them gives the *linearized acoustic wave equation* (2.6.14). Now the wave equation is given as a function of the pressure. This can also be done for the velocity (u).

$$\begin{aligned} \tfrac{1}{c_0^2}\tfrac{\partial^2 p'}{\partial^2 t} + \cancel{\rho_0\tfrac{\partial^2 u}{\partial x \partial t}} &= 0 \\ \cancel{\rho_0\tfrac{\partial^2 u}{\partial t \partial x}} + \tfrac{\partial^2 p'}{\partial x^2} &= 0 \\ \hline \tfrac{1}{c_0^2}\tfrac{\partial^2 p'}{\partial^2 t} - \tfrac{\partial^2 p'}{\partial x^2} &= 0 \end{aligned} \tag{2.6.14}$$

In 3D this gives (2.6.15), where the signal change must be small and the medium inviscid, thermally nonconducting, and quiescent (non moving medium). Classical mechanics refers this pressure fluctuation to three different phenomena mass injection, heat injection and force fluctuation. For a perfect gas this results in (2.6.16), where the term on the left is often referred to as the wave operator. Here the overdot above a certain variable indicates the time derivative ($\dot{m} = dm/dt$).

$$\frac{1}{c_0^2}\frac{\partial^2 p'}{\partial^2 t} - \nabla^2 p' = 0 \tag{2.6.15}$$

$$\underbrace{\frac{\partial^2 p'}{\partial t^2} - \nabla \cdot \left[c_0^2 \nabla p'\right]}_{\text{Wave operator}} = \underbrace{c_0^2 \frac{1}{\gamma}\frac{\partial \dot{m}'}{\partial t}}_{\text{mass injection}} + \underbrace{(\gamma - 1)\frac{\partial \dot{\nu}}{\partial t}}_{\text{heat injection}} - \underbrace{\nabla \cdot \left[c_0^2 f'\right]}_{\text{force fluctuation}} \tag{2.6.16}$$

2.6.3 Wave quantification

The simplest example is a *plane wave*, a sound propagating along a thin tube can be described as a plane wave. This can be solved with the use of d'Alemberts solution (2.6.17) and the linearlized wave equation. Here the first solution $f(t - x_1/c_0)$ represents a wave in the positive direction, and the $g(t + x_1/c_0)$ in the negative direction. Hereby a pressure perturbation f(t) at $x_1 = 0$ will be repeated at the location $x_1 = d$ at a time d/c_o. The *retarded time* is the time at the observer minus the propagation time, defined in (2.6.18). The effect of retarded time is therefore a key component in the quantification of the far field noise.

$$p'(x_1, t) = f(t - x_1/c_0) + g(t + x_1/c_0) \tag{2.6.17}$$

$$\tau = t - \frac{x}{c_0} \tag{2.6.18}$$

A more practical approach is the wave equation in *spherical 3D coordinates*, expressing this relation for the propagation of a wave limited to only the radial component (r, from the center of the coordinate system) gives (2.6.19). Multiplying d'Alemberts by r gives $rp'(x_1, t) = f(t - r/c_0) + g(t + r/c_0)$, where f and g represent the propagation of a wave in respectively, outwards - and inwards spherical direction . In general, only the outwards going wave is interesting, resulting in the solution to the wave equation given in (2.6.20).

$$\frac{1}{c_0^2}\frac{\partial^2 p'}{\partial^2 t} - \frac{1}{r}\frac{\partial^2}{\partial r^2}(rp') = 0 \tag{2.6.19}$$

$$p'(r, t) = \frac{f(t - r/c_0)}{r} \tag{2.6.20}$$

In many cases it is more relevant to evaluate the sound wave as a function of frequency rather than time. Taking the time dependence of a harmonic wave into account $f(t) = A(\omega t - \phi)$, rewriting it as $Ae^{-i\omega t}$ results in a complex output. Here the complex amplitude of the pressure, as a function of position for spherical waves is given as (2.6.21). The hat indicates a complex amplitude, k is the angular wavenumber. Inserting this formula in the linearized wave equation gives the well known *Helmholtz equation* (2.6.22).

$$\hat{p}(r) = \frac{\hat{A}e^{ikr}}{r} \tag{2.6.21}$$

$$\nabla^2 \hat{p} + k^2 \hat{p} = 0 \tag{2.6.22}$$

2.6.4 Sound sources

The solution for the unknown complex amplitude of a sound generated by a small sphere, can be found by matching the particle velocity of the sound wave in the radial direction to the velocity of the surface ($[\hat{v}_r]_{r=a} = u_0$). This results in (2.6.23). Here a denotes the radial position and u_0 the velocity of the surface. Substituting this into (2.6.21) gives Equation (2.6.24)

$$\hat{A} = \frac{i\omega\rho_0 a^2 u_0 e^{ika}}{(1-ika)} \tag{2.6.23}$$

$$\hat{p}(r) = \frac{i\omega\rho_0 a^2 u_0 e^{ik(r-a)}}{(1-ika)r} \tag{2.6.24}$$

The acoustic pressure can also be a function of the change of volume caused by the surface displacement. So a radially pulsating sphere can also be referred to as a volume displacement source. This is a simple acoustic source also known as a *monopole*, where the sound field is only a function of the distance from the center of the sphere and omnidirectional. The surface area of a sphere is $S = 4\pi a^2$, the rate of volume change of a sphere can be formulated as,

$$Qe^{-\omega t} = u_0 S e^{-\omega t} \tag{2.6.25}$$

Resulting in,

$$\hat{p}(r) = \frac{i\omega\rho_0 Q e^{ikr}}{4\pi r} \tag{2.6.26}$$

A simple multi-pole source is the *dipole*, and reflects the behaviour of a translating sphere. Here the surface velocity is given as, $[\hat{v}_r]_{r=a} = u_0\cos(\theta)$, where θ is the angle subtended by the point on the surface and the x_1-axis (viscosity effects are neglected). A solution for the complex amplitude of the pressure can be found by taking the derivative of (2.6.21), resulting in (2.6.27). So a dipole source can be noted by the presence of a $\cos(\theta)$ in $\hat{p}(r)$.

$$\hat{p}(r) = \frac{\partial}{\partial x_1}\left(\frac{\hat{A}e^{ikr}}{r}\right) \tag{2.6.27}$$

Rewriting this gives,

$$\hat{p}(r) = ik\cos(\theta)\left(\frac{i\omega\rho_0 v_0 a^3 e^{ikr}}{2r}\right)\left(1 - \frac{1}{ikr}\right) \tag{2.6.28}$$

Next to Monopole and Dipole sources, there is also a *quadruple source*. Two opposite dipoles make up a quadruple source, the equations involving a quadruple source will not be discussed. Schematic representations of the sound sources are given in Figure 16.

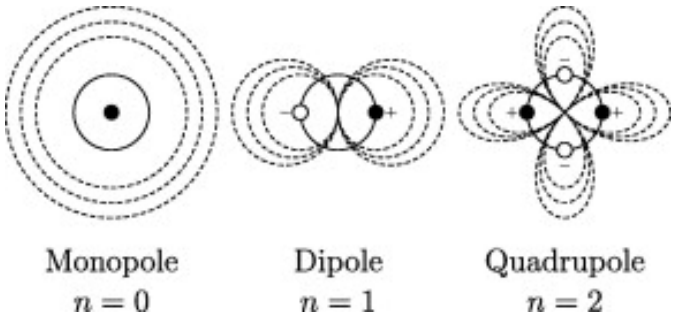

Figure 16: Schematic presentation of noise sources [18].

2.6.5 Green's function

A function named after the British mathematician George Green is the Green's function, and can help to solve the wave equation. This function is distributed in space and is dependent on the observer location x on time t, due to some sound source distributed in space y at time τ ($G(x,t|y\tau)$). With the Dirac delta function ($\delta(\mathbf{x}-\mathbf{y})\delta(t-\tau)$) and Gauss's Divergence theorem, the general solution for the Green's function to solve the wave equation results in,

$$p'(\mathbf{x},t) = \int_{-T}^{T}\int_{S}\left(p'(\mathbf{y},\tau)\frac{\partial G(\mathbf{x},t|\mathbf{y},\tau)}{\partial y_i} - G(\mathbf{x},t|\mathbf{y}\frac{\partial p'(\mathbf{y},\tau)}{\partial y_i}\right) n_i dS(y)\, d\tau \tag{2.6.29}$$

This solution represents two terms, the first term indicates the noise due to the force exerted by the vibrating surface on the flow, and the second the noise due to the surface vibration. The free field Green's function is defined as,

$$G_0(\mathbf{x},t|\mathbf{y},\tau) = \frac{\delta(t-|\mathbf{x}-\mathbf{y}|\ c_0-\tau)}{4\pi|\mathbf{x}-\mathbf{y}|} \tag{2.6.30}$$

G is very difficult to be obtained analytically so different computational techniques are developed to solve this problem. For example finite element method or boundary element method, to obtain the results from the experiments a certain algorithm for the beamforming technique is used (see Chapter 3.3).

2.7 Airfoil Noise

In this section, the important airfoil self-noise mechanisms are given. Furthermore, prediction models for these self-noise types with their important parameters are explained.

2.7.1 Self-noise production mechanisms

A lot of studies have been executed related to airfoil self-noise production mechanisms. In 1983 Brooks and Burley [19] reviewed rotor broadband noise, and gave discrepancy between the main airfoil self-noise mechanisms contributing to the total airfoil noise. These mechanism consist out of five main types of self-noise given in Table 1.

Table 1: Airfoil self-noise production mechanisms.

#	**Type of noise**	**Description**	**Visual representation** [19]
1.	Laminar boundary layer noise	Caused by instabilities in the wave, present at low Reynolds numbers. It has a ladder type structure in the frequency-velocity plot.	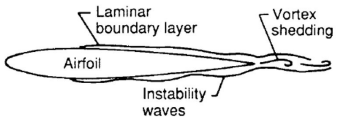 Laminar-boundary-layer—vortex-shedding noise
2.	Turbulent boundary layer noise	Influencing the broadband component of the noise, caused by scattering at the trailing edge, occurring at high Reynolds numbers.	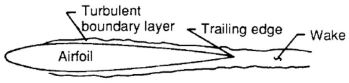 Turbulent-boundary-layer—trailing-edge noise
3.	Boundary layer separation noise	Influencing the low frequency domain because of the larger scales, often occurring at high angles of attack (at for example a helicopter). Creating a deep stall when large scale separation is occurring.	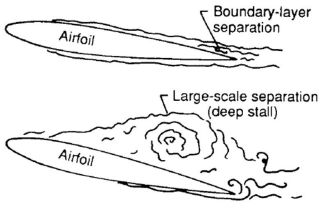 Separation-stall noise
4.	Boundary layer bluntness noise	Generated due to the the passage of the trailing edge vertices from the unstable shear layer on both airfoil suction and pressure sides. Occurring when $\delta^* > t_{TE}$.	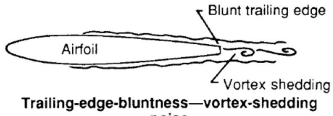 Trailing-edge-bluntness—vortex-shedding noise
5.	Tip vortex noise	Generated at the tip of the airfoil (or at the tip of a propeller), can be influenced by changing the geometry at the tip.	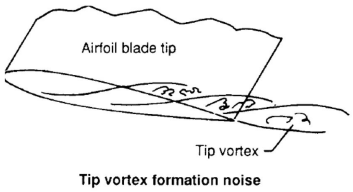 Tip vortex formation noise

Regarding wind turbine noise, turbulent boundary layer noise is the only self-noise type that can not be circumvented. All other self-noise mechanisms can be avoided by proper blade design and/or software.

2.7.2 Airfoil self-noise prediction, by Brooks

Brooks et al. [12] developed an overall prediction method for airfoil self-noise. This by an aerodynamic and acoustic analysis, based on semi-empirical experiments conducted on seven NACA0012 airfoils of different sizes (chord lengths from 25 to 610 mm) in an anechoic wind tunnel. Prediction methods are given for the airfoil self-noise production mechanisms from Table 1. Angles of Attack from 0° to 25.2°, and Re up to $4.6 \cdot 10^6$ are used. General equations related to the prediction of the SPL (based on the 1/3-octave band), for all airfoil self-noise mechanisms are given in this section. An in depth view of the prediction of the combined turbulent boundary layer trailing edge and the separated flow noise is given. This self-noise type occurring at at the trailing edge often dominates the airfoil self-noise, and gives an detailed description of the important parameters.

The four airfoil self-noise categories, for the prediction used by Brooks are;
1. Turbulent Boundary Layer Trailing Edge, and Seperated Flow Noise (TBL-TE)
2. Laminar Boundary Layer and Vortex Shedding noise (LBL-VS)
3. Trailing Edge Bluntness Vortex Shedding Noise (BLUNT)
4. Tip Vortex Formation Noise (TIP)

The self-noise spectra for different flow velocities (U) at an α of 0° are given in Figure 17. The data refers to hot-wire probe measurements made in the boundary-layer in the near-wake region of the TE of the airfoil. At higher flow velocities the noise is dominated by TBL-TE noise. Levels regarding the suction and pressure side overlap because of symmetry and the used AoA. At lower flow velocities, the LBL-VS noise becomes more and more present at frequencies ranging from 0.6-2 kHz. In general the whole amplitude of the SPL curve decreases when the velocity is lowered (see y-axis).

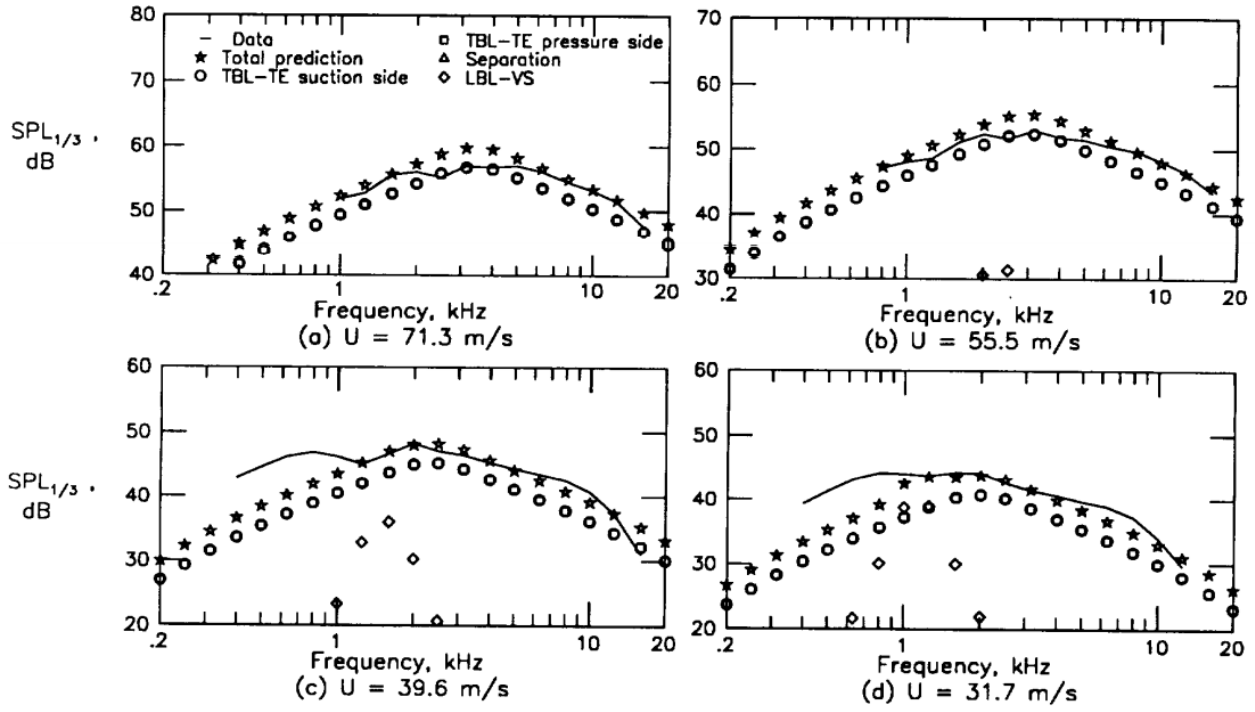

Figure 17: Self-noise spectra at different flow speeds, AoA of 0°, c=304.8 mm and a free transition [12].

The influence of the angle of attack on the self-noise spectra is given in Figure 18. A nonzero AoA results in a difference of the SPL for the pressure and suction side, regarding TBL-TE noise. So noise generation is not similar anymore for both sides of the airfoil. Increasing the AoA, results in an increase of the SPL due to LBL-VS and Separation Noise. So the peek around 3kHz in Figure 18c and 18d is a result of all the self-noise types popping up around the same frequencies. In general the broadband component of this plot increases, when the AoA increases. This tonal noises at specific frequencies, with significantly higher amplitudes in SPL are caused by the additional presence of LBL-VS and Separation noise, occurring at higher AoA.

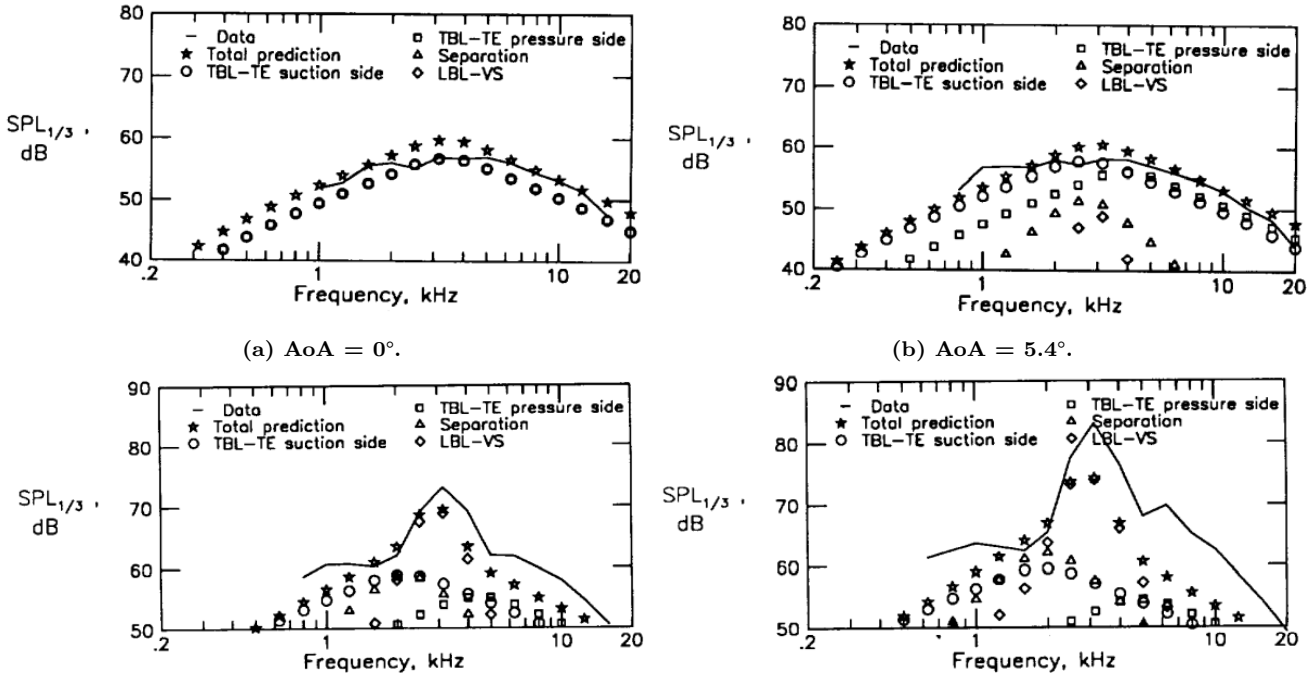

(a) AoA = 0°.

(b) AoA = 5.4°.

(c) AoA = 10.8°.

(d) AoA = 14.4°.

Figure 18: Self-noise spectra at different AoA, U=71.3 m/s, c=304.8 for a free transition [12].

Regarding the airfoils with other chord lengths, similar acoustic phenomena occur. The position of this peak in the SPL is slightly shifted to the right when the chord is reduced. At higher Reynolds numbers this peak is due to separation noise. At lower Reynolds numbers LBL-VS noise is most dominantly causing this peak in the noise spectra. Brooks also executed experiments where the boundary layer was tripped, located at 0.2 x/c from the leading edge. In general this resulted in a SPL output where all of the airfoil self-noise types where containing a wider range of frequencies, and less tonal peaks where present especially for the airfoils with a larger chord. In conclusion, with this tripping device the flow becomes turbulent at an early stage near the LE.

Turbulent Boundary Layer Trailing Edge -, and Seperated Flow Noise (TBL-TE)
The prediction of the SPL for the TBL-TE - and separated flow noise is defined in (2.7.1). This noise prediction consists out of three terms that are summed, corresponding to the pressure side, the suction side, and the angle of attack (denoted by p, s and α respectively). Each side of an airfoil with a well developed boundary layers produces noise independently, so the p and s side are uncorrelated. For angles of attack larger than zero ($\alpha > 0$), the third term SPL_α dominates the total TBL-TE noise. This results in,

$$SPL_{TBL-TE} = 10\log\left(10^{SPL_p/10} + 10^{SPL_s/10} + 10^{SPL_\alpha/10}\right) \tag{2.7.1}$$

where,

$$SPL_p = 10\log\left(\frac{\delta_p^* M^5 L\overline{D}_h}{r_e^2}\right) + A\left(\frac{St_p}{St_1}\right) + (K_1 - 3) + \Delta K_1 \tag{2.7.2}$$

$$SPL_s = 10\log\left(\frac{\delta_s^* M^5 L\overline{D}_h}{r_e^2}\right) + A\left(\frac{St_s}{St_1}\right) + (K_1 - 3) \tag{2.7.3}$$

and

$$SPL_\alpha = 10\log\left(\frac{\delta_s^* M^5 L\overline{D}_h}{r_e^2}\right) + B\left(\frac{St_s}{St_2}\right) + K_2 \tag{2.7.4}$$

As can be seen from (2.7.2), (2.7.3) and (2.7.4), these equations all have similar parameters. The first term consist out of the boundary-layer displacement thickness (δ^*), the Mach number (M), the characteristic length (L), the directivity factor ($\overline{D}$) and the distance to the observer in the polar coordinate system (r_e). Additional terms represent a universal spectrum shape $F_i(St)$, and empirical constants K_i. This results in the general solution,

$$SPL_i = 10\log\left(\frac{\delta_i^* M^5 L\overline{D}_h}{r_e^2}\right) + F_i(St) + K_i \tag{2.7.5}$$

Strouhal definitions
Brooks found that the ratio of the Strouhal number at multiple positions on the chord can be used in the prediction of the Sound Pressure Levels for the TBL-TE noise (and other self-noise types).

Directivity
The *directivity* function represents the propagating of the noise in space, often trailing edge noise is simulated as a dipole source. Brooks found that if wavelengths are much shorter than the chord length the noise behaves as a so-called baffled dipole (Figure 19a), corresponding to high frequencies. These functions take into account the fluctuations produced by the convective effect depending on the direction of propagation considered. For low frequency the behaviour can be represented as a pure dipole (Figure 19b).

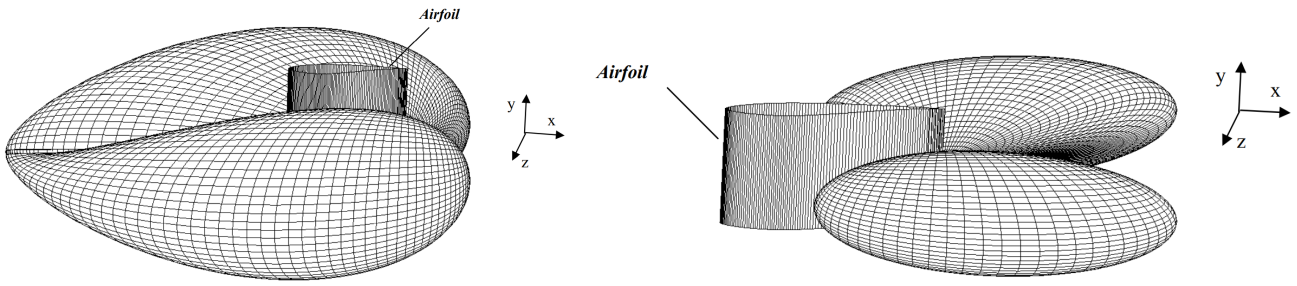

(a) Baffled dipole. **(b) Pure Dipole.**

Figure 19: Representation of the directivity function in 3D [20].

Spectral shape
Here the *spectral shape* function (A) depends on the Reynolds number and is determined by an interpolation of the curves A_{min} and A_{max}. This spectral shape function indicates the amount of presence for a certain frequency in the noise spectrum.

Empirical constants
The amplitude functions (K) are used to overlap the obtained SPL from the experiments with the noise prediction equations. Additional information about the equations related to the Strouhal definitions, directivity, spectral shape and empirical constants are given in Appendix B.

The scaled SPL_{TBL-TE} are given in Figure 20 and plotted versus the the Strouhal number, which gives an interesting result. The SPL values for multiple cases with different U and α, almost overlap when plotted with St on the x-axis. It can be concluded that the SPL_{TBL-TE} contributed to the broadband noise of the total noise spectrum, and does not include tonal peaks. This emphasizes the importance of Strouhal numbers in noise predictions models.

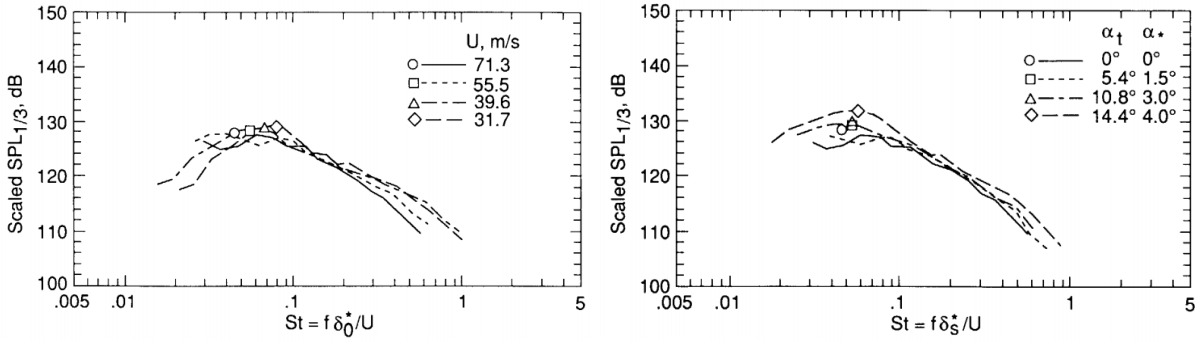

(a) Fixed AoA = 0 °. **(b) Fixed U = 71.3 m/s.**

Figure 20: Scaled 1/3-octave SPL_{TBL-TE}, c=30.48, with a tripped boundary layer [12].

Laminar Boundary Layer Vortex Shedding Noise (LBL-VS)
The relation for the prediction of LBL-VS noise is given in (2.7.6), this equation has similar parameters compared to the TBL-TE noise. Here the second, third and fourth term represent the dependency of, the Strouhal ratio, the Reynolds ratio, and the AoA (with shape functions G_1, G_2 and G_3). Scaled 1/3-octave SPL_{LBL-VS} values are given in Figure 21. For a fixed AoA, increasing the flow velocity results in a slightly higher SPL. Increasing the AoA results in a peak around $St^{'} = 0.2$, and an overall increase of the broadband component of the SPL_{LBL-VS}. It must be noted that laminar boundary layer noise can not occur when a tripping device is used.

$$SPL_{LBL-VS} = 10\log\left(\frac{\delta_p^* M^5 L\overline{D}_h}{r_e^2}\right) + G_1\left(\frac{St^{'}}{St^{'}_{peak}}\right) + G_2\left[\frac{R_c}{(R_c)_0}\right] + G_3(\alpha_*) \tag{2.7.6}$$

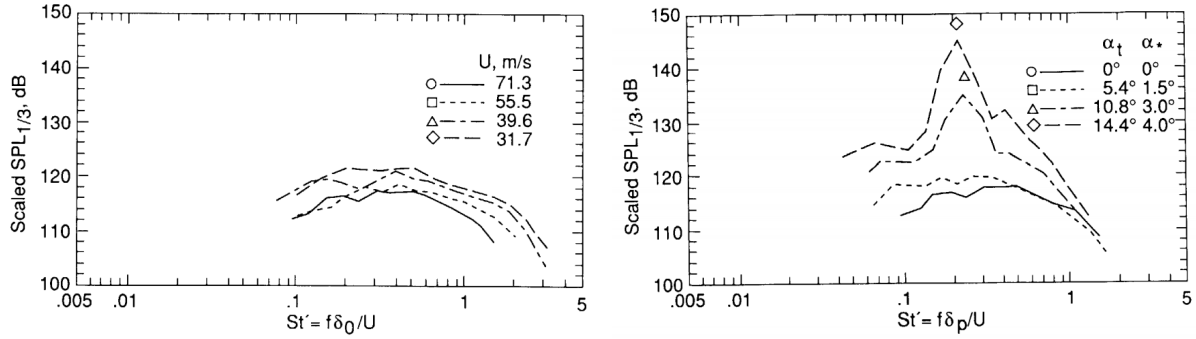

(a) Fixed AoA of 0 °. **(b) Fixed U of 71.3 m/s.**

Figure 21: Scaled 1/3-octave $SPL_{\text{LBL-VS}}$ for an airfoil with c=30.48, free transition [12].

Tip Vortex Formation Noise (TIP)

The noise associated with the turbulence in the locally separated flow region at the tip of a lifting blade (the tip vortex), is schematically shown in Figure 22a. The prediction method proposed is given in (2.7.7), it is important to note that δ^* is not present in this equation, the Mach scaling is slightly different, and again a term with the Strouhal number is present. The results by Brooks contained a comparison between a tip (3D model) and a 2D airfoil to assess the SPL_{TIP}. The results are given in Figure 22b where the circular markers represent the tip vortex formation noise. This shows, that this self-noise mechanism is mainly present in the high frequency domain.

$$SPL_{TIP} = 10\log\left(\frac{M^2 M_{max}^3 l^2 \overline{D}_h}{r_e^2}\right) - 30.5(\log St'' + 0.3) + 126 \tag{2.7.7}$$

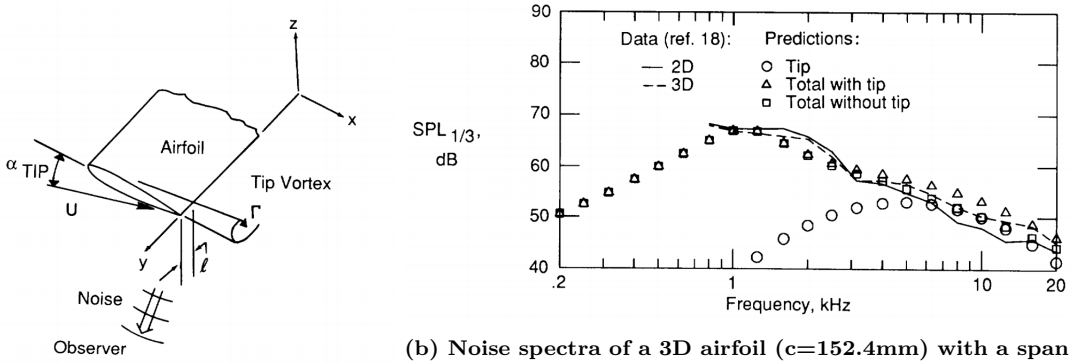

(a) Formation of tip vortex (Γ).

(b) Noise spectra of a 3D airfoil (c=152.4mm) with a span of 304.8mm, and that of a 2D airfoil section (U = 71.3 m/s α = 10.8°).

Figure 22: Tip Vortex Formation Noise [12].

Trailing-Edge-Bluntness-Vortex Shedding Noise (BLUNT)

The prediction for the 1/3 octave SPL_{BLUNT} is given in (2.7.8) Here h is the thickness of the trailing edge, a slightly higher power for the Mach number is used in the first term. Ψ is the angle between the tangents to the pressure and suction curves that defines the geometry of the airfoil at the TE (for the NACA0012, $\Psi = 14°$). The influence of this self-noise on the total SPL is tenuous.

$$SPL_{BLUNT} = 10\log\left(\frac{hM^{5.5}L\overline{D}_h}{r_e^2}\right) + G_4\left(\frac{h}{\delta^*_{avg}}, \Psi\right) + G_5\left(\frac{h}{\delta^*_{avg}}, \Psi, \frac{St'''}{St'''_{peak}}\right) \tag{2.7.8}$$

2.7.3 Amiet's Theory

Another well-established analytical prediction model is Amiet's theory. This model is specified to trailing edge noise, developed by Amiet. This theory is given in (2.7.9), simplified for an observer in the mid-span ($y = 0$). The left hand side (S_{pp}) represents the power spectral density of the far field noise for a certain angular frequency (ω), at chosen position $(x, 0, z)$. Here $\sigma^2 = x^2 + \beta^2 z$ a flow correction for radial distance, $l_y(\omega)$ the frequency dependent spanwise correlation length, b the span of the airfoil, $|\mathcal{L}|^2$ an expression for the unsteady lift function and $\Phi_p(\omega)$ wall pressure spectrum.

$$S_{pp}(x, 0, z, \omega) = \left(\frac{\omega c z}{4\pi c_0 \sigma^2}\right)^2 \frac{l_y(\omega) b}{2} |\mathcal{L}|^2 \Phi_p(\omega) \tag{2.7.9}$$

With this relation is can be assessed that the far field noise is dependent on the wall pressure spectrum $\Phi_p(\omega)$ and the spanwise correlation length $l_y(\omega)$. The wall pressure spectra can be obtained by a single microphone in the trailing edge of an airfoil, the second parameter can be obtained by the integration of the equation in (2.7.10). Here $\gamma^2(\omega, \Delta\xi_y)$ is the squared coherence between a microphone pair in the trailing edge, with a distance of $\Delta\xi_y$ between them.

$$l_y(\omega) = \int_0^\infty \sqrt{\gamma^2(\omega, \Delta\xi_y)} d(\Delta\xi_y) \tag{2.7.10}$$

Amiet's theory states, that the obtained far field noise is a function of the wall pressure spectrum (Φ_p). This can be useful in the assessment of the influence of the test sections. When similar wall spectra are obtained in different test sections, together with no (or similar) test section influence on the far field noise, the SPL should be the same. In this way, far field noise differences can be related to the test section itself, obtaining the test section influence.

2.8 XFOIL Simulations

XFOIL is an interactive program that can be used to simulate a subsonic flow over an airfoil. 2D airfoil contours can be defined, and with the inputs Reynolds and Mach the pressure distribution, lift and drag characteristics, and boundary layer parameters can be calculated. XFOIL is a result of an MIT project in the 1980s designed by Mark Drela [21], and is based on the same aerodynamic principles given in .

2.8.1 Pressure coefficient

Regarding the pressure coefficient (C_p) (2.5.9), first the influence of a natural versus a forced transition is given. Then the influence of the Angle of Attack (AoA) is shown.

Natural and forced transition
Figure 23 shows the pressure coefficient for the three different airfoil simulated by XFOIL. Figure 23a shows the C_p for a forced transition, 23b shows the natural transition of the airfoils. Both types are shown to visualise the laminar separation bubble in the pressure coefficient plot. For all three airfoils a laminar separation bubble is present. Characteristics like the point of separation, are unique for each airfoil. A tripping device is simulated at 5% of the chord, the AoA is zero and the free stream velocity is 30 m/s ($Re = 3.97 * 10^5, M = 0.09$).

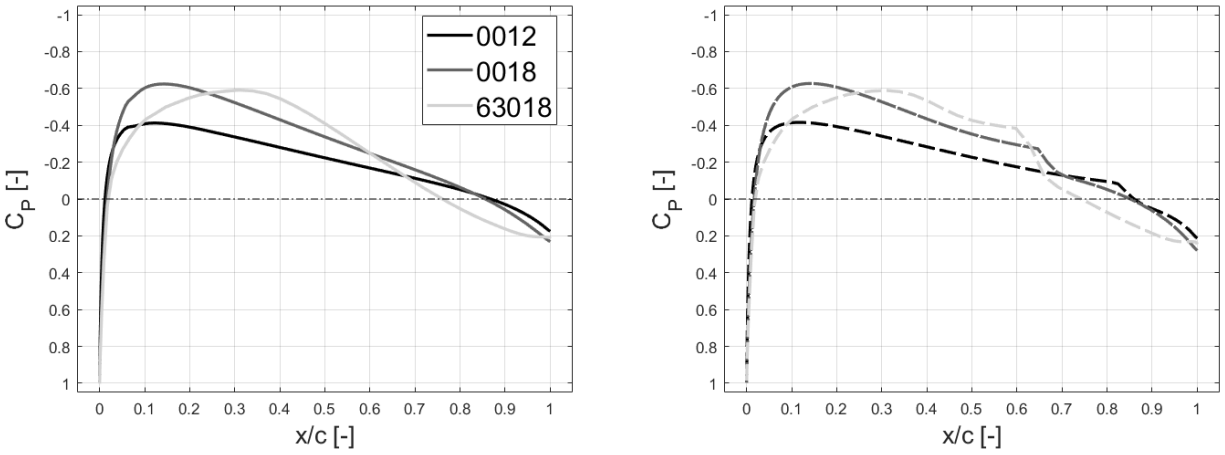

(a) Tripped boundary layer. **(b) Natural Transition.**

Figure 23: Pressure coefficient, natural transition vs. a tripped boundary layer (U_∞=30m/s and AoA=0°).

Most values are negative, this is due to the relation of the pressure coefficient. The pressure difference between the surface and the freestream ($p(x/c) - p_\infty$), is divided by the dynamic pressure (q_∞). In general $p < p_\infty$ resulting in mostly negative values for C_P, beneficial for the resulting lift force. This is due to the the acceleration induced by flow because of the airfoil geometry. According to Bernoulli [8], higher velocity results in lower static pressure. Looking at the relation of C_P, this also means that changing the velocity in the XFOIL simulation does not affect the shape of the C_p curve. This because the coefficient refers to q_∞ (y-axis values must be changed). It seems that only one line from LE to TE is plotted, this is not true. C_P values are calculated for the pressure and suction side, only those two lines overlap because the airfoils are symmetrical and the AoA is zero.

Regarding the 4-digit NACA profiles, the thicker airfoil has a slightly higher C_P at $[0.04 < (\frac{x}{c}) < 0.84]$. So the flow velocity is affected in a higher rate, originating form the geometry. More particles flowing around the NACA0018 are influenced by the presence of this airfoil in comparison to the NACA0012. So the thicker airfoil encounters a higher (more negative) pressure coefficient than the thinner airfoil, at the same x/c. The decay of the NACA0018 over the chord length is also higher, corresponding to the higher decade of the airfoil geometry

itself. The NACA63018 has a slightly different curve in the beginning of the plot, originated form the curvature near the leading edge. This airfoil is designed in such way that the position of minimum pressure is located at 0.3 x/c, this is also more or less the case. This peak value is also similar to the peak of the NACA0018, which has the same thickness. For all three airfoils a laminar separation bubble is present in the natural transition case due to an unstable shear layer. Applying a trip results in a turbulent boundary layer and no laminar separation bubble. Figure 23b shows that characteristics such as the point of separation and reattachment, are completely different for all three airfoils. This is due to the geometry, resulting in a different build up of the boundary layer and thus boundary layer characteristics.

The influence of the Angle of Attack

The AoA influences the C_p around the airfoil, this is shown in Figure 23. Three different angles for a tripped NACA0012 are simulated. It shows that the C_p increases (more negative) when the AoA becomes higher. For all three cases the flow is not separated, indicated by the curve returning to zero at the trailing edge. Mainly the values on the leading edge show different values in the pressure coefficient. So a higher AoA results in a larger portion of the flow pushing the airfoil upwards increasing the lift, but also the drag increases trying to push the airfoil upstream. This results in different values for the lift, drag and moment coefficients when the AoA is changed.

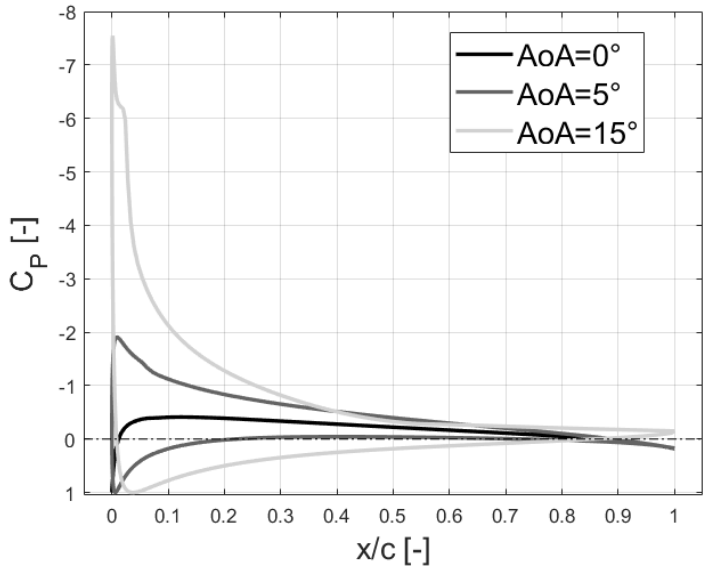

Figure 24: Pressure coefficient for the NACA0012 different AoA (U_∞=30m/s, $x_{tr.p}$=0.05 and $x_{tr.s}$=0.05).

2.8.2 Lift and Drag Characteristics

Values for the aerodynamic coefficients and other important parameters for all three airfoils are given in Figure 25, important phenomena are listed below.

- The lift coefficient for different AoA is given in Figure 25a. It can be seen that the lift coefficient increases when the AoA becomes higher, this is due to the increased lift force. The angle where C_L is at its maximum can be described as the *stall angle*, here a large wake with recirculation zone is created and the the flow is in stall. For the NACA0012 the flow is stalled at 12.5°, for the other two airfoils this phenomena occurs at 16.5°. Also an increase of the drag coefficient is visible in Figure 25b. Increasing the AoA even further results eventually in complete separation of the flow, from this point both the lift - and drag coefficient shows a linear behaviour.
- Regarding C_D, this graph shows that the drag mainly consists out of pressure drag (pressure drag coefficient C_{DP}), and is not determined by the shear stress distribution.
- The moment coefficient (Fig. 25c) shows both positive and negative values, meaning clockwise and counter-clockwise moments when the AoA changes. Both the stall angle and separation point can be retrieve from this graph.
- Increasing the AoA results in a shift of the transition point (Figure 25d). It is found that the flow becomes turbulent at an earlier stage on the airfoil at the top/suction side. For the bottom/pressure side, the flow will become turbulent at a later stage. The C_P increases at a higher AoA at the pressure side, making it harder for the Tollmien-Schlichting waves to grow, and to become turbulent. Turbulent structures and especially flow separation results in a thicker boundary layer.

  Regarding noise, a thicker boundary layer results in more noise. This can also be seen in (2.7.9) based on Amiets theory, and the equations from Brooks [12]. Regarding non-zero AoA, due to the thicker boundary layer on the suction side of the airfoil, the trailing edge noise is always dominated by the noise coming from this side.
- In Figure 25e C_L is plotted versus C_D. A high lift force with low drag would be most beneficial, so mainly operating in the left top region would be favorable. After that the lift decreases, with an increasing drag. This can also be showed as the ratio of lift over drag (Fig. 25f), most optimal conditions lay around 5-8°. Aircraft wings are designed with the most optimal ratio, regarding wind turbine blades it is less of a problem when the ratio is slightly lower. Operating above this most optimal ratio, results in a higher rotational speed, and a slightly more structurally loaded and deflecting wind turbine blade. This would not be beneficial.

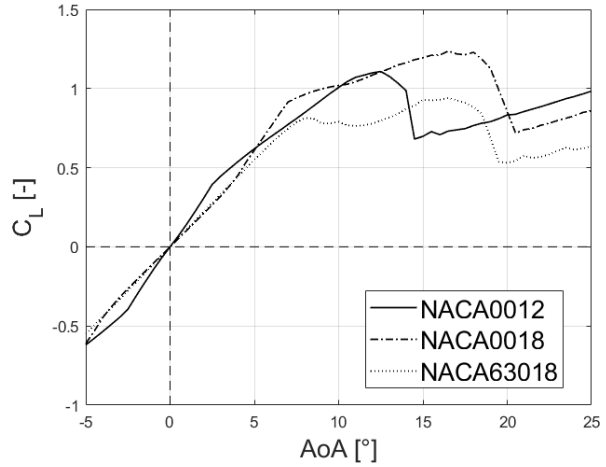

(a) Lift coefficient vs. AoA.

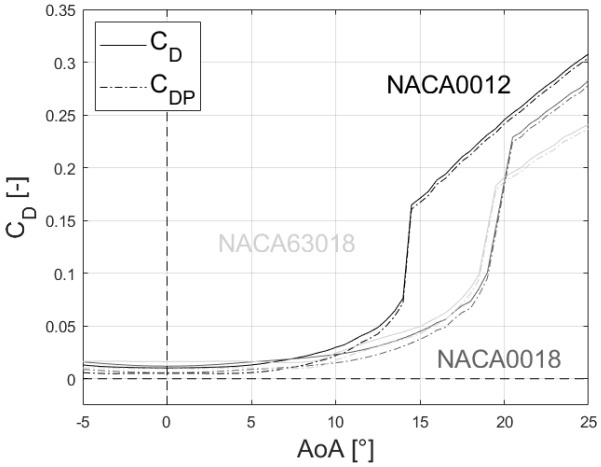

(b) Drag Coefficient vs. AoA.

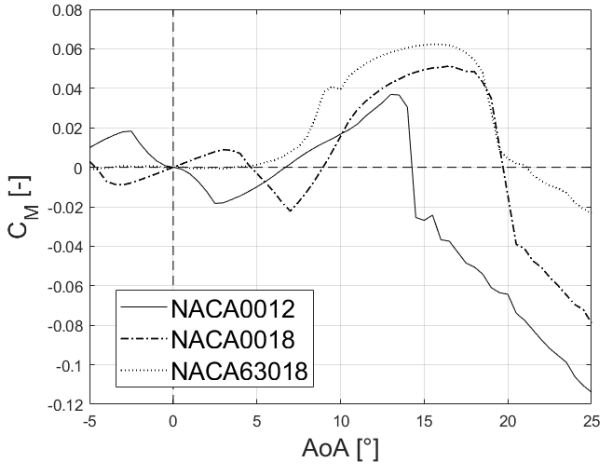

(c) Moment coefficient vs. AoA.

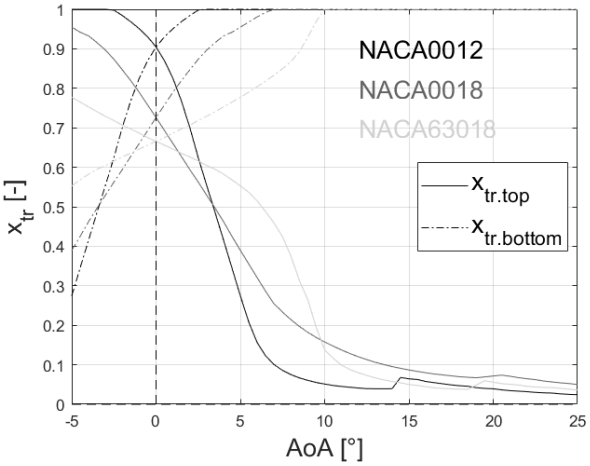

(d) Transition point vs. AoA.

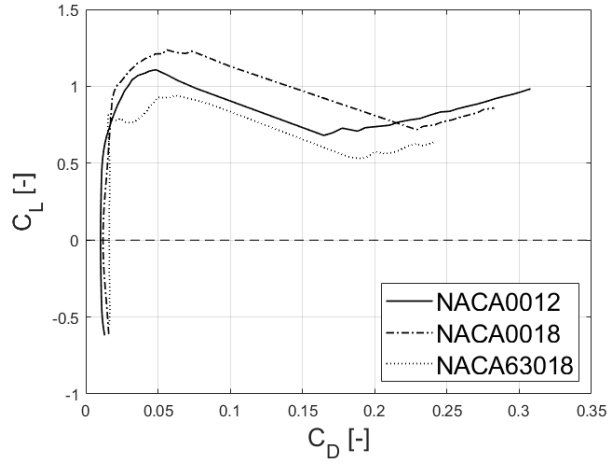

(e) Lift - vs. drag coefficient.

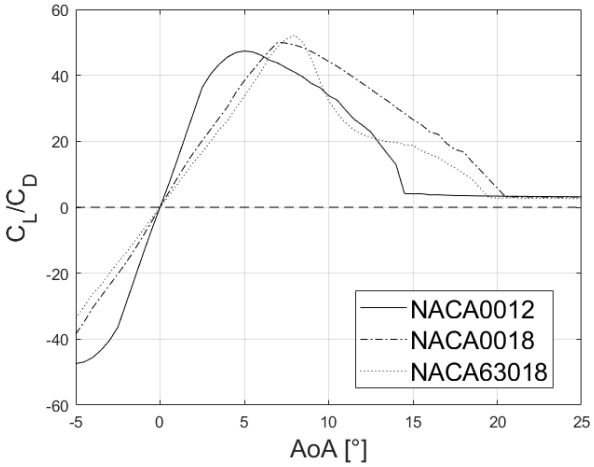

(f) Ratio of C_L/C_D - vs. AoA.

Figure 25: Aerodynamic characteristics (Natural Transition, U_∞=30m/s).

2.8.3 Boundary Layer Parameters

Boundary layer parameters (δ^* and θ) are retrieved from XFOIL, and the boundary-layer disturbance thickness (δ) is calculated with (2.4.17). The development of the boundary layer is given in Figure 26, here the blue line represents the top side, red the bottom side, and yellow the boundary layer in the wake. As already mentioned, the boundary layer disturbance thickness is an important parameter for the prediction of the trailing edge noise of airfoils. In this way, already an indication of the noise propagation from the TE, for different AoA can be made.

Figure 26a shows that for the top side (blue), the boundary layer is increasing along the airfoil. A positive AoA results in a thicker boundary layer along the top (suction side), while for an AoA of $-5°$ δ is thinner (pressure side). The same principles occur on the bottom side, but the other way around. Positive AoA will decrease the boundary layer because now this is the pressure side. At the trailing edge, first δ shows a small increase and then settles in the freestream. For all AoA also a sudden bend in the boundary layer is visible (especially at 0°) originating from the transition point. In Figure 26b also higher positive AoA are included in the graph. This shows a different behaviour of the development of the boundary layer. It was found that the flow was stalled at 12.5°, and completely separated at 14.5°. At the top side, this results in a negative gradient after separation. At the bottom (suction side) the boundary layer is even further decreased. Regarding the boundary layer in the wake, higher AoA redirect the flow further away from the center line moving the particles away from the airfoil.

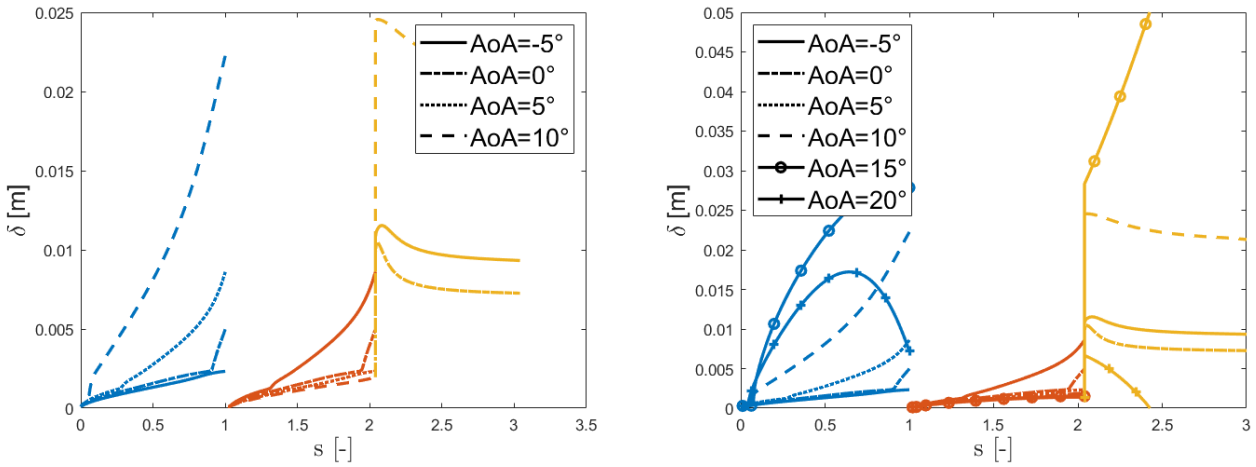

(a) δ $[-5° \leq AoA \leq 10°]$ **(b)** δ $[-5° \leq AoA \leq 20°]$

Figure 26: Development of the boundary layer disturbance thickness, NACA0012 Natural Transition, U_∞=30m/s.

2.9 Exit Nozzle Noise Reduction

As stated in Chapter 2, noise coming from the flange coupling of the CTS contaminated the results. So a solution for this unwanted noise source must be made, and proper results can be obtained. A lot of literature about different noise reduction techniques for airfoils is already present. These techniques to reduce airfoil noise, can also be used to lower the unwanted noise coming from the flange coupling. Multiple airfoil noise reduction techniques will be discussed, compared, and in the end noise reducing strategies will be designed to reduce the unwanted noise source.

2.9.1 Airfoil Noise Reduction Techniques

In this section, the most important techniques with their potential are given and explained. These airfoil noise reduction techniques are; serrations, finlets, rails and brushes. Other noise reduction techniques like; acoustic liners, sound absorbing textiles, additional porous structures and perforated plates are briefly discussed.

1. Serrations
The use of *serrations* attached to the TE of a wind turbine blade is the most mature, and well studied noise reduction technique. This pointy structure has often a sawtooth geometry, and can reduce the SPL of the noise over 10 dB at certain frequencies. The serrations are breaking the interference between radiated acoustic pressure waves, reducing the trailing edge noise.

Oerlemans [6] carried out acoustic field measurements on a 94m diameter wind turbine, with one standard blade, one blade with an optimized airfoil shape, and one standard blade with trailing-edge serrations (with four serration configurations, see Figure 27a). Under normal condition, an overall noise reduction of 0.5 and 3.6 dB were obtained for the optimized - and serrated blade respectively. The noise reduction increased with increasing wind speeds. Noise reduction up to 5 dB was measured at the lower frequencies (Fig. 27b). Although at higher frequencies the tip noise was slightly increased, the SPL was significantly reduced for the serrated blade without adverse effects on the aerodynamic performance. Oerlemans suggested flexible trailing edge brushes for more noise reduction.

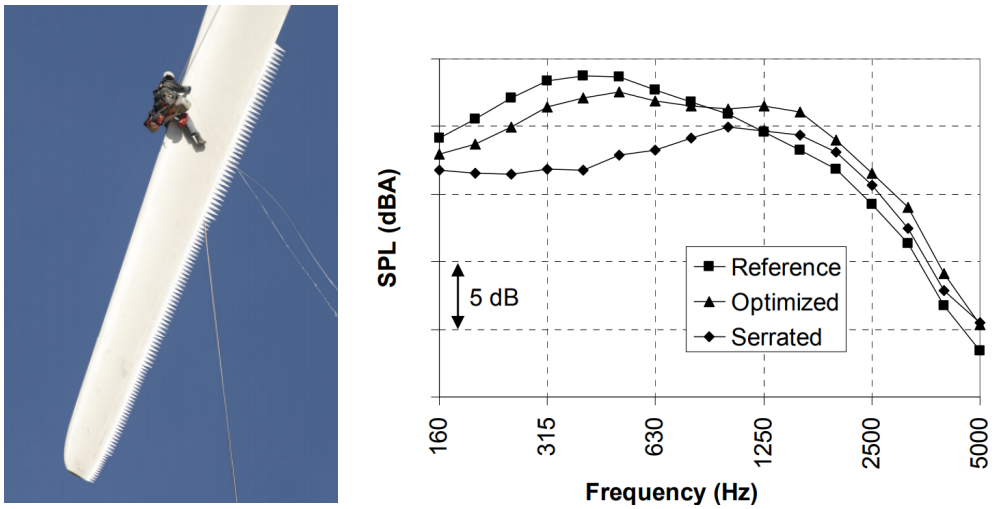

(a) Climber on top of serrated wind turbine blade.

(b) SPL, averaged over all wind speeds (6-10 m/s).

Figure 27: Reduction of wind turbine noise by TE serrations, from [6].

As can be seen from Figure 27a, multiple configuration of the serrations are used on the span of the wind turbine blade. Designing TE serreation in the most optimal way requires in depth research about the different parameters. In the following section, the most important parameters are briefly discussed and defined by substantial academic research.

Design parameters for trailing edge noise reducing serrations are;

1. Aspect Ratio, proportion between the width and height of a single serration.
2. Shape function of the serrations.
3. Alignment with the airfoil.
4. Serration length, extended airfoil length.
5. Thickness of the serrations.
6. Material.

Aspect Ratio

Sanders et al. [22] executed airfoil trailing edge noise measurements in all three configurations of the UT wind tunnel. Two configurations of serrations were used on the NACA0012 and NACA0018, shown in Figure 28a. Previous studied showed that the optimal Aspect Ratio (AR) is, AR = 1 : 2 [23]. A serration length of 10% and 20% of the chord was used, defining the amplitude and length. In general, the output (Figure 28b) shows a noise reduction between 0-7 dB, with a peak of 12 dB around 2000Hz for the open-jet test section (U_∞=50 m/s).

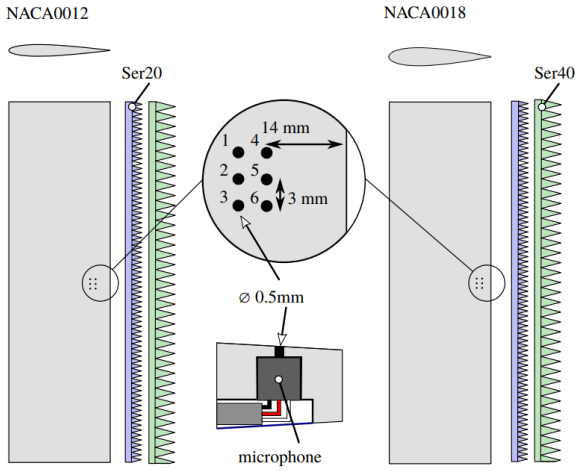

(a) Airfoil instrumentation, and serration geometry.

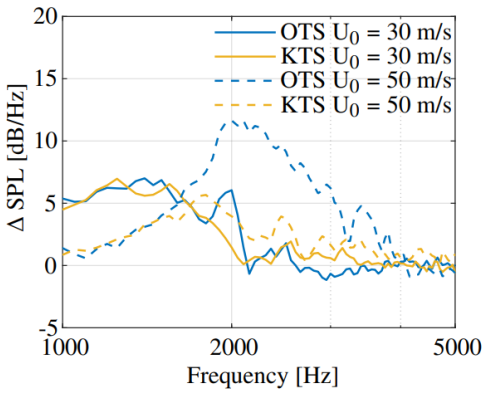

(b) Measured noise reduction for the Ser20, in the open-jet and kevlar®-wall test section.

Figure 28: Airfoil TE noise measurements in the UT wind tunnel, a benchmark-case [22].

Shape function

The sawtooth geometry is the most implemented geometry of the serration. Literature regarding simulations with other shape function are available, and are showing promising results for an additional noise reduction. A paper published by the university of Delft [24] compared the sawtooth geometry, with a more curved serration, the iron geometry (Figure 29). Attached to the TE of the NACA0018, this results (based on simulation) in the noise in a far-field noise reduction of approximately 2 dB at certain chord based Strouhal numbers [$5 > St_c > 15$].

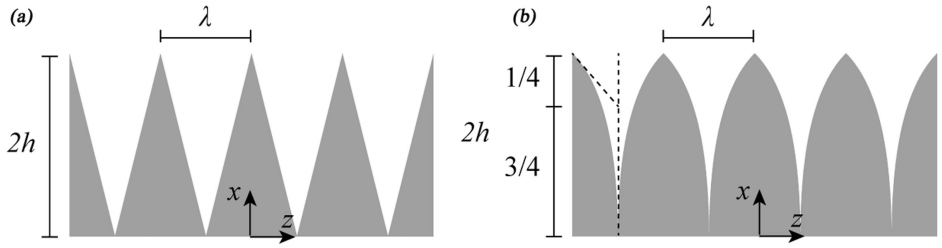

Figure 29: Sawtooth (left), and Iron geometry (right) [24].

Published in 2020, Kholodov [25] states that: "the sharper the serrations are, the higher the noise reduction is". In this paper, the influence of the shape curvature, slits, and the combination of the two affecting the noise from a serrated airfoil is assessed (based on Ayton's analytical model). Multiple slit configuration where analyzed, concluding that more slits will result in more noise reduction. Regarding the shape curvature, the sharper the serration, the more noise was reduced. The final optimization for the serrations, with both slits, and different shape curvatures, are given in Figure 30.

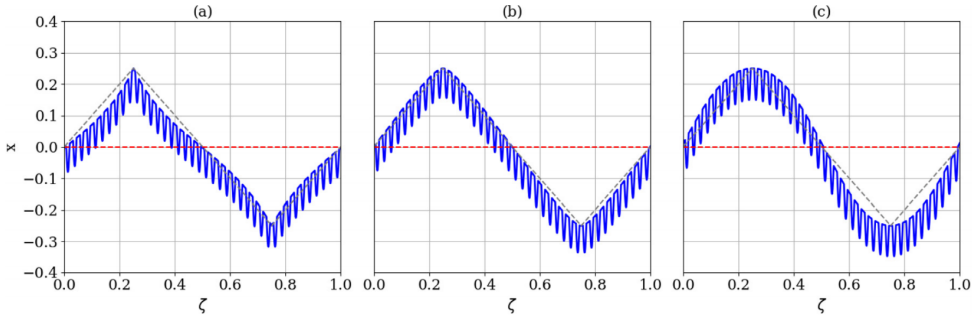

Figure 30: Serration geometry, with slits and different shape curvatures: (a) l = 0.01d ,(b) l = 0.1d and (c) l = 0.2d [25].

SPL output of the simulations without slits, resulted in a maximum noise reduction of 21 dB, 4 dB, and 2 dB, for (a),(b) and (c) resp. (compared with a straight TE). The additional noise reduction due to the presence of the slits is given in Figure 31. This shows the gained noise reduction for each case compared to this shape curvature without slits. This results in an additional noise reduction between 8-10 dB around 5000-6000 Hz.

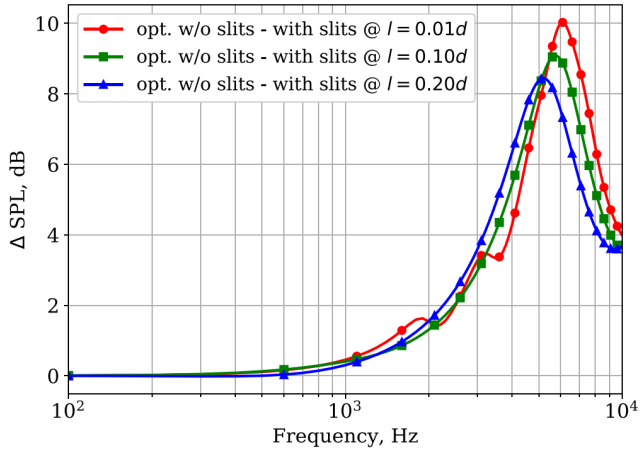

Figure 31: Additional noise reduction, by the slits [25]

Although this publication shows promising results involving serrations with slits. This is a stand alone research itself, and will not be covered in this report due to time constraints. It also based on an analytical model, and experiments from Moreau [26] show different results. Here the noise reduction from narrow and broad serration ($AR_N = 1:10$ and $AR_B = 1:3\frac{1}{3}$) of a flat plate with low-to-moderate Reynolds is assessed. Resulting in a higher noise reduction with the broad serration, and in poor agreement with the theory and assumption of Kholodov stated on the top of this page.

Alignment

Serrations reduce the broadband component of the noise, but sometimes increase the noise at higher frequencies. This can be originated from the alignment of the serration.

Leon et al. [27], investigated the serration-flow misalignment on the noise emissions. This resulted in experiments with multiple serration flap angles (φ), using a serrated NACA 6512-10 airfoil (Figure 32a). The SPL results are given in Figure 32b, and show that the most optimal alignment with the airfoil is at $\varphi = 0°$, for all angles of attack. A crossover frequency (f_c) is introduced at higher serration flap angles. At $\varphi = 6°$, the lower frequencies are still reduced, but after f_c the SPL is even higher compared to the straight TE (without serration), so not beneficial.

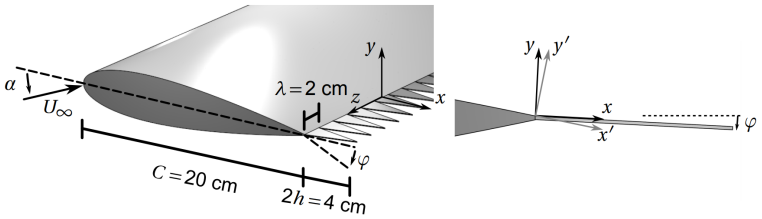

(a) Schematic representation, AR=1:2, and a length of 20% of the c.

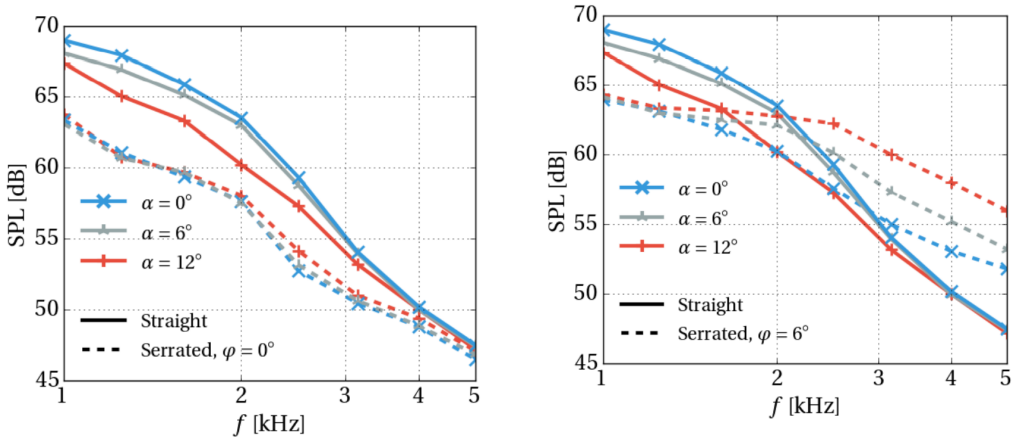

(b) SPL at multiple AoA, φ=0° (left) and φ=6° (right).

Figure 32: Serration flap angle [27].

Length

Previous results showed that often a serration length of 10% to 20% of the chords was used. From Figure 27a it can be deducted that Oerlemans used a shorter serration length, at higher flow velocities (towards the tip).

Thickness and Material

Regarding the thickness, it is important that the serration can withstand the forces applied by the flow, so this depends on the material. [27] used a constant serration thickness of 1mm. Often non high-end steel is used.

The influence of TE serrations on wind turbines is assessed by Llorente and Ragni [28]. Experiments have been carried out with a Nordex ADO30 and a NACA64$_3$418 in a wind tunnel. The lift coefficient for both airfoils is increased by serrations, especially around the region at maximum C_L. The drag coefficient (C_D) is negligibly increased, resulting in an overall increased airfoil performance. Loads are increased within a 5% margin from the mean loading, power variations up to 1% respect to the original where assessed.

2. Finlets

The effects of streamwise surface treatments on trailing edge noise is assessed by Abbas et al [29]. The influence of *finlets* on the noise emitted from a tripped long flat-plate model was measured. Multiple configurations of these finlets where used (Figure 33). Finlets will reduce the eddy convection velocity, resulting in lower noise emissions.

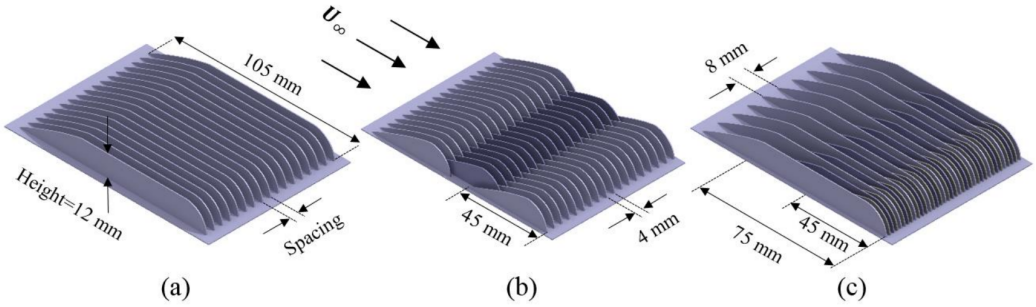

Figure 33: Various surface treatment configurations: (a) 2D standard configuration, (b) 3D staggered configuration, (c) 3D gradual-change configuration [29].

Results showed that these staggered configuration did not have an additional noise reduction in comparison with the 2D standard configuration. Staggered configuration do increase the manufacturing complexity. Trailing edge noise reduction up to 10 dB is reached, especially at the mid to high frequencies. The right plot in Figure 34, even shows an increase at the lower frequencies when a spacing (S) of 1-4 mm is used. The left plot does not show this phenomena. Optimal spacing lays between 8-12 mm.

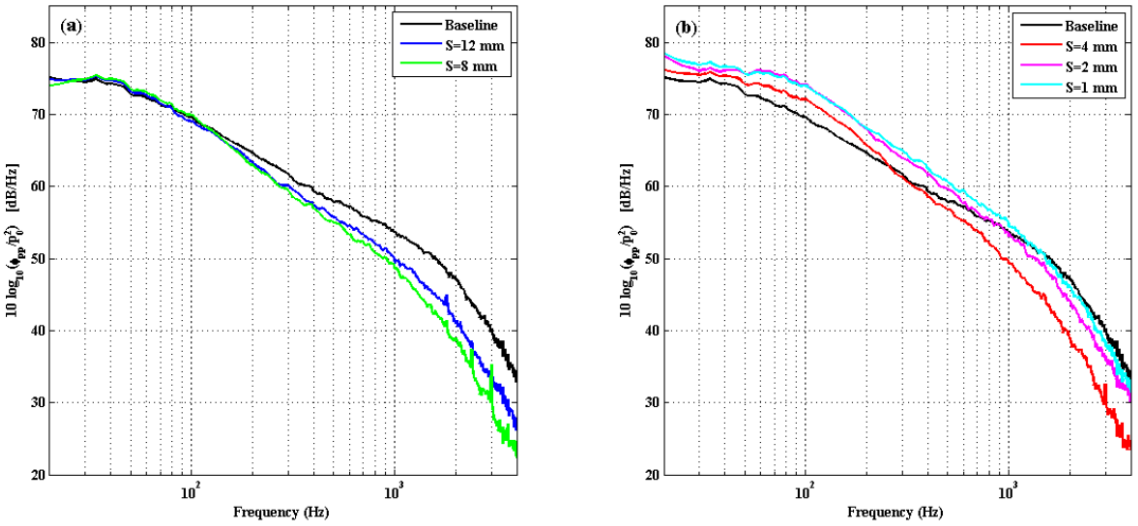

Figure 34: Finlet spacing influence on the surface pressure PSD (2D standard configuration) [29].

Clark [30] executed measurements on a tripped DU96-W180, with Re_c up to 3 million, at multiple AoA. Multiple variations in finlet spacing, height and thickness where applied in these experiments. Resulting in a optimal height between 8 to 12 mm, and an optimal thickness around 2mm.

3. Rails

Clark [30] also used this same airfoil to examine the noise reduction by the use of *rails*. This literature is based on bio-inspired noise control, and this concept originates from flight feathers of many owl species.

Experiments with varying design parameters (height, spacing, extension and diameter) for the rails were executed. The SPL is especially reduced in the frequency domain between 1500 and 4000 Hz. But in general, this resulted in no better noise reduction compared to serrations or finlets. Especially in the high frequency domain the SPL becomes higher. Here the noise is produced by smaller turbulent eddies, suggestion that these eddies can still grow underneath the rails, emitting noise. Although, for the case with $Re_c = 3e6$ and $\alpha = 6.9°$, the noise reduction regarding rails is higher in comparison with finlets. Another downside for rails is there complex structure.

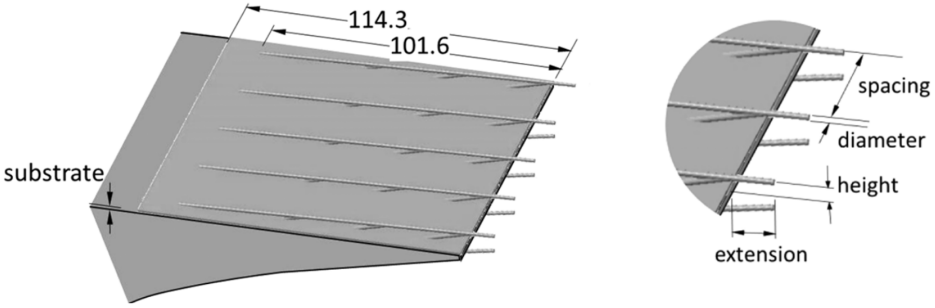

Figure 35: Rails applied at the TE of the U96-W180 model[30].

4. Brushes

Broadband noise reduction with trailing edge *brushes* is investigated by Finez [31]. Experiments were conducted on a NACA65(12)-10 airfoil, with different trailing edge brushes. Variations on fiber properties were used (length, diameter and density). The different brushes that are attached at the TE are represented in Figure 36a. This research showed only a broadband noise reduction of 0.5 dB, up to 3 dB around 1000 Hz. The pressure spectral density is given in Figure 36b. The suggestion was made that the span wise fibers of the brush, disorganize turbulent structures before they can radiate sound.

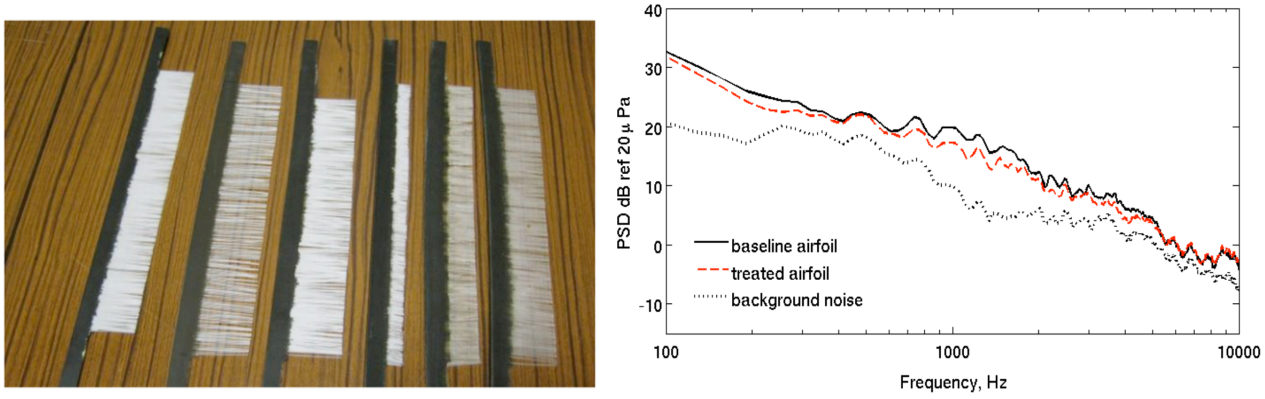

(a) Different TE brushes. **(b) Acoustic PSD in the far field, U_0 =30 m/s and α =10°.**

Figure 36: Broadband noise reduction with trailing edge brushes [31].

Finez also states that the literature from Herr et al. [32] [33], about TE brushes on both, a flat plate and a NACA0012 airfoil, showed a broadband noise reduction of 10 dB (regarding TBL-TE, LBL-VS and bluntness noise). But none of the academic papers from Herr are present at the accessible databases.

5. Substrates

Clark [30] also assessed the influence of a *substrate* on the airfoil model. These samples are given in Figure 37. The overall sound levels for these substrates where increased up to 1.4 dB. Increasing the height of the substrate increase the noise emitted. Between 1000Hz and 2000Hz the SPL becomes slightly higher, when $f > 2000$ Hz the SPL is marginally lower in comparison to the case without a substrate. Another downside of this substrate is that it influences the boundary layer, affecting the aerodynamic properties. This also indicates the importance of a smooth surface.

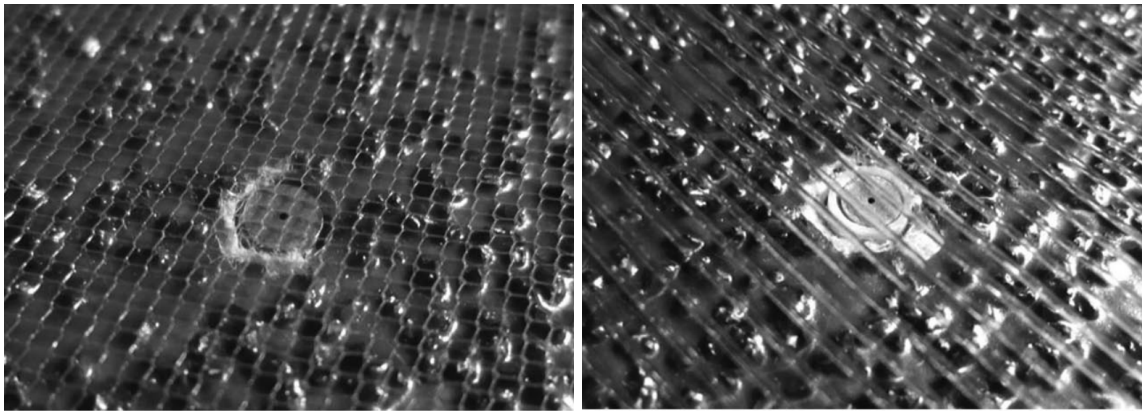

(a) Multi directional fibers. **(b) Fibers oriented only in the flow direction.**

Figure 37: Substrates used by Clark [30].

6. Acoustic Liners

Acoustic liners are used to reduce the noise, and often used in aircraft engines. Noise is reduced by partially absorbing the energy in the sound wave by applying an acoustic liner. A schematic view of is given in Figure 38a. An acoustic liner is often a sandwich panel (A), consisting out of a porous top layer for protection called face-sheet (B), a honeycomb structure providing internal partitions for energy/noise absorption (C), and an impervious layer called back-sheet (D). A more simplistic acoustic liner is given in Figure 38b. This Flamex PU, consists out of a oil, dust, dirt, and moisture-proof polyurethane top layer, and a sound-absorbing melamine foam. Corresponding absorption coefficient of a Flamex PU sample, with a thickness of 25 mm is given in Figure 38c.

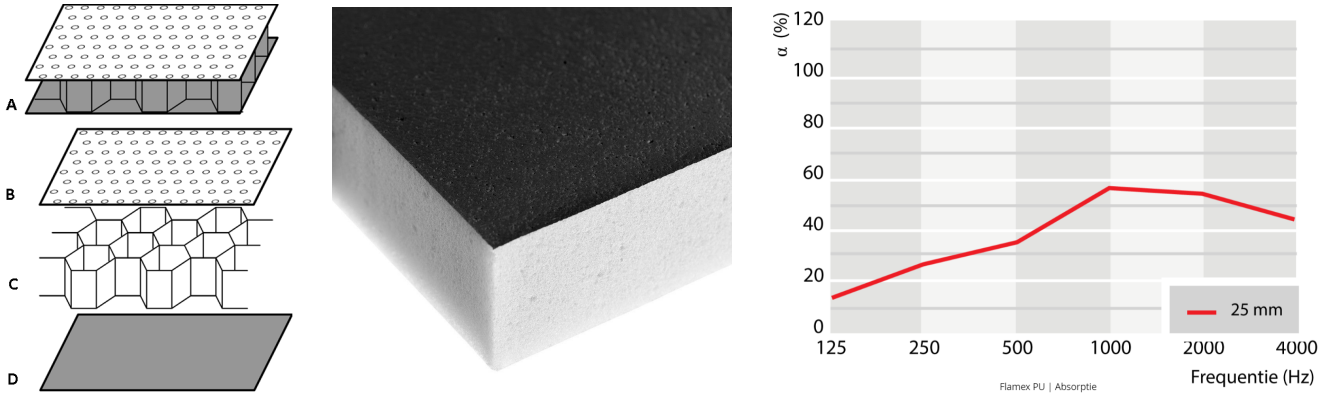

(a) Schematic view. **(b) Flamex PU.** **(c) Absorption coefficient.**

Figure 38: Acoustic liners, from www.akoestiekwinkel.nl.

7. Fabrics

Noise reducing *fabrics* are often used in building acoustics, for example in acoustic panels often combined with an air cavity. Similar to acoustic liners, part of the energy in the acoustic wave is absorbed. Sound absorption of textile fabrics is discussed by Atiénzar-Navarro [34]. This paper showed the importance of an air cavity when sound absorbing fabrics are used, this significantly increased the absorption coefficient. Segura-Alcaraz [35] investigated the influence of a woven fabric structure on the acoustic absorption. It showed that with the appropriate combination of warp and weft densities, the absorption coefficient can reach values close to 1. The mass effect of the pores in the woven structure increases the absorption at lower frequencies.

Pile-fabric materials can also be used to reduce the noise inside of academic wind tunnels, and proved to be working quite well. This fur-like material with fibers of approximately 10 mm long can be used to reduce the noise. These fibers disturb the growing vertices near the surface, partially eliminating the accelerating and decelerating vertices which scatter noise. Techniques of reducing aerodynamic noise in 3/4 Open Jet Wind Tunnels is researched by Kudo [36], using pile-fabric in the collector of the wind tunnel to reduce the background noise during experiments. This resulted in an overall reduction of 1dB, but resulted in a small pressure loss over the collector.

8. Curved wall

Kudo [36], used different edges for the the exit nozzle of the wind tunnel floor to assess the influence on the noise. The half ellipse edge showed better results in comparison to a quarter ellipse, this due to a more gradual development of the boundary layer. A similar curved wall can be used at the end of the closed wall test section of the UT wind tunnel to reduce the noise.

9. Other

Other noise reduction techniques that are frequently used but not so effective, are the concepts of a perforated plate and porous materials. Teruna [37] investigated multiple porous structures on the leading edge of a NACA0012, resulting in an overall SPL reduction of 1.2 and 0.8 dB. Although the use of porous structures can decrease the noise, for this case (and multiple other situation) this results in a decrease of the lift coefficient. Possible Noise Reduction Techniques for the exit nozzle are given in Figure 39.

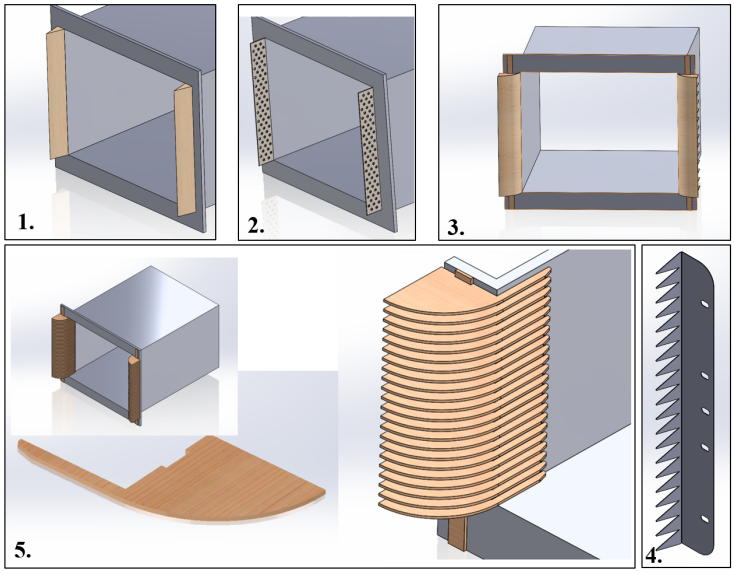

Figure 39: Possible Noise Reduction Techniques for the exit nozzle: (1) Additional (porous) structure, eliminates bluntness noise. (2) Noise reducing perforated plate (3) Curved wall, a quarter ellipse structure. (4) Stacked corner finlets. (5) Exit nozzle Serration.

PART II, METHODOLOGY

3 Methodology

3.1 Experimental set up

This chapter contains information about the experimental set-up. The working principle of the aeroacoustic wind tunnel is given, differences between the test sections are mentioned, and the used instrumentation will be shown. Experiments are conducted in the A2 aeroacoustic wind tunnel of the University of Twente. A schematic view of the wind tunnel is presented in Figure 40. It is a closed-circuit wind tunnel with a window section of 0.7m x 0.9m (height vs. width) entering the closed test section. Radial turbines move the airflow in clockwise direction, powered by a 130kW electrical motor. A heat ex-changer and acoustic damping panels discharges/absorb the unwanted effects from the turbines. The flow is made laminar when it passes through the settling chamber, then the flow goes through anti-turbulence grids where it afterwards is contracted and then sent to the closed test section. After the anechoic chamber the stream is recollected again, and goes through the collector and a closed system is formed. Here additional acoustic damping material is applied to reduce the reflection of the corner vanes. These vanes are guiding the are flow in the corners.

An anechoic chamber with dimensions 6×6×4m is given in Figure 41(anechoic environment for frequencies of 160 Hz and above). Acoustic insulation foam wedges are applied on the walls and ceiling. Acoustic foam is also applied on the floor, supported by metal grids enabling people to walk inside the chamber. The wind tunnel has multiple test sections to execute experiments, discussed later on. The wind tunnel reaches velocities up to 60 m/s with a turbulence intensity less than 0.4%.

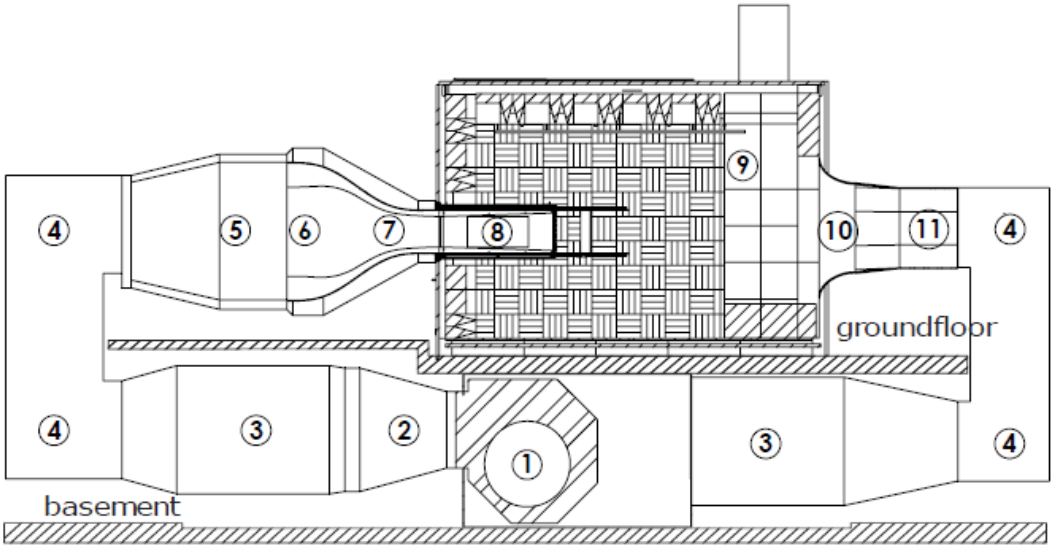

Figure 40: A schematic view of the wind tunnel of the University of Twente. (1) Radial turbines; (2) Water-cooled heat exchanger; (3) Acoustic dampening panels; (4) Corner vanes; (5) Settling chamber; (6) Anti-turbulence grids; (7) Contraction; (8) Closed test section; (9) Anechoic chamber; (10) Jet stream collector; (11) Collector. [38]

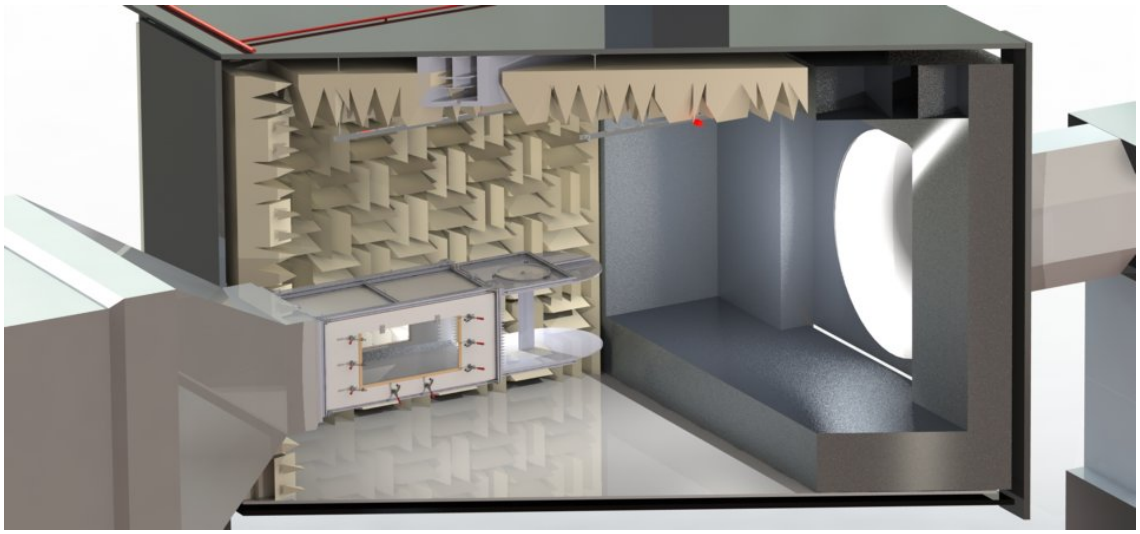

Figure 41: Anechoic Chamber of the UT wind tunnel [38].

3.1.1 Test sections

The same experiments are executed in three different test sections, in this way the influence of the test sections can be assessed. Schematic representations and photo's of the different test sections are given in Figure 42 and 43. These test sections are:

1. *Closed Test Section* (CTS)
   Acoustic wind tunnel testing started in closed test sections, where microphone phased arrays are flush-mounted on a panel in the wall. This resulted in the best possible aerodynamic free-flight conditions, but the interaction of the flow with the boundary layer near the wind tunnel walls contaminated the output of acoustic experiments. At the UT this section is $1.8m$ long. Acrylic plates are enclosing the CTS and microphones are $10mm$ recessed in a conical shaped aperture with an opening angle of 110° behind a Kevlar cloth. This aperture is used to avoid unwanted boundary layer noise (cross sectional view in Figure 44). In this way you will benefit from the aerodynamic performance of the CTS without boundary layer noise.
2. *Open-Jet Test Section* (OTS)
   Another way to circumvent this unwanted phenomena, is to use an open test section. The airfoil is placed slightly after the CTS with a microphone array at 90° from the center line, nevertheless this results in a diverged airflow reducing the aerodynamic performance. A shear layer is created refracting the sound waves propagating from the airfoil towards the microphones, an angle and amplitude correction must be applied. Refraction's occur in time and space by interaction of the sound waves with turbulent eddies in the shear layer, resulting in a correlation loss between microphone pairs in the CSM. Another disadvantage of the OTS is the deflection of the flow affecting the C_P with non-zero AoA. This results in a difference between the *effective angle of attack* (based on the pressure coefficient) and *geometric angle of attack* (the angle set in the wind tunnel). Here the C_P values are matched to set the correct effective - with the corresponding geometric AoA (explained in further detail in Section 4.7.1).
3. *Hybrid Test Section (HTS), Kevlar®-Wall*
   In the recent years also a hybrid test section is developed. Experiments where tested with the use of a tensioned Kevlar cloth as side panels in the closed test section (Figure 44a). In this way the flow can not pass through the Kevlar, but the walls are acoustically transparent. The Kevlar has a thickness of $0.12mm$ and a weight of $61g/cm^2$. In this way aerodynamic conditions are good, and sound waves can still propagate trough the Kevlar cloth to the microphone array. A similar correction using Amiet's shear layer refraction method must be applied for the boundary layer at the Kevlar.

For consistency results will be presented in the following order; OTS, HTS and CTS.

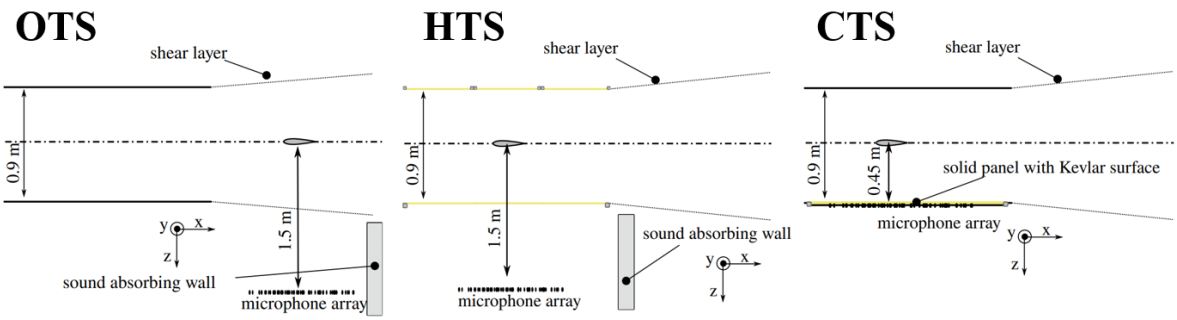

Figure 42: Schematic representation of the test sections [22].

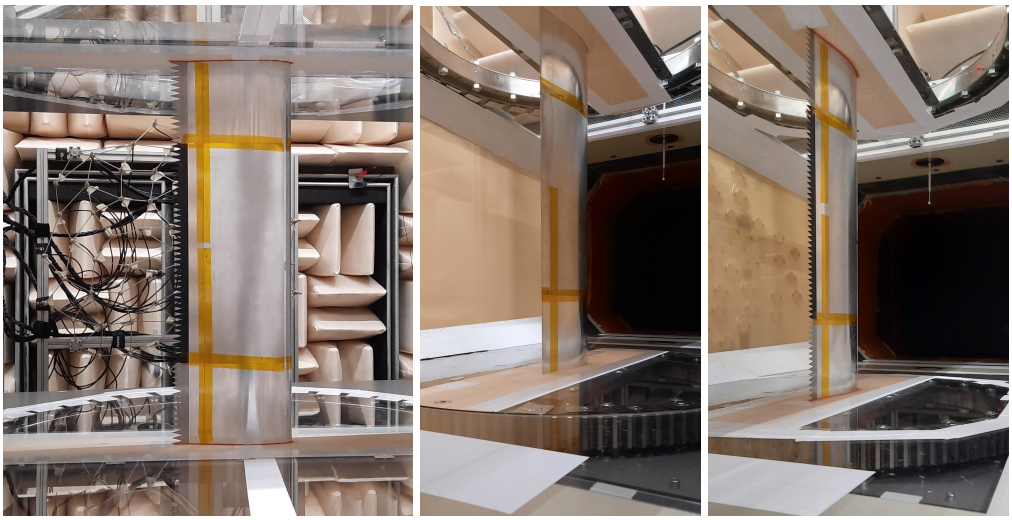

(a) OTS. **(b) HTS.** **(c) CTS.**

Figure 43: Photo's of the test sections.

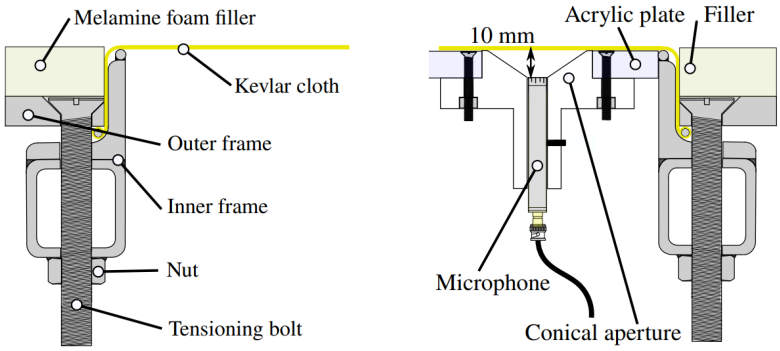

(a) HTS. **(b) CTS.**

Figure 44: Cross sectional view of the test section [22].

3.1.2 Instrumentation

The airfoils with corresponding instrumentation are given in Figure 45. The NACA0012 and NACA0018 both have a chord length of 200mm and a span of 700mm. The airfoils are equipped with six Knowles FG-23329-P07 microphones at the trailing edge to measure the wall pressure fluctuations. The pinhole diameter is 0.5mm and the holes have a spacing of 3mm in both direction, chordwise and streamwise . Two different serrations are applied at the trailing edge of the airfoil (Ser20 and Ser40), a serration length of 10% and 20% of the chord (resp. 20 and 40mm) with an Aspect Ratio of 1:2.

The NACA63018 is an airfoil consisting out of multiple parts, in this way the profile can be tested in multiple aeroacoustic wind tunnels (with different window sections) and data can be compared. The trailing edge can be changed and noise reducing serrations can be tested. This hollow airfoil has a chord of 200mm and is equipped with 28 pressure tabs, located on both sides of the airfoil. In this way also non-zero AoA can be tested. Wall pressure fluctuations can be measured with four analog MEMS microphones (Invensense ICS-40300). The microphones are spaced 5 mm apart in both streamwise and chordwise direction and are in L-shaped arranged. A pinhole diameter of 0.7mm is used.

At all airfoils two zigzag tripping device are applied at 0.05 x/c (pressure and suction side). This to make sure that the turbulent structures at the the TE are present, resulting in the most dominant airfoil self-noise type Turbulent Boundary Layer Trailing Edge Noise. A zig-zag trip of 0.5 mm height (70° and 6 mm width) is used. The wall pressure microphones are powered by the BaseTech BT-153 power supply and sampled with the NI PXIe-4499 Sound and Vibration modules.

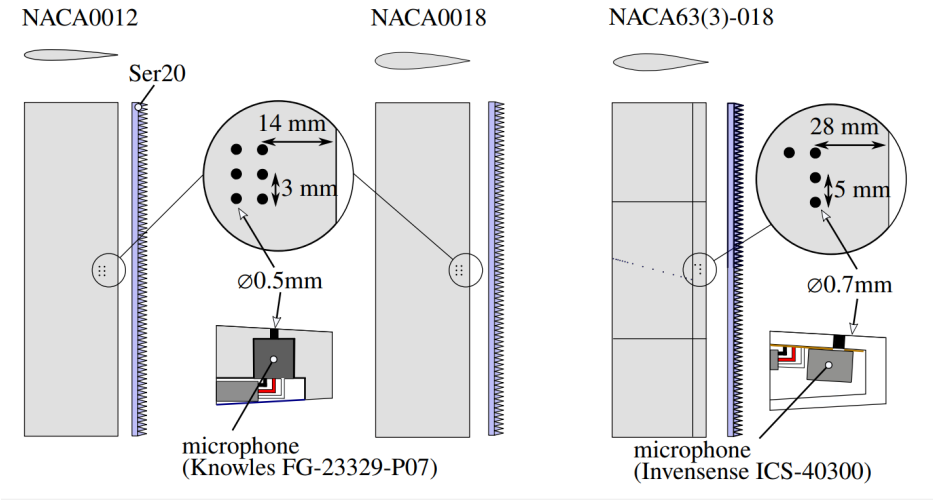

Figure 45: Airfoil instrumentation [22].

Airfoils can be mounted vertically in the test section, the experimental set-up for the for the OTS is given in Figure 46. A certain frequency must be set for the inverter, powering the motor of the radial turbines causing the air to circulate. The freestream flow velocity can be measured with the pitot tube, the pressure will be measured at two positions on the pitot and the freestream flow velocity can be calculated ($U_\infty = \sqrt{\frac{2(p_\infty - p_0)}{\rho}}$). A thermocouple is used to secure a constant temperature. Via the turntables the geometric AoA of the airfoil can be set, the gap between the turntable and the sandwich panel is now sealed. With the microphone array consisting of 62 microphones, set at a distance of 1.5m (for the OTS and HTS), the noise levels can be assessed. The distance between the microphones and the airfoils in the CTS is half of the windtunnel width +10mm (460mm). An acoustic barrier is placed between the collector and array to absorb/redirect unwanted noise coming from the collector.

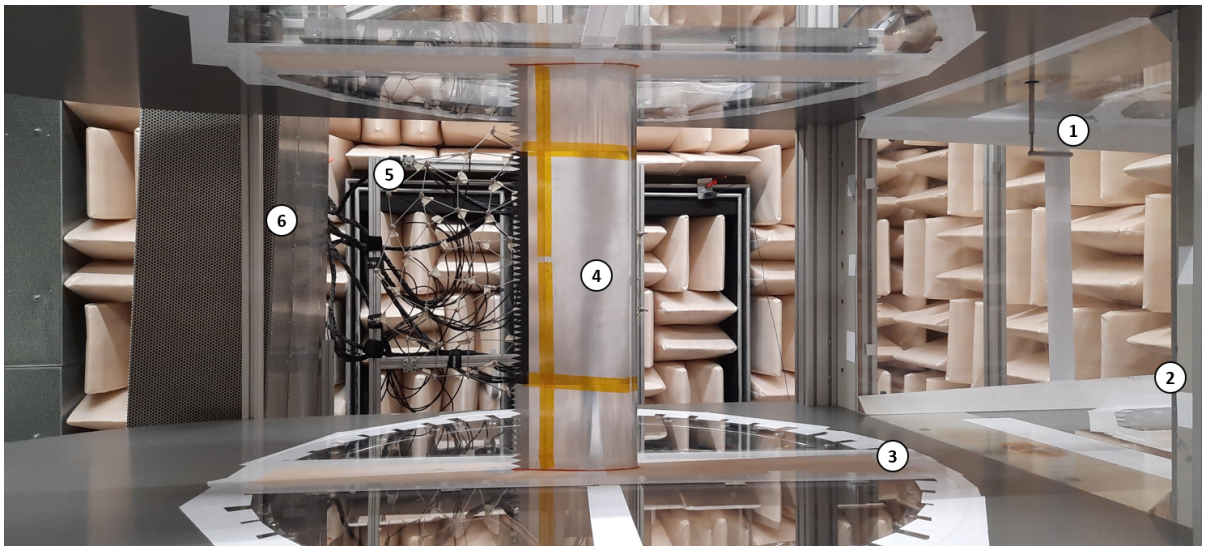

Figure 46: Experimental setup for the OTS. (1) Pitot tube, (2) Thermocouple, (3) Turntable, (4) Airfoil, serrated, (5) Microphone Array, (6) Acoustic barrier.

Regarding the far field noise, two different microphone arrays are used, microphone locations are given in Figure 47. For the OTS and KTS a spiral shaped array is used, here the microphones all have a unique distance to the center of the grid, resulting in a good localization of the noise sources. For the CTS this same array is compressed to fit inside of the wall of the closed test section of the wind tunnel. This array is designed by PhD candidate and supervisor of this project Marijn Sanders (UT). This is a new configuration for the CTS and will help to quantify and locate the noise from the TE of the airfoils in a better way. This due to the position closer to airfoil (0.46m instead of 1.5m), together with a wider angle range in relation to the trailing edge. During previous experiments the microphones were recessed 10mm behind a Kevlar cloth and flush mounted into an acrylic plate. The airfoil noise was largely disturbed by the boundary layer noise and noise from the Kevlar cloth resulting in poor results (hardware configuration for both arrays is given in Appendix C).

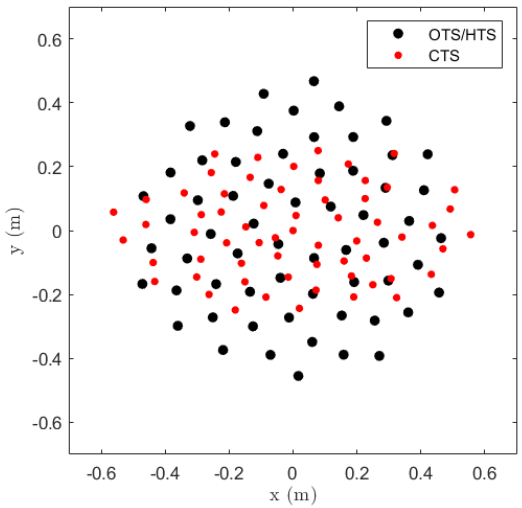

Figure 47: Microphone Array, microphone configuration.

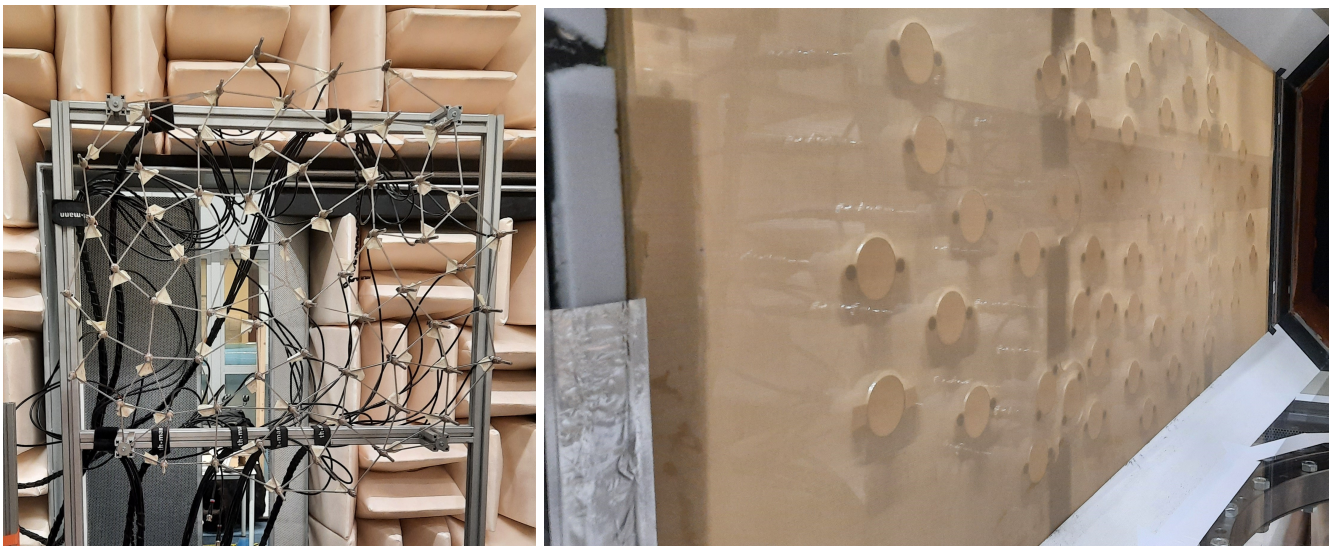

(a) OTS and HTS. **(b) CTS.**

Figure 48: Photo's of the two microphone arrays.

A schematic of the data acquisition is given in Figure 49. The sound waves coming from the airfoil towards the membrane of the microphones will result in a AC voltage, which is amplified to reduce the unwanted electronic noise. To avoid the alias effect in the converter, a low-pass filter is used. Then the timeseries of the pressure is stored in the memory of the computer. The timeseries must then be Fourier-transformed to convert it to the frequency domain. A post processing algorithm is used to analyze the acquired data, given in the next chapter.

Concluding, experiments are conducted with three different airfoils (NACA0012, NACA0018 and NACA63018) in three test sections (OTS, HTS and CTS). Far - and near field noise will be measured and in the end compared.

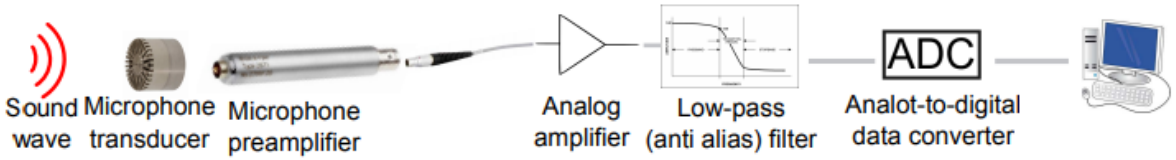

Figure 49: Data Acquisition scheme [39].

3.2 Final Design Noise Reduction Technique

After the conducted literature research about noise reducing strategies, in this section the final design for the exit nozzle noise reduction is discussed. The estimated noise reduction for all the different techniques with their design parameters are given in the Table 2.

Table 2: Noise reduction techniques and their potential.

Noise Reduction Techniques	**Δ SPL**	**Design Parameters**
1. Serrations	max.12 dB 0-7 dB (f<2000 Hz)	Amplitude, AR 1:2 Length, 10% chord Shape function, sharp sawtooth Alignment, $\phi = 0°$ Thickness, approx. 1mm
2. Finlets	max. 10 dB 5-10 dB, (2000-5000Hz)	Not staggered Spacing, 4-8mm Height, 8-12mm Thickness, 2mm
3. Rails	max. 8 dB increased SPL (f>4000Hz)	Spacing, length, diameter Height, extension
4. Brushes	max. 3 dB broadband approx 0.5 dB	Length, thickness Density
5. Substrates	increased 0-1.4 dB	Fiber direction, roughness
6. Acoustic Liner	-	Absorption coefficient
7. Fabric	broadband 1 dB	Air cavity, fiber length
8. Curved wall	-	Oval ratio, thickness

Regarding the airfoil noise reduction techniques, serrations and finlets show the most promising results. The SPL when rails are applied, are slightly increased at high frequencies. Rails also do have a more complicated design so this technique is not chosen for the final design. Brushes applied on the TE of an airfoil show only a small noise reduction, and substrates even increase the radiated noise. Because serrations can easily be applied and is effective in airfoil application, this noise reduction technique is chosen. This serration is an extension of the wall, and can be produced in a short-time frame. Regarding the last three noise reduction techniques, these will be combined into one solution, discussed in the next section.

Exit nozzle Serration

Regarding the design of the serration at the exit nozzle of the wind tunnel, the design parameters in the previous table are being used. So an AR of 1:2 with a sharp sawtooth geometry, completely align with the side walls. The serration length is based on airfoil serrations, three configuration are designed with a length of 20, 30 and 40mm. The thickness will be 10mm, so it can be clamped and bolted in the current situation.

(a) Acrylic Plate, Ser20, Ser30 and Ser40 (Solid Works). **(b) Photo of the installed serration.**

Figure 50: Exit Nozzle Serration.

Quarter Ellipse with Teddy-bear fabric

The last three noise reduction techniques, are combined into one solution. A quarter ellipse wooden structure filled with melamine foam, covered by a 'teddy bear' fabric. In this way the noise is not scattered at the flange coupling, and the fibers of the fabric interact with the boundary layer breaking the growing eddies in the flow, reducing the noise. The melamine foam can also absorbs unwanted sound waves propagating to this quarter ellipse.

Figure 51: Quarter Ellipse fabrication process. From left to right; (1) wooden structure, (2) applying melamine foam and velcro tape, (3) applying fabric (4) installed Quarter Ellipse.

3.3 Post Processing

In this chapter the Beamforming Technique is explained with underlying equations and corresponding corrections, also Source Power integration is given. Furthermore the Matlab based algorithm for this beamforming technique is explained.

3.3.1 Beamforming Technique

To post-process data acquired by microphones, a technique called Beamforming is used. This is developed by Boeing in 1994, and identifies and quantifies noise sources. It is also known as sum-and-delay or destructive, because it uses the time delay of the noise in each microphone and sum the result to create a constructive interference. This is possible because the sound wave produced by the noise source has a different phase related to the propagation distance, beamforming technique is discussed in [39].

A *Cross Spectral Matix* (CSM) (3.3.1) is used to express the correlation between two microphones. Here m and n refer to specific microphones, the term $\sigma\mathbf{I}$ is the statistical variance of the noise. In the real world the noise is always affected by unwanted phenomena; electronic interference, turbulent flow reaching the microphone, inducing the so-called pseudo noise. As the CSM gives the correlation between the microphones, the diagonal elements (auto-power) will relate the output to itself, resulting in a value equal to the statistical variance. While the off-diagonal elements are uncorrelated, so this noise will only affect the diagonal. Diagonal removal is applied to circumvent this unwanted noise. The beamforming algorithm will use Matlab, for the calculation of the CSM the most broadly used Welch method is used.

$$C_{mn} = \mathbf{E}(p_m(f)p_n^*(f)) + \sigma\mathbf{I} \tag{3.3.1}$$

A linear isentropic wave can be expressed as the Helmholtz wave equation expressed on the left side in (3.3.2), on the right the presence or absence of sound sources. The right-hand side is zero when there are no sound sources. In presence of an monopole source described by $q(t)$, the Dirac delta function $\delta(\mathbf{x} - \mathbf{x}_0)$ presents the information about the geometrical location of the source. The non-homogeneous wave equation in the free-field has the solution given in (3.3.3), where $(\mathbf{x} - \mathbf{x}_0)/c_0$ represents the retarded time (τ).

$$\left(\frac{1}{c_0^2}\frac{\partial}{\partial t^2} - \nabla^2\right) p = q(t)\delta\left(\mathbf{x}\text{-}\mathbf{x}_0\right) \tag{3.3.2}$$

$$p\left(\mathbf{x},\ \mathbf{x}_0, t\right) = \frac{1}{4\pi}\frac{q(\mathbf{x}_0, t - |\mathbf{x}\text{-}\mathbf{x}_0|/c_0)}{|\mathbf{x}\text{-}\mathbf{x}_0|} \tag{3.3.3}$$

The formulation in the frequency domain, derived by the Fourier transform ($P(\mathbf{x}, \mathbf{x}_0, \omega) = \mathcal{F}(p(\mathbf{x}_0, t))$) is expressed in (3.3.4).

$$\begin{aligned} Z(\omega, \mathbf{x}_0) &= \frac{4\pi}{M}\sum_{m=1}^{M} |\mathbf{x} - \mathbf{x}_0| P(\mathbf{x}, \mathbf{x}_0, \omega) e^{i\omega\tau} \\ &= \frac{1}{N}\sum_{m=1}^{N} s(\mathbf{x}, \omega) P(\mathbf{x}, \mathbf{x}_0, \omega) \end{aligned} \tag{3.3.4}$$

Where $s(\mathbf{x}, \mathbf{x}_0, \omega)$ is the so called steering function (3.3.5),

$$s(\mathbf{x}, \mathbf{x}_0, \omega) = 4\pi|\mathbf{x} - \mathbf{x}_0| e^{i\omega\tau} \tag{3.3.5}$$

Considering an array with M microphones it is often given as the *steering vector* $g(\mathbf{x}, \omega)$ in (3.3.6).

$$g(\mathbf{x},\omega) = \begin{bmatrix} 4\pi|x_1 - x_0|e^{i\omega t_1} \\ 4\pi|x_2 - x_0|e^{i\omega t_2} \\ \vdots \\ 4\pi|x_M - x_0|e^{i\omega t_M} \end{bmatrix} \tag{3.3.6}$$

The microphone signals in the frequency domain can also be presented in vector format (3.3.7).

$$Y(\omega) = \begin{bmatrix} P_1(\omega) \\ P_2(\omega) \\ \vdots \\ P_M(\omega) \end{bmatrix} \tag{3.3.7}$$

The beamformer output $Z(\omega)$ can then be represented as (3.3.8). Here $(..)^\dagger$ refers to the Hermite form (transposed and complex conjugated). The power output of the signal can be calculated by squaring this absolute beamformer output, $L(\mathbf{x}) = |Z|^2$ given in (3.3.9).The CSM, expressing the correlation between two microphones is represented in this relation in the form of $CSM = Y(\omega)Y(\omega)^*$.

$$Z(\omega) = \frac{g(\mathbf{x},\omega)^\dagger Y(\omega)}{M} \tag{3.3.8}$$

$$\begin{aligned} L(\mathbf{x}) &= ZZ^* \\ &= (g^\dagger Y)(g^\dagger Y)^* \\ &= g^\dagger (YY^*)g \end{aligned} \tag{3.3.9}$$

Free stream velocity and grid position corrections

The beamforming formulation consider a stationary source, however in wind tunnel experiment, where the source is immersed in a moving flow, convection correction (Doppler effect) should be applied. Otherwise the beamforming would calculate the noise source shifted to the free-stream velocity. On the other hand, the power output of each search grid point should be dimension-less by the distance to the microphone to avoid calculate higher levels far from the actual noise source. A reference point should be established, in this study, the reference point was the center of the array of microphones.

The beamforming formulation used in this work follows the methodology proposed by Oerlemans [6]. The steering vector was calculated as shown in (3.3.10) and time delay was calculated as presented in (3.3.11), where $\beta^2 = 1 - M^2$ and $\mathbf{M}$ is the Mach number of free stream velocity expressed as a vector (only has a component in the free-stream velocity direction).

$$g = \frac{e^{-i\omega\tau}}{4\pi\sqrt{(\mathbf{M} \bullet (\mathbf{x}_m - \mathbf{x}_0))^2 + \beta^2|\mathbf{x}_m - \mathbf{x}_0|^2}} \tag{3.3.10}$$

$$\tau = \frac{1}{c_o\beta^2}(\mathbf{M} \bullet (\mathbf{x}_m - \mathbf{x}_0) + \sqrt{(\mathbf{M} \bullet (\mathbf{x}_m - \mathbf{x}_0))^2 + \beta^2|\mathbf{x}_m - \mathbf{x}_0|^2}) \tag{3.3.11}$$

For the beamforming code developed in this work, a 2D search grid along the span of the model was used, each direction was discretized in 50 points.

Source Power Integration

Source Power Integration (SPI) is used to quantify the total noise of a source in a defined region. Conventional beamforming gives the intensity of the noise at each search grid. To analyze the spectra and total noise for a specific area, a Region of Interest (ROI) is defined to calculate the corresponding total noise. Initially, this technique simulates a monopole of unit intentisty at the center of the ROI, known as a Point Spread Function (PSF). The PSF basically defines how a microphone array responds to a monopole placed in front of the array.

The relation for calculating the power with SPI is given in (3.3.12) and based on [40]. Here J is the total search grid points inside of the ROI, $w'_j = g/|g|^2$, g_k the steering vector at the location of the simulated source, and P_{sim} the intensity of the simulated monopole, assumed as a unit.

$$P = \sum_{j=1}^{i} \left(w'_j CSM w_j\right) \frac{P_{sim}}{\sum_{j=1}^{i} w'_j \left(g_k g'_k\right) w_j} \tag{3.3.12}$$

The defined ROI is given in Figure 52, the flow is coming from left to right. A region is selected around the trialling edge, where there is no interference with the wind tunnel walls, but the region is broad enough to take into account all the relevant noise levels given in the beamforming maps.

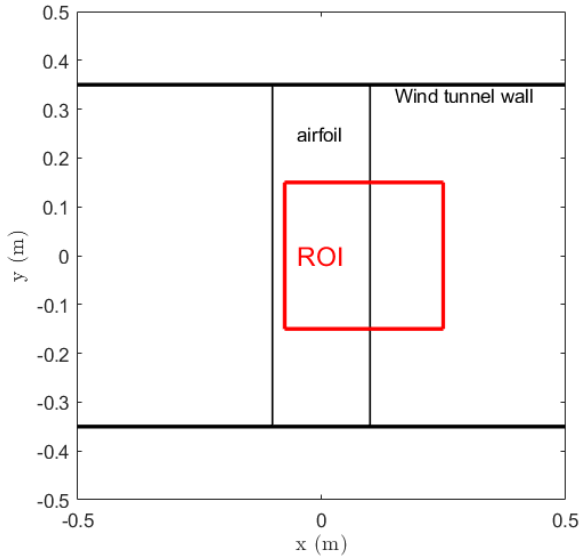

Figure 52: Region of Interest (x=[-0.075 0.25] and y=[-0.15 0.15]).

3.3.2 MATLAB Algorithm

An existing Matlab based algorithm is used to post process the raw microphone data. With this procedure the corresponding beamforming maps, and integrated sound pressure levels can be calculated. This algorithm consists out of the following eight steps:

1. **TDMS2MDATA.m**
   Converting a .TDMS (Technical Data Management Streaming) file, to .hdf5 (Hierarchical Data Format) file as input for the beamforming code. Most important, consisting the time series of all microphones.

2. **MDATA2CSM.m**
   Converting microphone time signals MDATA (.hdf5) into CSM format for the BEAMUT beamforming codes. For each test section the corresponding shear layer is taken into account in the final calculation of the Cross Spectral Matrix.

3. **Plot_Single_Mic_Spectra.m**
   Calculates the spectrum for an individual microphone. Spectra can be plotted against the frequency or Strouhal number.

4. **INPUTBEAMUT.m**
   Writes the required beamforming input parameters for the computational beamforming. Search grid point locations and microphone coordinates are defined here.

5. **RUN_CBF.m**
   A beamformer output map using the conventional beamforming method in the frequency domain. Different correction methods for the mean flow convection velocity can be used (Amiet and Sijtsma). Both methods showed similar results, Amiet is a more complex, time-consuming but accurate method and will be used for the OTS and HTS. The CTS uses Sijtsma because the z-coordinate of the shear layer location equals zero, Amiet can not be used in this Matlab file.

6. **PLOT_THIRD_OCT_BMAPS.m**
   Computes and plots the integrated noise maps from a given set of beamforming results.

7. **RUN_POW_INT.m**
   Writes the input parameters to calculate the integrated spectrum for a certain region of interest. Most important, the ROI must defined here.

8. **Plot_Integrated_Spectra.m**
   Plots the integrated third octave spectrum for the defined ROI.

PART III, RESULTS

4 Results

In this chapter, all the relevant results are given, explained and academically substantiated.

4.1 Background Noise

First, the acoustic effects of the noise reduction techniques are assessed. After that, a comparison of the background noise for the different test sections is set up.

4.2 Background Noise Reduction Techniques

The first experiments were related to the different noise reduction techniques, applied at the end of the CTS. After a discussion about the different noise reduction techniques, the quarter ellipse would be the most promising technique. The results are given as SPL of a single microphone in Figure 53a (mic15, in the middle of the band). In blue the initial background noise is shown, which is the reference for these first experiments. After installing the Quarter Ellipse and running the measurements, it was found that this Quarter Ellipse even slightly increased the noise. A strong airflow underneath and on top of the turntables outside of the wind tunnel was assessed, possibly generating noise. By human hearing, noise from the gap between the four turntables and the tunnel was assessed. Putting a seal on top of the turntables and making it airtight would be viable solution. After applying a seal, the SPL showed significant lower values so noise was reduced (Figure 53a). With this outcome, the additional noise reduction of the other techniques were assessed (serrations and Teddy-bear fabric). As Figure 53a shows, this did not resulted in a further decrease of the noise, doubting the origin of the noise source (the exit nozzle).

The gain in noise reduction for the Sealed Turntable in comparison to the initial situation, is given in Figure 53b. This shows a noise reduction up to 12 dB around 2000 Hz, for higher frequencies the noise is reduced between 4-6 dB. Regarding trailing edge noise at zero AoA, the frequency range lays between 1000-5000 Hz, so this background noise reduction will be beneficial for the beam-forming plots of the TE noise. The gap between the turntables will be sealed for all far field noise experiments.

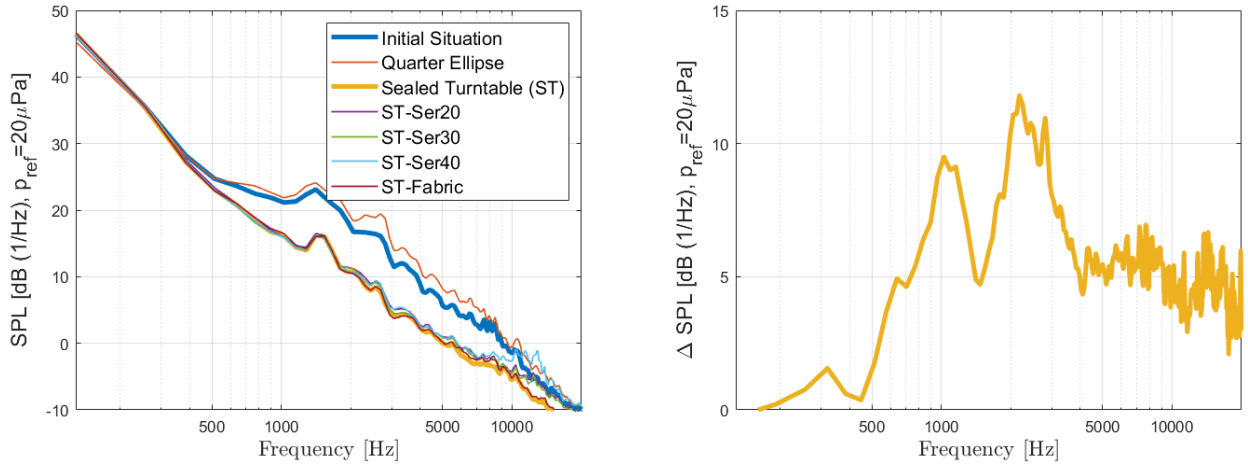

(a) Single microphone spectrum. **(b) Noise reduction of the Sealed Turntable.**

Figure 53: Measured background noise of a single microphone in the center of the array, normalized to a distance of 1 m from the wind tunnel centerline (OTS, U_∞ =30 m/s).

4.2.1 Calibration, Pressure Field to the Free Field

To compare the background noise of the different test sections, first of all a calibration for the CTS microphone array must be made. The Pressure Field (PF) must be related to the Free Field (FF), to compare with the other test sections. The microphone array for the OTS and HTS is positioned in the free field around 1.5m from the noise source, so acoustic reflection will not occur. The microphones for the CTS are located in the pressure field (0.45m from the noise source) resulting in higher levels due to pressure doubling. A so called house of foam is build in the CTS to avoid further reflection during this calibration. A speaker is emitting white noise measured by one single microphone in the array center (red circle, Figure 54a), measured for the free field and the pressure field.

1. Free Field, data acquired without the acrylic plate and microphone holder.
2. Pressure Field, data acquired with the acrylic plate and microphone holder.

In this way, the influence of the acrylic plate and microphone holder can be assessed for the CTS. Resulting in a better comparison of the different test sections. This results in two different SPL spectrum curves, the difference between these curves is subtracted and plotted in Figure 54b. This data is rather noisy, due to the fact that both situations are not, and can not be measured at the same time (like in other calibration methods). A 2^{nd} order polynomial fitted this data and is subtracted from the noise levels obtained during all the experiments in the CTS (calibration subtracted from all single microphone data). In this way, all test section are comparable.

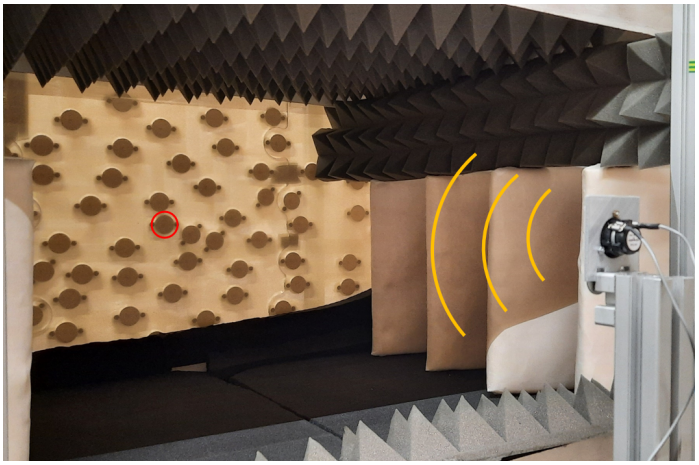

(a) Photo of the house of foam in the CTS (PF).

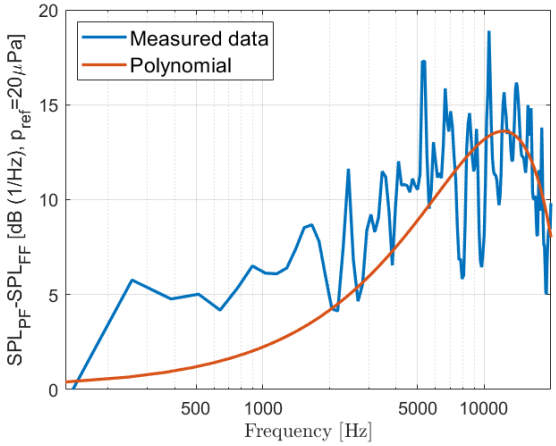

(b) SPL difference between the two configurations.

Figure 54: Calibration, pressure field to the free field.

4.2.2 Comparison of the Background Noise

Experiments measuring the background noise for each test section (without airfoil) are carried out. The background noise spectra for the OTS and HTS are similar (Figure 55a), whereas the CTS gives higher values. A high frequency hump (> 7000 Hz) is present at the HTS and CTS, possibly originating from the vibration of the Kevlar cloth and the gap between the Kevlar panels. The frequency resolution has been tweaked to avoid unwanted peaks in the spectrum (cf. Figure 53a). Regarding higher flow velocities, the background noise increases and the hump shifts to higher frequencies (Figure 55b). The difference in SPL compared to the OTS is similar for all velocities.

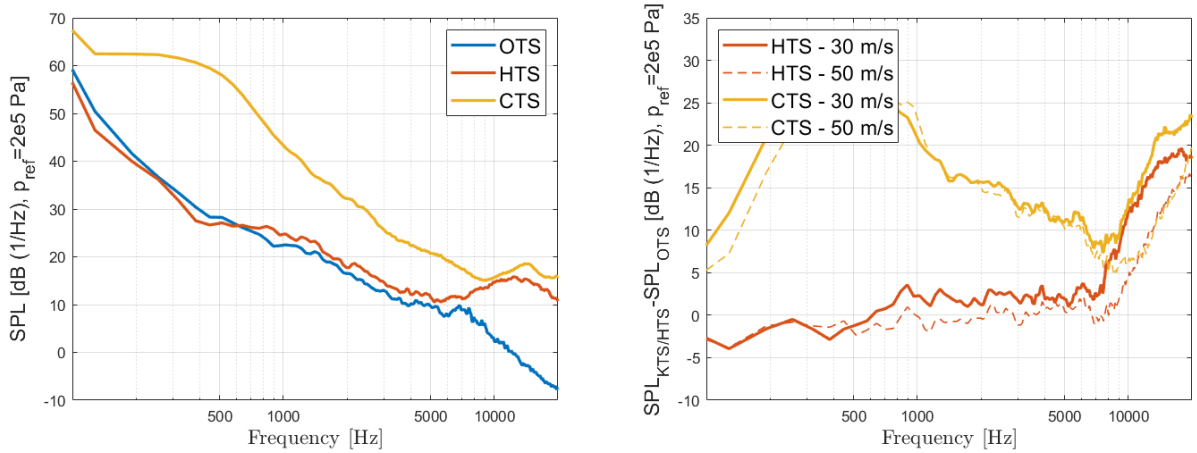

(a) SPL (U_∞ =30 m/s). **(b) Increased background noise compared to the OTS.**

Figure 55: Measured background noise of a single microphone in the center of the array, normalized to a distance of 1 m from the wind tunnel centerline.

With the beamforming technique, the location and amplitude of noise sources can be visualised/quantified. The beamforming maps of the HTS, shows two line sources at the intersection of the panels (Figure 56a). Noise is generated due to the unsteady surface and/or gap between the panels. For the open - and Kevlar test section, the microphone array is placed in the free field, an acoustic barrier is used to avoid noise coming from the collector and corner vanes of the wind tunnel contaminating the experiments. Regarding the CTS, the microphones are flush mounted in the conical microphone holders, allowing low frequency noise from the corner vanes to interfere with the experiments (Figure 56b). Both unwanted noise sources could contaminate the experiments.

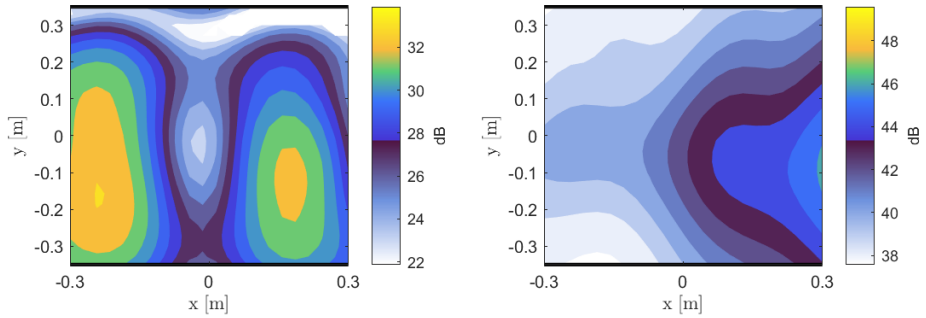

(a) HTS - 2500 Hz. **(b) CTS - 1000 Hz.**

Figure 56: One-third octave beamforming maps for the background noise, scaled to a reference distance of 1 m. (U_∞ =30 m/s).

4.3 Wall Pressure Microphones

4.3.1 Calibration Procedure

Calibration methods for the sensitivity and the frequency response for the microphone's are applied. A pistonphone is used during the calibration of the sensitivity, together with a tonal noise of 1 kHz. Values for each microphone are given in Table 3. The sensitivity of a microphone, the ratio of the output voltage to the input pressure $[mV/Pa]$, only affects the amplitude of the wall pressure spectrum.

Table 3: Sensitivity of the Surface Pressure Microphones.

Microphone	1	2	3	4	5	6
NACA0012	47.6	52.0	42.0	46.5	37.2	57.9
NACA0018	54.0	38.1	43.4	40.1	49.6	54.0
NACA63018	277.8	220.5	213.6	3457.85	-	-

Then the calibration device (Figure 57a) is used to determine the frequency response. A Visaton FR8 speaker is emitting white noise in the calibration device, the reference mic located at the calibrator (a GRAS microphone) and the Knowles/Invensense wall pressure microphones can be compared. A transfer function can be calculated to eliminate the difference in frequency response due to the pinhole in the airfoil. These two calibration methods must be used in the post processing algorithm. In this way, the wall pressure microphones in the airfoil can be compared. Differences regarding the sensitivity and frequency response of a certain microphones are eliminated.

It must be checked if the microphones are not saturated, for the Knowles microphones they saturate above $U_\infty = 25\ m/s$. Microphones are saturated when the histogram of the data doesn't resemble a Gaussian distribution (see Figure 57b). For 30 m/s these humps in the curves (at the begin and end) shows that the microphones are saturated. The Invensense microphones in the TE of the NACA63018 saturate at a higher velocity, allowing sound pressure measurements up to U_∞ =50 m/s.

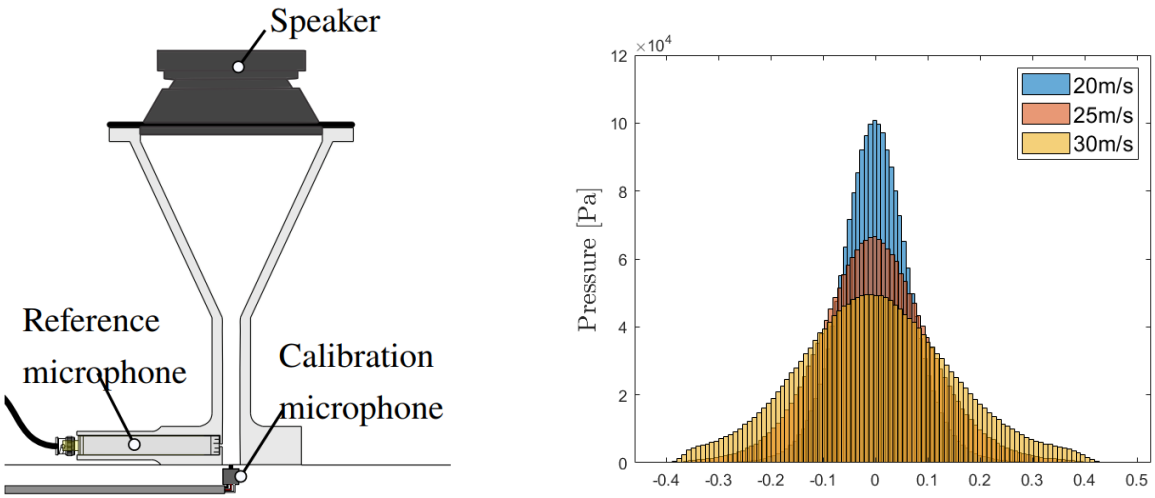

(a) Calibration Device [22]. **(b) Histogram of the data of mic1, NACA0012.**

Figure 57: Calibration, wall pressure microphones.

4.3.2 Comparison of the Test Sections

Although, the measured data of the calibration of the wall pressure microphones shows a large peak at frequencies higher than a 1000Hz (see Figure 58a). It is assumed that the frequency response of the Knowles microphones is flat, this is also given by the Knowles supplier [41]. A flat transfer function is applied to the data to correct for the influence of the pinhole.

Data in Figure 58b shows the wall pressure spectrum (Φ_p/p^2_{ref}) for all three test sections. This data collapses almost exactly for all sections, which is a good first indication that the trailing edge noise radiated by the airfoil is similar. Wall pressure spectra can be used to calculate the power spectral density of the far field based on Amiet's theory (2.7.9). The span-wise and stream-wise coherence between microphone pairs are given in Figure 58c and 58d respectively. This again shows that the coherence for the wall pressure spectrum for the different test sections is similar. The coherence can be used to calculate the correlation length (l_y and l_x) given in (2.7.10), also used in Amiet's theory. Similar wall pressure characteristics are assessed for the NACA0012, giving a good first indication that the far field noise coming from the trailing edge of the airfoil is similar in all test sections. Identical results are obtained for the other airfoils, but not shown in these graphs for simplicity. So these graphs suggest that similar values for the far field noise should be obtained. Otherwise, differences would be related to the test section itself (influence of the test section). In the next section, the far field noise for the different test sections is compared.

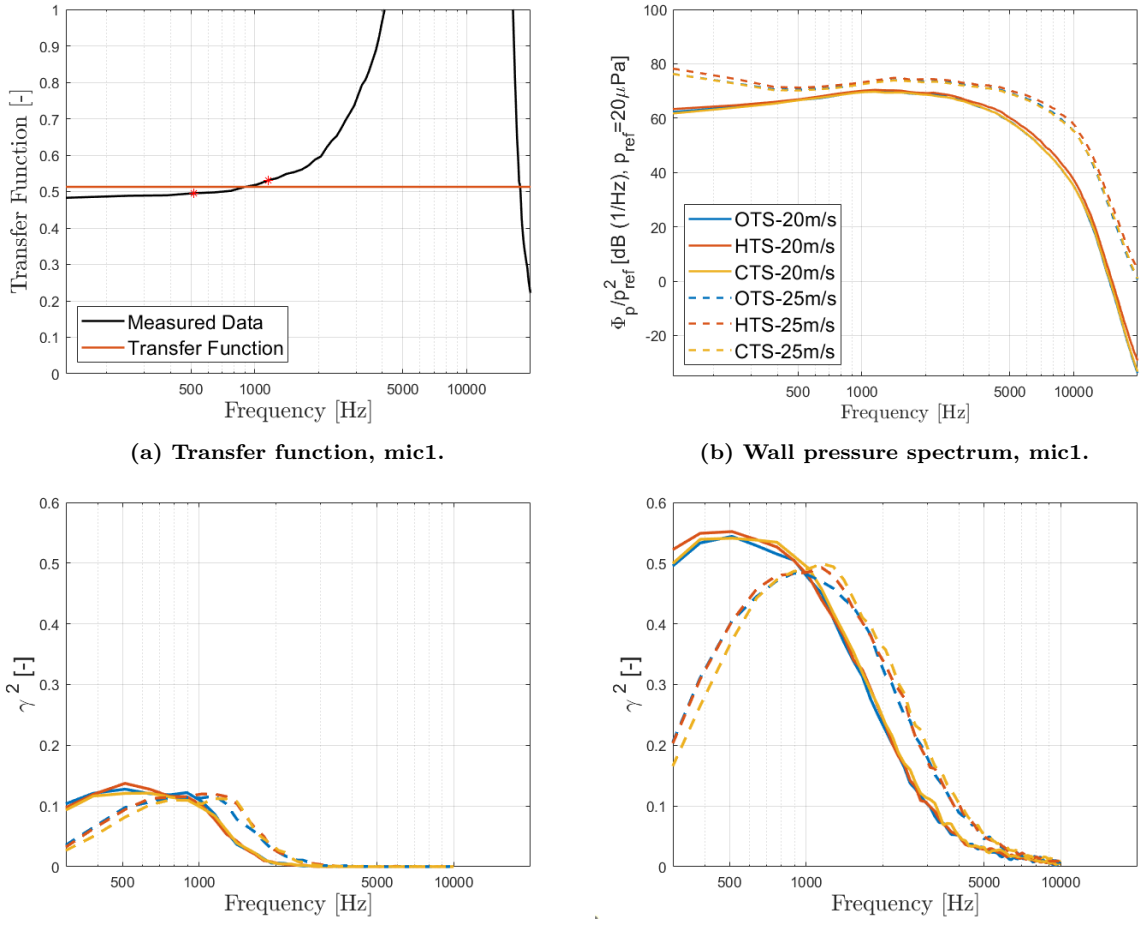

(a) Transfer function, mic1.

(b) Wall pressure spectrum, mic1.

(c) Span-wise coherence, mic1-mic2.

(d) Stream-wise coherence, mic1-mic4.

Figure 58: Wall pressure characteristics for the NACA0012 (AoA=0°).

4.4 Far Field Noise

4.4.1 Test Section Comparison

The beamforming maps for the NACA0012, with a straight trailing edge, for all test sections, are given in Figure 59. The flow is coming from left to right, and the airfoil geometry and wind tunnel walls are plotted in the beamforming maps. For all cases the trailing edges noise is dominating, resulting in a line sources around the TE. Trailing edge noise dominates the spectrum for frequencies around 1000-5000 Hz, so three frequencies are chosen for the beamforming maps (1500, 2500 and 4000 Hz).

The dB levels for the OTS and HTS are similar, the CTS gives slightly lower values. The correction regarding the calibration of the Pressure Field to the Free Field (CTS) is taken into account. The shape of the line source for the OTS and HTS are similar, this because the same microphone array and distance to the airfoil is used. The CTS gives a smaller line source, possibly because of a shorter distance to the noise source and a wider array, resulting in better localization of the noise source.

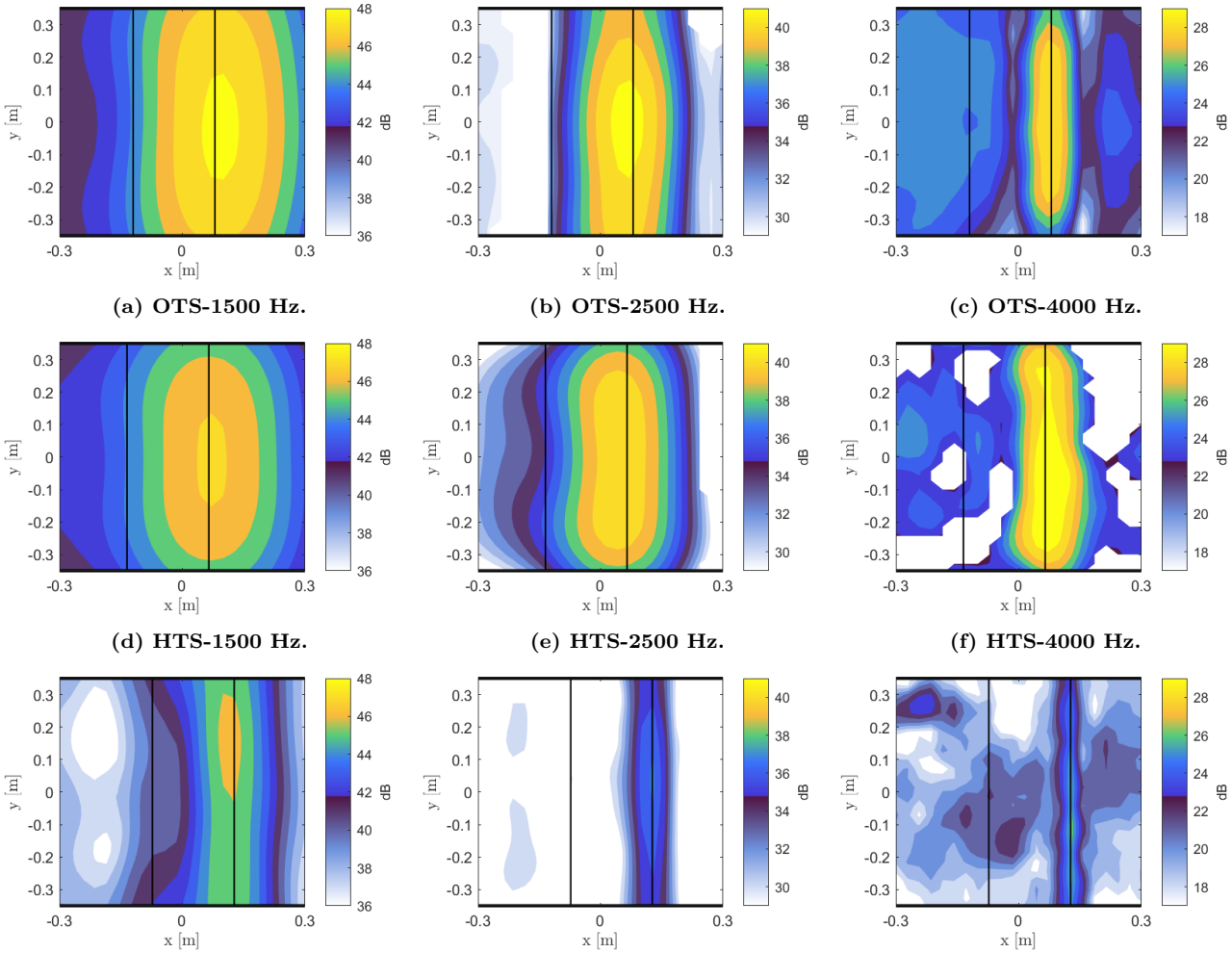

(a) OTS-1500 Hz. (b) OTS-2500 Hz. (c) OTS-4000 Hz.

(d) HTS-1500 Hz. (e) HTS-2500 Hz. (f) HTS-4000 Hz.

(g) CTS-1500 Hz. (h) CTS-2500 Hz. (i) CTS-4000 Hz.

Figure 59: One-third octave beamforming maps for the NACA0012-StrTE, scaled to a reference distance of 1 m (AoA=0°, U_∞=30 m/s).

Regarding the SPL after source power integration, the results are given in Figure 60. The defined region of interest is given in Figure 52, x= [-0.075 0.25] and y=[-0.15 0.15]. This ROI is chosen so that all relevant amplitudes of the TE line source are taken into account, but influences of the wind tunnel walls are circumvented. The Strouhal number is calculated by $St = (f\delta^*)/U_\infty$ (with δ^* from XFOIL). The difference in background noise for the test sections is still visible after integration. Up to a 1200 Hz and St=0.07, all test sections give similar values. The OTS and HTS overlaps even up to a 8000Hz and St=0.45. The CTS gives lower values than the other two test sections when f>1200 Hz and St>0.07.

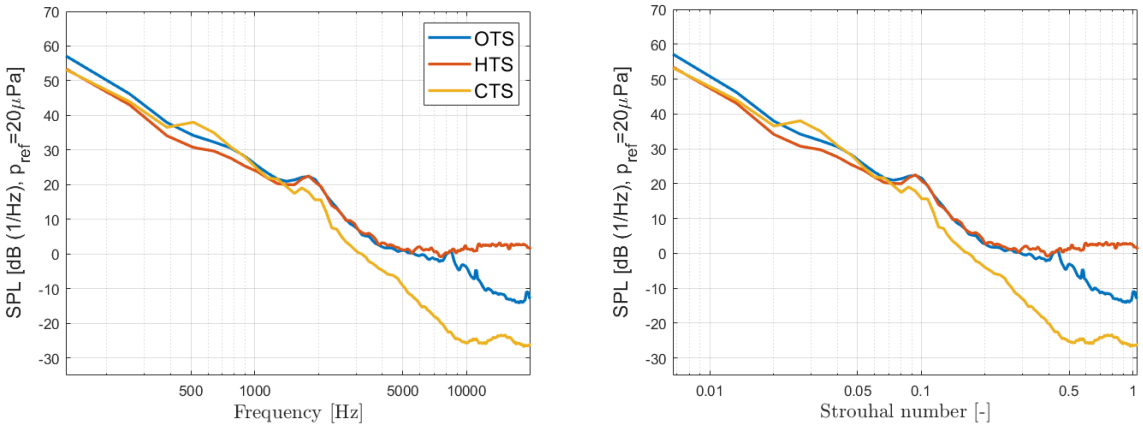

(a) Frequency plot. **(b) Strouhal plot.**

Figure 60: Integrated noise levels in one-third octave bands for the NACA0012, StrTE scaled to a reference distance of 1 m (AoA=0°, U∞=30 m/s).

For all test sections the beamforming maps show interaction with the wind tunnel walls (at the airfoil location) at low frequency, especially at higher velocities or serrated airfoils (Figure 61). To avoid this phenomena in the post processing, a relatively small ROI can be specified. In this way the noise coming from the wind tunnel walls will not be taken into account during the power integration.

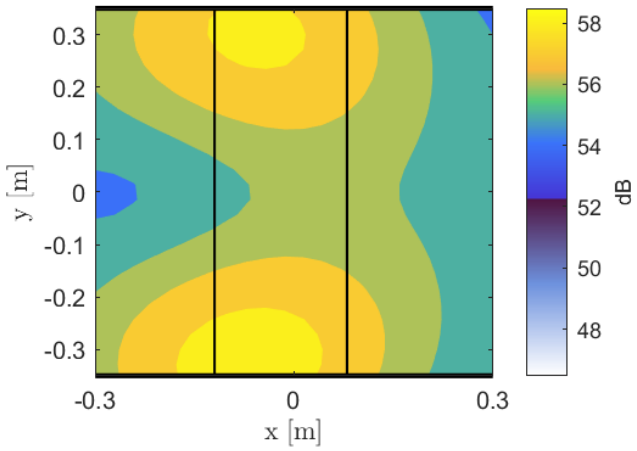

Figure 61: One-third octave beamforming map OTS-NACA0012-StrTE, 1500 Hz, scaled to a reference distance of 1 m (AoA=0°, U∞=50 m/s).

4.4.2 The influence of Serrations

The influence of serrations on TE noise is given in Figure 62, the beamforming maps for the OTS are given (AoA=0°, U_∞=30 m/s). For the given frequencies, it shows a noise reduction between 4-10 dB. Values for the two different serrations are similar. As discussed before, the deviating shapes in the Figures 62d and 62g originate from interaction with the wind tunnel walls. For the Straight TE this principle is almost not present, due to the higher values of the TE noise dominating the plot.

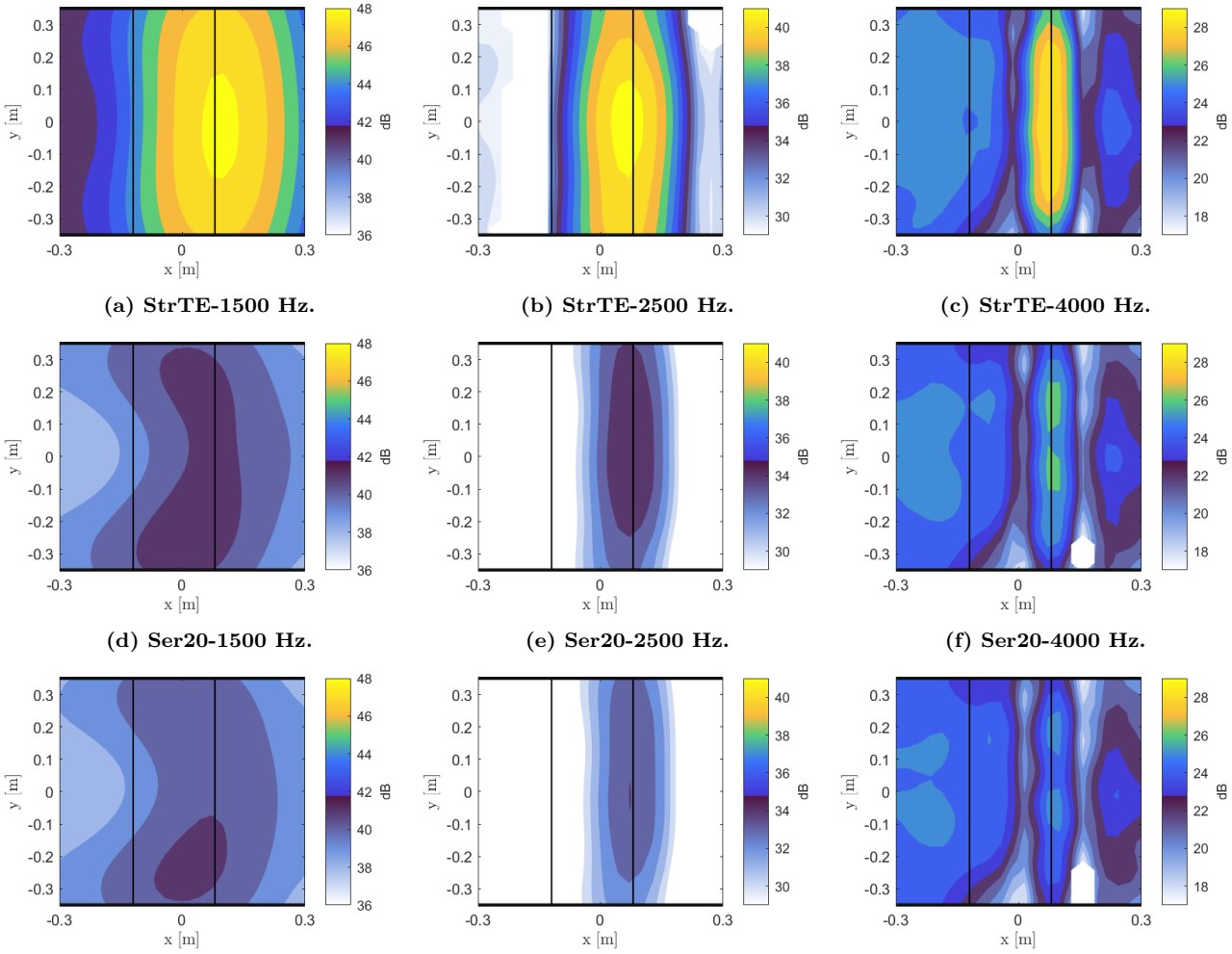

(a) StrTE-1500 Hz. (b) StrTE-2500 Hz. (c) StrTE-4000 Hz.

(d) Ser20-1500 Hz. (e) Ser20-2500 Hz. (f) Ser20-4000 Hz.

(g) Ser40-1500 Hz. (h) Ser40-2500Hz. (i) Ser40-4000 Hz.

Figure 62: One-third octave beamforming maps for the OTS-NACA0012, scaled to a reference distance of 1 m (AoA=0°, U_∞=30 m/s).

More important is the test section comparison of the serrated airfoils. After power integration, this results in the SPL given in Figure 63. This shows, that both serration reduce the TE noise at similar frequencies and with similar noise reduction levels. Noise is being reduced between 500-5000 Hz for a free stream velocity of 30 m/s. The background noise in the plots refer to the noise after power integration in the specified ROI. Rather similar spectra are given for the OTS and HTS, the CTS deviates clearly.

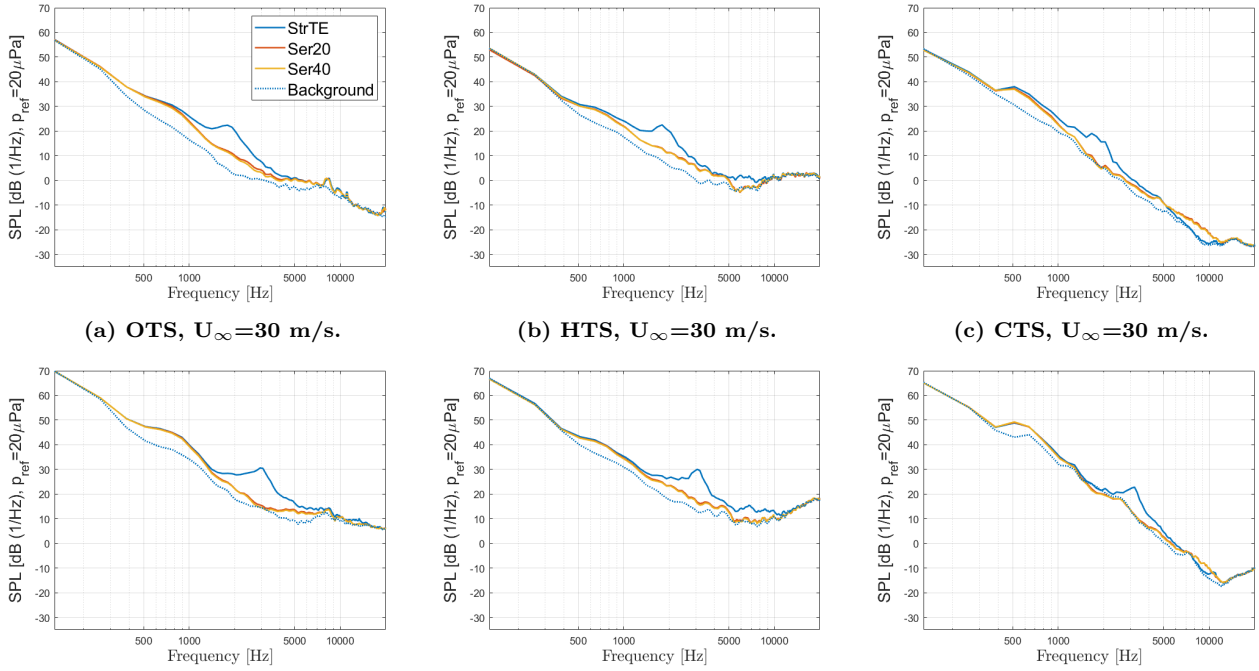

(a) OTS, U_∞=30 m/s. **(b) HTS, U_∞=30 m/s.** **(c) CTS, U_∞=30 m/s.**

(d) OTS, U_∞=50 m/s. **(e) HTS, U_∞=50 m/s.** **(f) CTS, U_∞=50 m/s.**

Figure 63: Integrated noise levels in one-third octave bands for the NACA0012, scaled to a reference distance of 1 m (AoA=0°).

The gain in noise reduction is given in Figure 64. Regarding 30 m/s, a maximum noise reduction of 11.5 dB is obtained for the OTS. All test sections show similar peaks around 2000 Hz for the two serrations, 9.5-11.5dB. So despite the deviations in background noise, the noise reduction of the serrations on the NACA0012 at 30 m/s is similar in all test sections. At 50 m/s the noise reduction is assessed between 11-16 dB. Both serrations show quite similar results, the Ser40 shows a slightly higher noise reduction in each test section. In comparison to 30 m/s, at 50 m/s noise is reduced at slightly higher frequencies. The origin of the deviations of the ΔSPL between the different test sections is the background noise. The HTS shows a slightly noisier spectrum in comparison to the OTS, where the curves are smooth (f<3000 Hz). It must be noted, that for the CTS the background noise gives similar values as the serrated airfoil at some frequencies. Indicating that the background noise is higher than the noise coming from the CTS-NACA0012-Ser, resulting in a lower noise reduction at higher flow velocities. Regarding U_∞=20 m/s a maximum noise reduction of 8 dB is measured, ΔSPL for the test sections overlaps nicely. For 40 m/s the noise reduction by serration shows already ready differences between the test sections.

Regarding the beamforming maps of the CTS, line sources will be visible at less frequencies, especially at higher velocities. Resulting in a power integration over a region without TE noise, eventually leading to different ΔSPL at those frequencies. The range of frequencies where the line source for TE is visible, is given in Table 4. Beamforming maps where TE noise is barely/not visible are given in Figure 65.

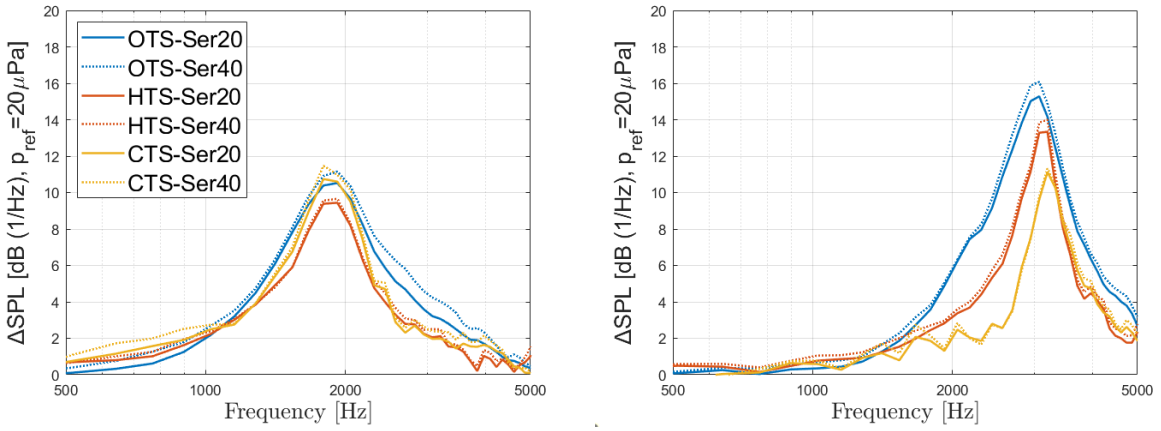

(a) U_∞=30 m/s. (b) U_∞=50 m/s.

Figure 64: Integrated noise reduction levels of the trailing-edge serrations in one-third octave bands, NACA0012 (AoA=0°).

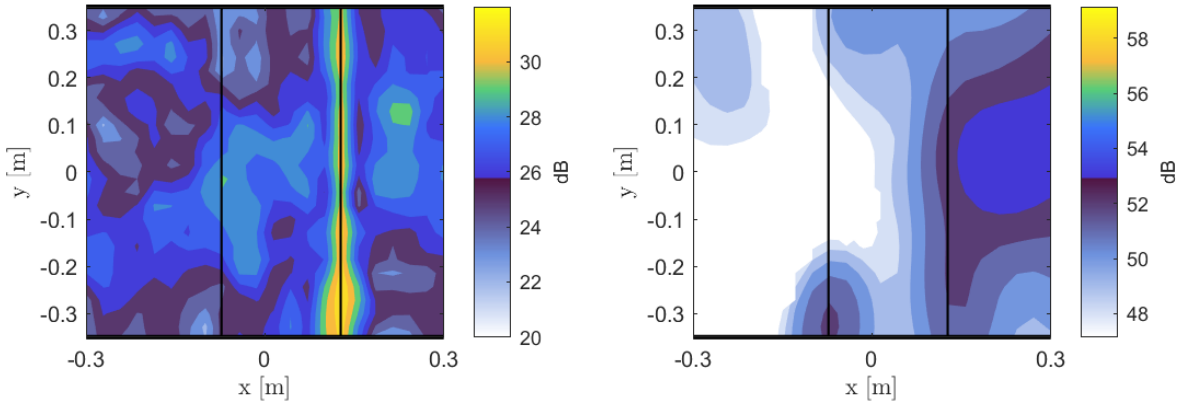

(a) U_∞=40 m/s, 4000 Hz. (b) U_∞=50 m/s., 4000 Hz.

Figure 65: One-third octave beamforming maps for the CTS-NACA0012-Ser20, scaled to a reference distance of 1 m (AoA=0°).

Table 4: Visible TE line sources in the one-third octave beamforming maps, NACA0012 (values in kHz).

	OTS			*HTS*			*CTS*		
	StrTE	**Ser20**	**Ser40**	**StrTE**	**Ser20**	**Ser40**	**StrTE**	**Ser20**	**Ser40**
20 m/s	0.5-3	0.5-3	0.5-3	0.5-3	0.5-3	0.5-3	1-2	1-2	1-2
30 m/s	0.5-6	0.5-6	0.5-6	0.5-4	0.5-5	0.5-5	1-3	(4)	(4)
40 m/s	0.5-6	0.5-6	0.5-6	0.5-5	0.5-5	0.5-5	1-4	(4)	(4)
50 m/s	0.5-6	0.5-6	0.5-6	0.5-5	0.5-5	0.5-5	2-4	X	X

4.5 Mach Scaling

Scaling by Mach in acoustics is often done to show the origin of a certain SPL spectrum (for a certain frequency range), relating it to certain aerodynamic mechanism. Figure 66 shows Mach scaling of the TE noise versus the Strouhal number, representing a frequency range from 500-5000 Hz. This can also be helpful in the prediction of trailing edge noise.

The spectrum shape at 20 m/s is deviating from the rest, this is due to the lower levels of the noise, increasing the presence of the background noise in the SPL. Hereby the TE noise at 20 m/s (OTS) is only visible up to 3000 Hz, while for the other velocities the beamforming maps shows line sources up to 6000 Hz. The fifth power law scaling behavior is associated with sources in the boundary layer, so also used for airfoil noise scaling. Brooks [12] found a power law scaling between fifth and sixth order for the airfoil noise. Tripping devices were used, and turbulent boundary layer structures where developed on both sides of the airfoil. Regarding laminar boundary layer vortex shedding noise, this power law scaling can not be used. The graph shows a good scaling with the 4th power for the OTS and HTS, even with the 3d power for the HTS. Furthermore no conclusions can be made.

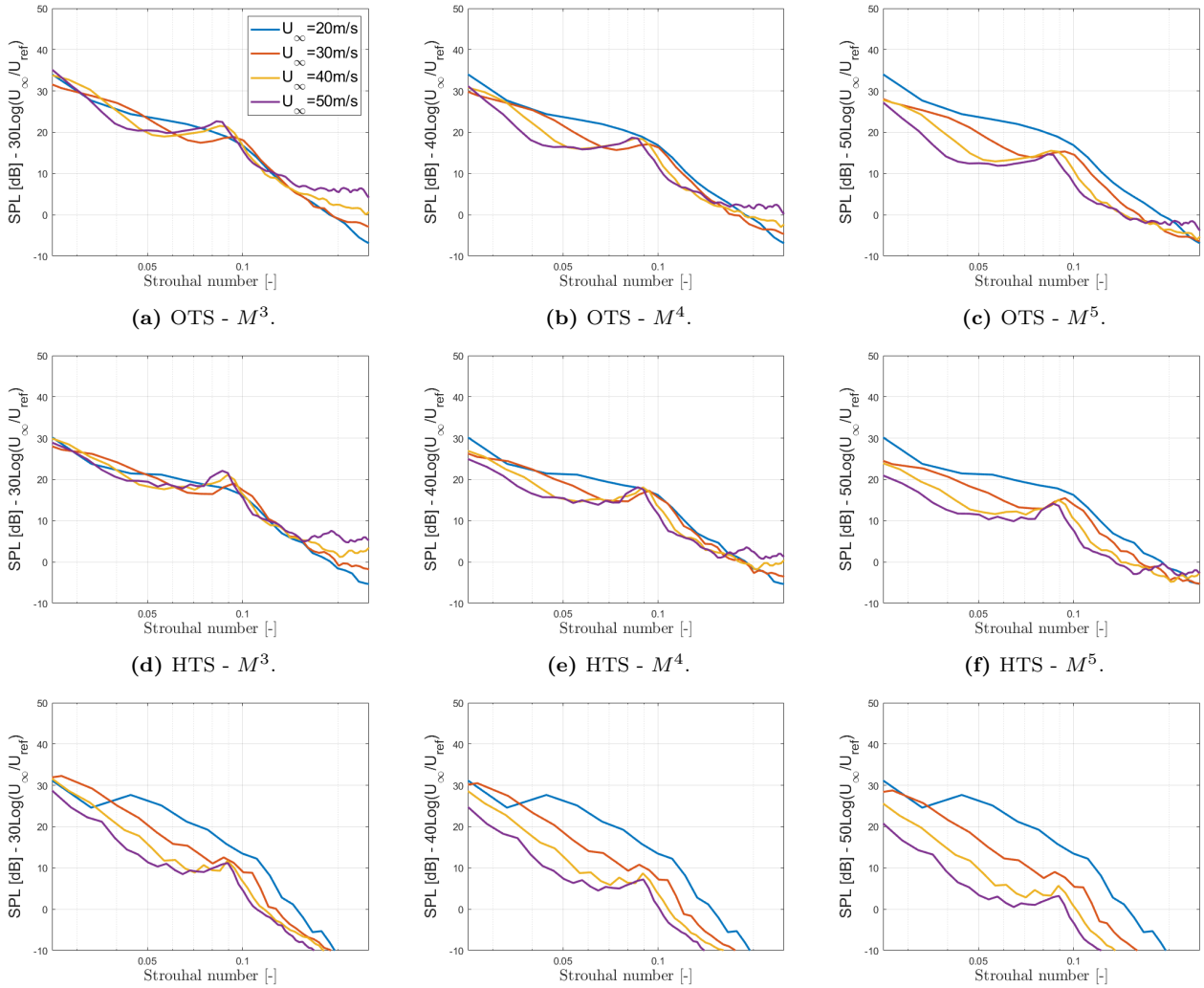

(a) OTS - M^3. **(b)** OTS - M^4. **(c)** OTS - M^5.

(d) HTS - M^3. **(e)** HTS - M^4. **(f)** HTS - M^5.

(g) CTS - M^3. **(h)** CTS - M^4. **(i)** CTS - M^5.

Figure 66: Mach number scaling with the NACA0012 Trailing Edge Noise.

4.6 Airfoil Comparison

A comparison of the three airfoils is given in this section. The far field spectrum data is given in Figure 67. Here the integrated levels shows a maximum of 18.7 dB above the measured background noise, produced by the NACA0012. The spectrum for the NACA0018 and NACA63018 (similar thickness) overlaps up to 2000 Hz, at higher frequencies the NACA63018 produces more noise. Regarding noise reduction by serration, the loudest airfoil also shows the highest noise reduction (10.5dB). This airfoil shows a steep peak around 2000 Hz, while the other two other airfoils show a slightly broader noise reduction. Noise is reduced up to 7300 Hz for the NACA63018, this airfoil also shows more high frequency noise in the far field spectrum in comparison to the other two airfoils. A maximum noise reduction of 6.8 dB and 7.8 dB for the NACA0018 and NACA63018 respectively is assessed.

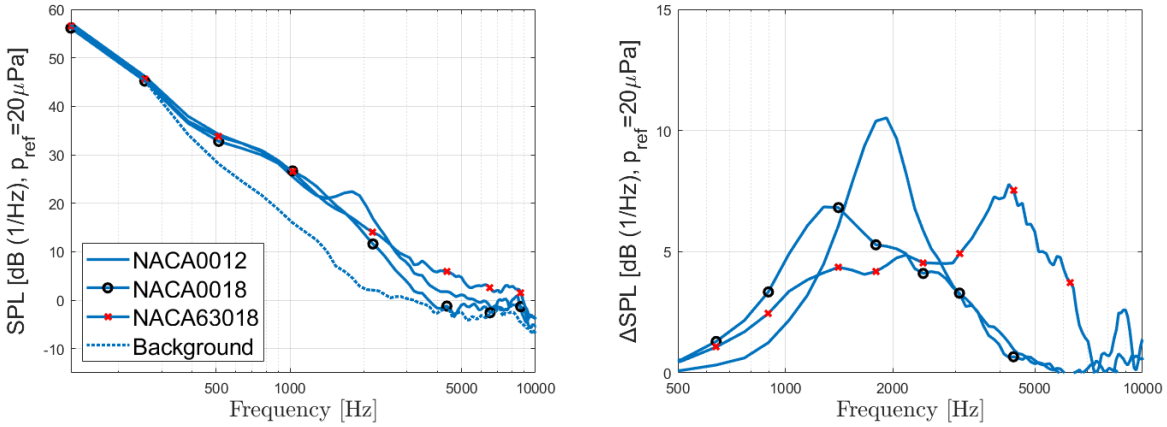

(a) Integrated noise spectrum - StrTE. **(b) Integrated noise reduction levels by Serration.**

Figure 67: Airfoil comparison of the far field noise (OTS, AoA=0° and U_∞=30 m/s).

The wall spectrum for the the different airfoils is given in Figure 68, transfer functions for the frequency response are applied. It must be noted that different microphones are being used in the TE of the airfoils, and the chordwise location is different (NACA0012 and NACA0018: x/c=0.93, NACA63018: x/c=0.86). The amplitude of Φ_p/p^2_{ref} can not be compared, it can be concluded that there is a different development of the boundary layer over each airfoil, resulting in three different wall pressure spectra.

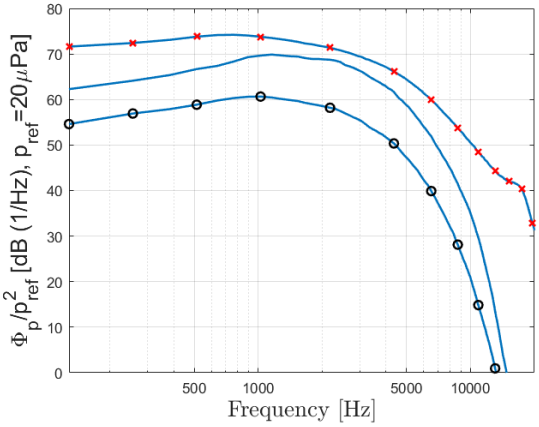

Figure 68: Comparison of the wall pressure spectrum (OTS, AoA=0° and U_∞=20 m/s).

4.7 Non-zero Angles of Attack, NACA63018

4.7.1 Matching the Aerodynamics

Each test section has its own shear layer, for the OTS this results in a diverged flow leading to lower pressure levels acquired by the pressure ports for non-zero AoA (shear layers are given in Figure 42). Due to this issue the *effective Angle of Attack* (AoA_{eff}) determined by the lift forces, and the *geometric Angle of Attack* (AoA_{geo}) set in the wind tunnel, must be matched. In this way the same aerodynamic conditions are used in each test section and a comparison can be made. With the pressure tabs the measured C_p can be matched with XFOIL, relating the effective - with the geometric AoA.

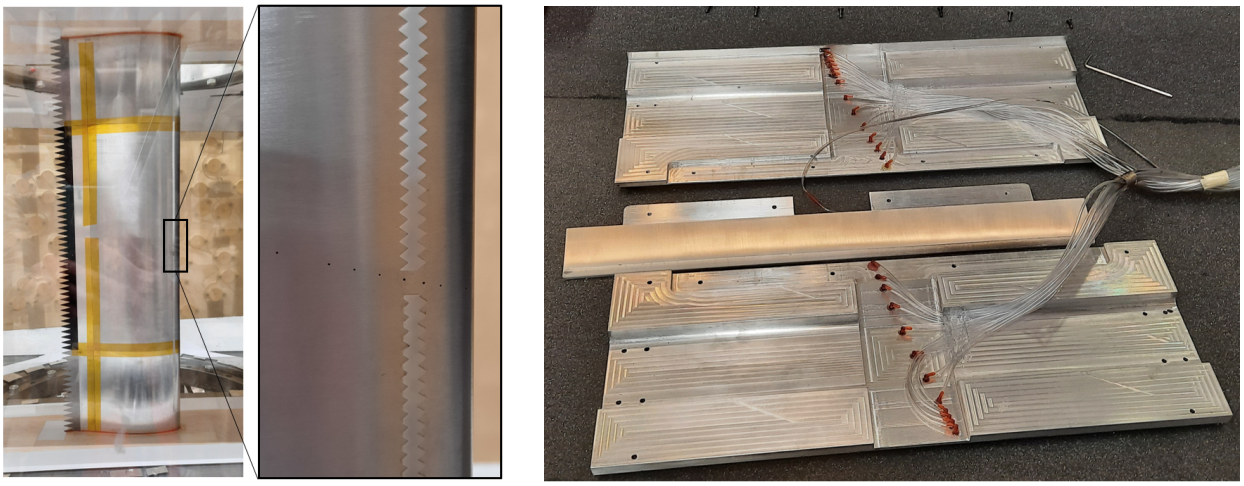

(a) The installed serrated NACA63018 (CTS), detailed view of the pressure ports and tripping device near the leading edge.

(b) Inside of the hollow airfoil with in the middle the straight trailing edge. Pressure port holes are connected via pressure tubes to a pressure box to acquire the data.

Figure 69: Photo's of the NACA63018.

In Figure 70 the experimental C_p data for the NACA63018 is compared to XFOIL. This shows that the acquired data from XFOIL (AoA_{eff}=4 °) is represented by a geometric angle of attack of 5°. Data for all test section is given in Table 5. This shows that the geometric AoA for the OTS deviates the most from the effective AoA, the other two test sections have smaller deviations. The CTS has the best aerodynamic free-flight conditions. The difference between the HTS and CTS could originate from the fact that the Kevlar cloth is not complete airtight, reducing the flow rate.

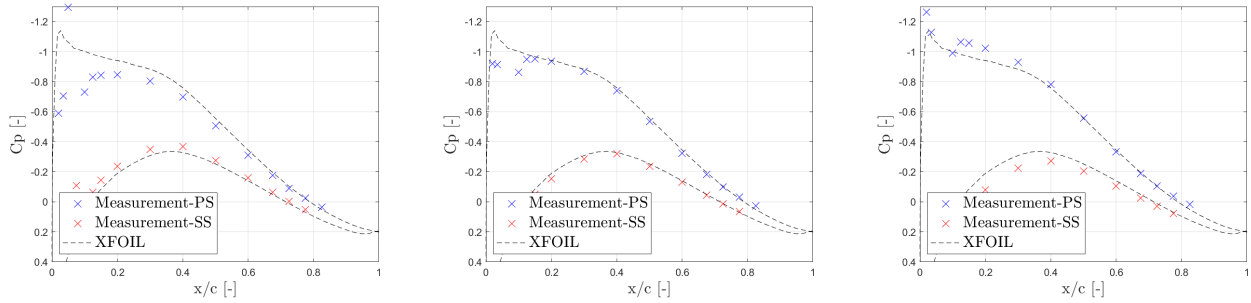

(a) AoA_{geo}=4°. **(b) AoA_{geo}=5°.** **(c) AoA_{geo}=6°.**

Figure 70: NACA63018 C_p data, HTS.

Table 5: Geometric Angle of Attack for all test sections.

Effective AoA [°]	**0.0**	**4.0**	**8.0**	**-4.0**	**-8.0**
Geometric AoA, OTS [°]	0.0	6.5	12.0	-6.5	-12.0
Geometric AoA, HTS [°]	0.0	5.0	9.5	-5.0	-9.5
Geometric AoA, CTS [°]	0.0	4.5	9.0	-4.5	-9.0

A rotation of the turntable in clockwise direction (looking from the top) is defined to by positive angle of attack. This is shown in Figure 71. So the NACA63018 is positioned at an AoA_{geo}=9.5°, representing AoA_{eff}=8°. The air is flowing towards LE of the airfoil, so in this configuration the suction side is shown, the lift force will be in the direction of the Kevlar cloth on the right, perpendicular to the free stream. A negative AoA will represented by a rotation in counter clockwise direction, resulting in a lift force in opposite direction.

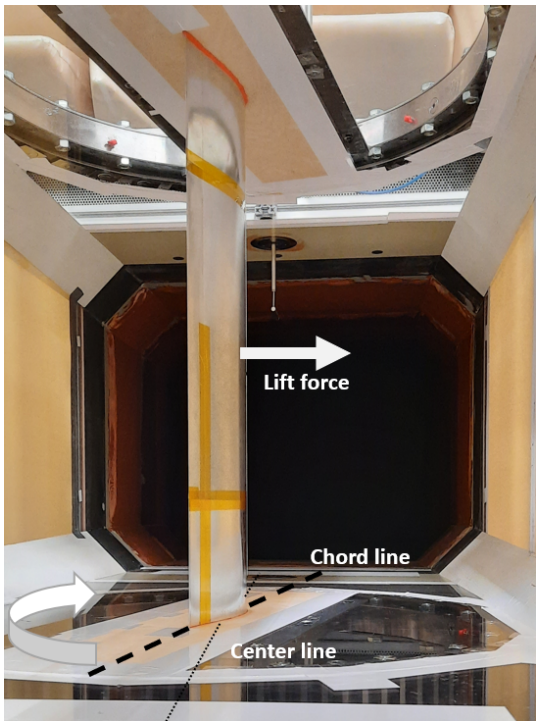

Figure 71: Photo of the NACA63018 at a non-zero AoA in the HTS.

4.7.2 Wall Pressure Microphones

The wall spectrum of the NACA63018 at non-zero Angles of Attack shows some interesting results. In general the spectrum overlaps nicely for all AoA, at all velocities (Figure 72). Only for the positive AoA at 20 m/s there are some small differences in the spectrum for each test section. Here the surface pressure is measured for the pressure side, so no separation would be expected near the trailing edge. A tripping device is used on both sides, so these differences could also not originate from transitional regions. Deviations between the test sections due to the hysteresis effect would also be likely to be visible on both sides.

The different geometric AoA for each test section could lead to a different development of the boundary layer, resulting in different values for the wall spectrum and/or far field noise. The graphs shows slightly higher values for the OTS, here the difference between the geometric and effective angle of attack is also the highest (AoA_{geo}=6.5° and AoA_{geo}=12°). If this is true, one would expect to see this phenomena on both sides of the airfoil. Although it could be true that development of the boundary layer on the pressure side is affected in a higher rate than on the suction side. Increasing the velocity could reduce this phenomena.

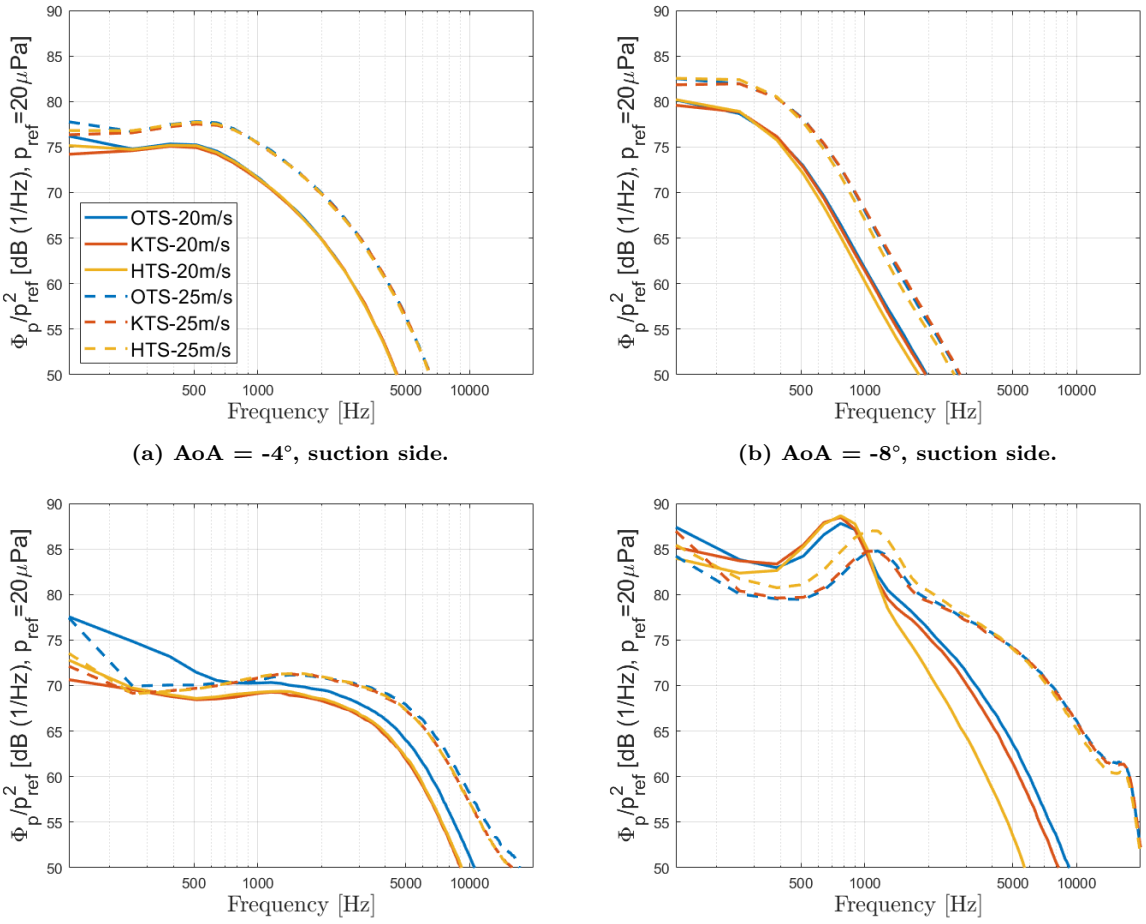

(a) AoA = -4°, suction side.

(b) AoA = -8°, suction side.

(c) AoA = 4°, pressure side.

(d) AoA = 8°, pressure side.

Figure 72: Wall spectrum for the NACA63018 at non-zero Angles of Attack.

4.7.3 Comparing the acoustic Far Field

In all test sections the straight trailing edge gives clear third-octave beamforming maps for $AoA = 4°$. Line sources are visible up to 6000 Hz (Fig. 73 and 75). Regarding the serrated airfoil, the same phenomena occur as discussed in previous sections. The interaction of the wind tunnel walls with the airfoil is increasing, resulting in noise sources in the beamforming plots especially for an AoA of 8° . This will not influence the integrated noise levels because of the chosen ROI.

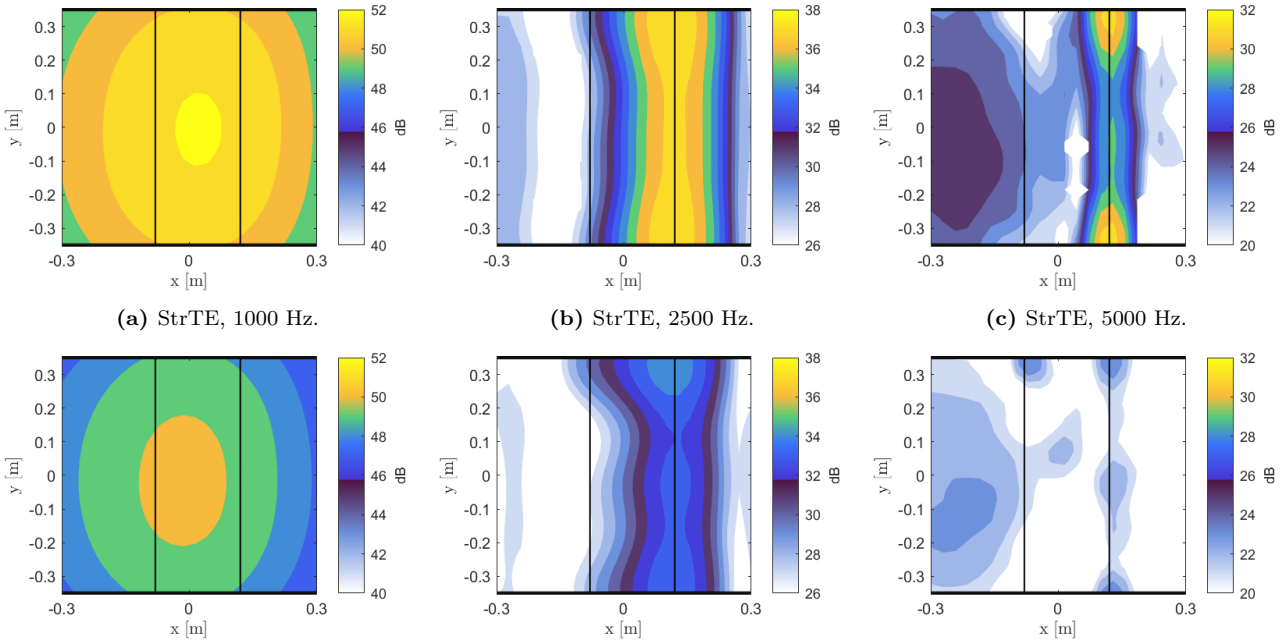

(a) StrTE, 1000 Hz. **(b)** StrTE, 2500 Hz. **(c)** StrTE, 5000 Hz.

(d) Ser, 1000 Hz. **(e)** Ser, 2500 Hz. **(f)** Ser, 5000 Hz.

Figure 73: One-third octave beamforming maps for the NACA63018, scaled to a reference distance of 1 m (OTS, AoA=4° and U_∞=30 m/s).

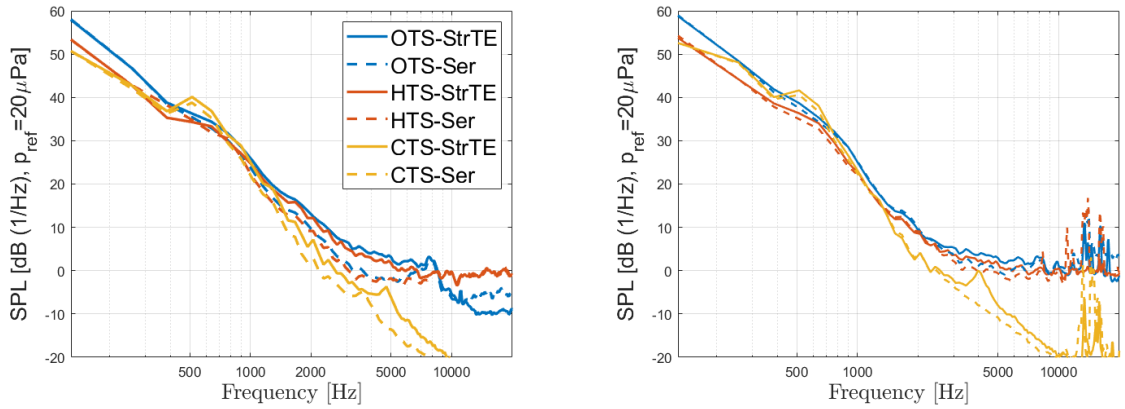

(a) AoA=4°. **(b) AoA=8°.**

Figure 74: Integrated noise levels in one-third octave bands for the NACA63018, scaled to a reference distance of 1 m (U_∞=30 m/s).

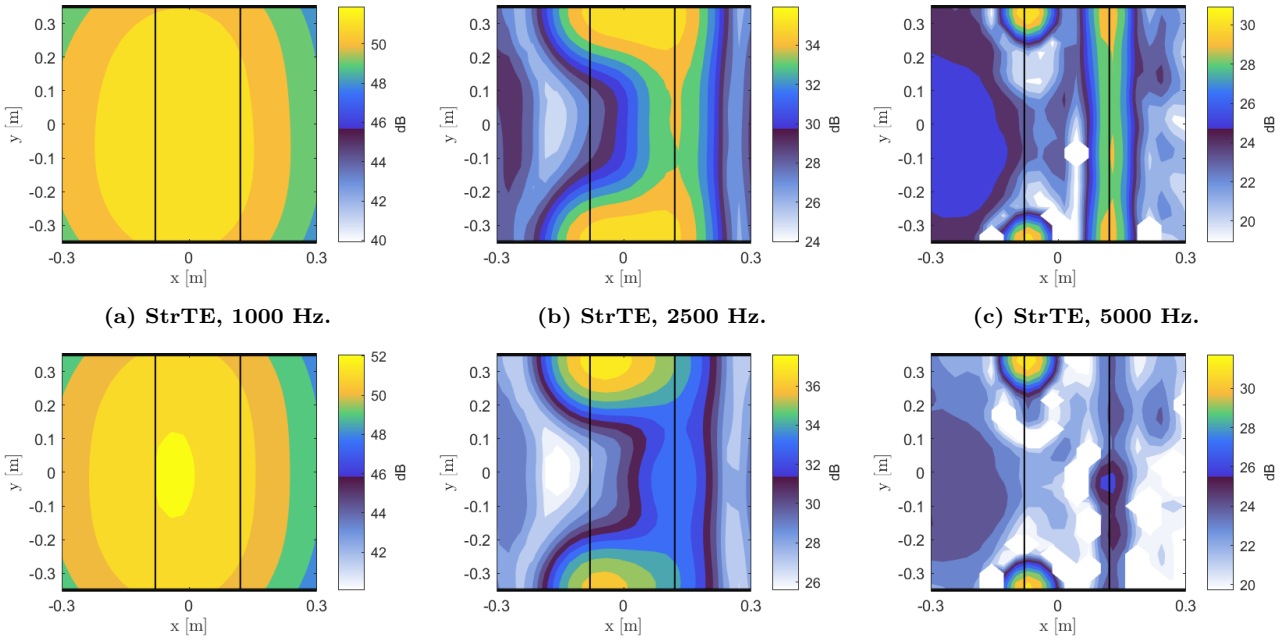

(a) StrTE, 1000 Hz. **(b) StrTE, 2500 Hz.** **(c) StrTE, 5000 Hz.**

(d) Ser, 1000 Hz. **(e) Ser, 2500 Hz.** **(f) Ser, 5000 Hz.**

Figure 75: One-third octave beamforming maps for the NACA63018, scaled to a reference distance of 1 m (OTS, AoA=8° and U_∞=30 m/s).

Table 6: Visible TE line sources in the beamforming maps for the NACA63018 (values in kHz).

AoA=4°

	StrTE-30	StrTE-50	Ser-30	Ser-50
OTS	1-6	1-6	1-3	1-5
HTS	1-6	1-6	(1-2)	(4)
CTS	1-4	1-4	(1-2)	X

AoA=8°

StrTE-30	StrTE-50	Ser-30	Ser-50
1-5	(4-5)	1-4	(4-5)
1-5	(4-5)	1-4	(3-4)
(2-3)	X	1-4	X

The integrated noise levels for lower frequencies (Figure 74), are not smooth like the spectrum for the NACA0012 given in Figure 60. The OTS gives a rather smooth curve, this is due to the visible Trailing Edge noise in the beamforming maps. The frequencies where a line source is visible at the TE is given in Table 6. For the serration with an AoA=4°, the beamforming plots only show TE noise for a small range of frequencies. At higher AoA the frequencies with visible line sources reduce even further, resulting in a power integration partially over the background noise influencing the spectrum. It can be concluded from this table that for the CTS this experiment can not define the TE noise for non-zero AoA properly for the relevant frequencies.

Noise reduction by serration for the NACA63018 at non-zero AoA is given in Figure 76. The data for the OTS and HTS are quite similar, the ΔSPL for the CTS is not representative for the noise reduction and gives large deviations from the other two test sections. An AoA of 4° gives a maximum noise reduction of 5.8 dB and 4.6 dB, for 30 and 50 m/s respectively. For an AoA of 8° at 30 m/s (Figure 76c), a noise reduction of max. 3.2 is found. Noise reduction by serration for an AoA of 8° at 50 m/s can not be measured due to the higher background noise.

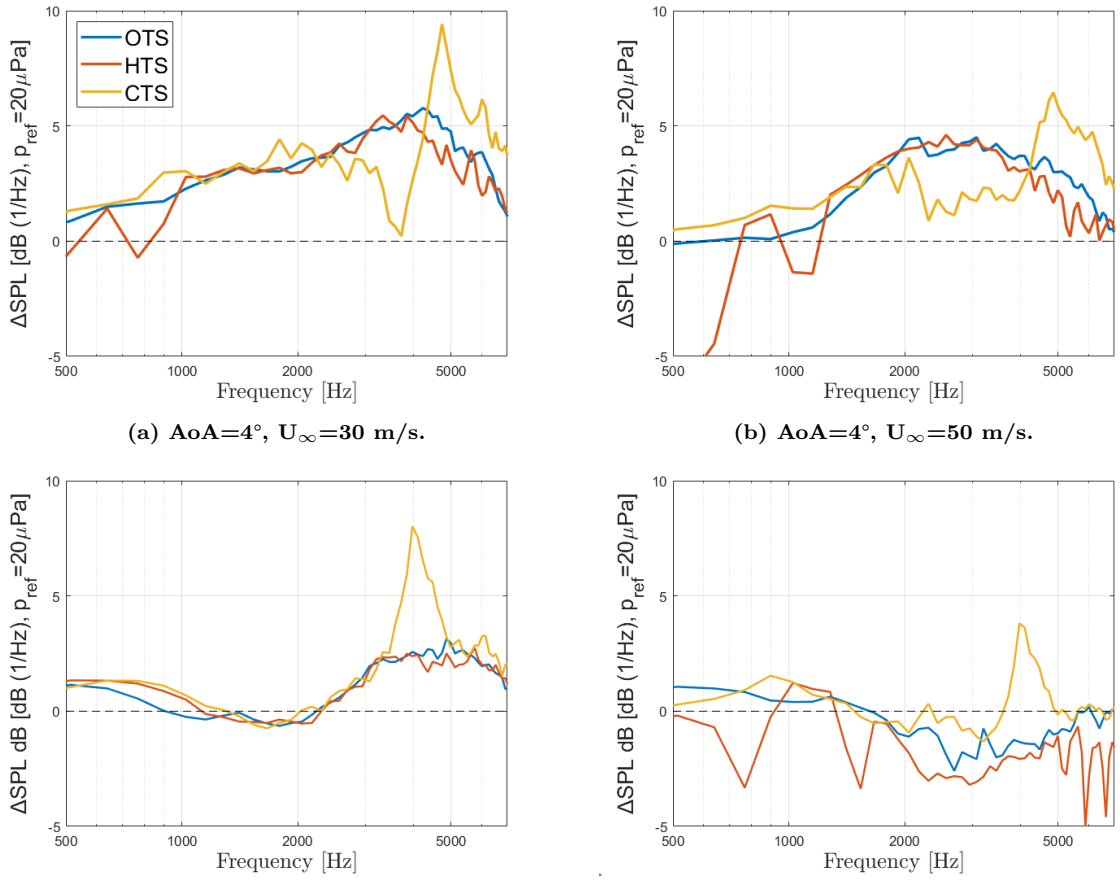

(a) AoA=4°, U_∞=30 m/s. **(b) AoA=4°, U_∞=50 m/s.**

(c) AoA=8°, U_∞=30 m/s. **(d) AoA=8°, U_∞=50 m/s.**

Figure 76: Integrated noise reduction levels of the trailing-edge serrations in one-third octave bands for the NACA63018.

PART IV, CONCLUSIONS, DISCUSSION AND RECOMMENDATIONS

5 Conclusions

Literature about fluid mechanics, airfoil aerodynamics, acoustics and airfoil noise, showed the theoretical fundamentals in aeroacoustic tests with airfoils. XFOIL simulations gave understanding about the aerodynamic principles, which is the basis for the prediction and understanding of airfoil self-noise. Literature review about existing airfoil noise reduction techniques, helped to design the most optimal way to reduce the background noise of the UT wind tunnel. With the beamforming technique and corresponding MATLAB algorithm, the experimentally assessed data was post processed and results could be obtained.

Results
Noise reduction techniques for the exit nozzle of the CTS are designed, fabricated, and their acoustic performance is assessed. This showed, that the exit nozzle serration and quarter ellipse both increased the background noise (Figure 53), doubting the physical phenomena of the unwanted noise source. A strong airflow through the turntables was assessed, generating noise. A seal was applied and the noise was reduced up to 12 dB at 2000 Hz, for higher frequencies the noise was reduced between 4-6 dB (OTS at U_∞=30 m/s).

After calibration of the CTS (PF to the FF), the *background noise* for the different test section types is compared (Figure 55). Single microphone spectra for the OTS and HTS are similar (<7000 Hz), the CTS gives way higher SPL values. A high frequency hump above 7000 Hz is present for the HTS and CTS, probably originating from the vibration of the Kevlar cloth and the gap between the panels. These noise sources also visible in the beamforming maps.

The first *trailing edge noise experiments* were related to the near field of the NACA0012 at AoA=0°. The wall pressure spectrum (Φ_p/p^2_{ref}) with corresponding coherence (γ^2) (Figure 58), showed overlap for all test section. So similar wall pressure characteristics are assessed, giving a good first indication that the far field noise coming from the trailing edge of the airfoil is similar in all test section types. The beamforming maps and integrated noise levels for the far field noise also showed similar values, only the CTS gave slightly lower values (Figure 60 and 59). All values were similar up to 1200 Hz and $St = 0.07$, the OTS and HTS overlap up to 8000 Hz and $St = 0.45$. Interaction of the airfoil with the windtunnel walls generating noise was assessed in the beamforming maps, especially present at higher flow velocities.

The influence of *serrations* on the far field noise of the NACA0012, showed a maximum noise reduction between 9.5-11.5 dB around 2000 Hz for the different test sections (AoA=0° and U_∞=30 m/s). Similar noise reduction levels for the Ser20 and Ser40 where found, noise was reduced between 500-5000 Hz. So despite the differences between the test section types, similar ΔSPL values are assessed experimentally. Regarding the beamforming maps of the CTS, line sources are visible at fewer frequencies especially at higher velocities. Resulting in a power integration over a region without TE noise, eventually leading to different ΔSPL at those frequencies. Slightly different noise reduction levels are obtained for the different test section types for AoA=0° and U_∞=50 m/s.

Noise levels for the NACA0012 with a Straight TE at multiple velocities, are post processed by *Mach scaling*. The fifth power law scaling behavior is associated with sources in the boundary layer. Overlap of the spectra with a Mach number scaling of the third and fourth power were obtained. So furthermore no conclusions can made from this analysis.

The far field noise *comparison of the airfoils* with a straight TE (OTS, AoA=0° and U_∞=30 m/s), showed that the NACA0012 was the loudest airfoil with a max. of 18.7 dB above the background noise. However the NACA63018 showed higher integrated SPL values at frequencies > 3000 Hz. Serrations reduced the noise for the NACA0012 and NACA0018 mainly for 500-5000 Hz, while for the NACA63018 noise was reduced up to 7300 Hz. Different wall pressure spectra are obtained for the airfoils, indicating a different development of the boundary layer (OTS, AoA=0° and U_∞=20 m/s).

Regarding the experiments with the *NACA63018 at non-zero AoA*, it was found that for the OTS the geometric - and effective AoA deviates the most, this due to the diverged airflow. Wall pressure spectra for the suction side overlapped for all test section types, for all AoA, at all velocities. Interesting wall characteristics were found for the pressure side, here small deviations between the test sections were assessed, probably origination from the differences in geometric AoA. Far field noise measurements at AoA=4° showed fewer line sources in the beamforming maps, especially for the CTS. It can be concluded that for the CTS this experiment can not define the TE noise for non-zero AoA properly for the relevant frequencies. Regarding the OTS and HTS, the noise reduction by serration (ΔSPL) can still be obtained at all velocities. Regarding AoA=8°, noise spectra could be obtained for the straight trailing edge. For the serration this resulted in poor results in the beamforming maps, here the background noise was higher than the serrated TE airfoil noise. Noise reduction levels could still be obtained for U_∞=30 m/s (OTS and HTS), for 50 m/s.

General

In conclusion, the influence of the test section types in trailing edge noise measurements is small. Background noise may differ, but is not influencing the results for the near field in any way (AoA=0°). Far field noise results at AoA=0° show minor deviations in the obtained noise reduction, mainly present in the CTS for higher free stream velocities. Regarding non-zero AoA, the test section influence is increased for both the near - and far field. The CTS is not suitable for far field noise measurements, with a serrated airfoil at non-zero AoA.

6 Discussion and Recommendations

Points for discussion are listed below.

- It must be noted that thesis is fully orientated towards the influence of the test section type for aeroacoustic trailing edge noise measurements of an airfoil. The influence of the test section can be completely different when for example, a 30P30N wing element is used in the UT wind tunnel.
- Calibration of the CTS (PF to FF), showed a rather noisy spectrum. This due to the fact that both configuration could not be measured at the same time, and it was not an ideal anechoic environment. Improving this calibration could result in more similar values for the CTS in comparison with the other two test sections.
- Beamforming maps for the HTS showed line sources originating from the gaps between the three Kevlar panels. Although this did not influenced the SPL and ΔSPL at these velocities (20, 30, 40 and 50 m/s), experiments with lower velocities could result in a power integration of this unwanted noise source, especially at the serrated airfoil.

Recommendations for follow-up research and experiments in the UT wind-tunnel are listed below.

- Regarding further acoustic noise measurements with airfoils in the UT wind tunnel. A better and quicker way to apply the seal on the turntables must be designed. This job was quite time consuming, the seal must be removed and placed again every time when a different AoA must be used.
- Coherence of the wall pressure spectra for the NACA63018 at non-zero AoA could be obtained. This would give more insight in the effect of the difference between the geometric - and effective AoA in the different test section types.
- Pressure coefficient data of the NACA63018 at non-zero AoA could be analyzed in more depth. Data is gathered for an effective AoA from 0° to 20° (increment = 1), for a natural - and forced transition. The influence of the test section type on the separation point for a natural transition could be assessed. Including the hysteresis effects.
- The StrTE noise spectra at multiple velocities, can be analyzed in more depth for the Mach scaling. It can be plotted versus the Helmholtz number to relate noise to certain aerodynamic mechanism.
- A comparison of the far field noise spectra with the prediction model from Brooks can me made.
- Surface pressure experiments for all airfoils at $U_\infty > 25$m/s could be executed (different microphones in the NACA0012 and NACA0018 are required). Wall pressure characteristics could be obtained, most likely resulting in similar spectra and overlapping coherence between the microphones.

References

[1] UnitedNations, "Paris agreement," pp. 1–27, 2015. DOI: https://unfccc.int/files/essential_background/convention/application/pdf/english_paris_agreement.pdf.

[2] InternationalEnergyAgency, "Onshore wind, more efforts needed.," 2020. DOI: https://www.iea.org/reports/onshore-wind.

[3] WindEurope, "Wind energy in europe in 2019, trends and statistics," pp. 1–24, February 2020. DOI: https://windeurope.org/data-and-analysis/product/wind-energy-in-europe-in-2019-trends-and-statistics/.

[4] J. F. Manwell and J. G. McGowan, *Wind energy explained: Theory, design and application*. John Wiley Sons Ltd, 2009, ISBN: 978-0-470-01500-1.

[5] H. Abbot and A. E. von Doenhoff, *Theory of Wing Sections*. Dover Publications Inc., 1959, ISBN: 486-60586-8.

[6] S. Oerlemans, "Wind turbine noise: Primary noise sources," *National Aerospace Laboratory (NLR)*, no. NLR-TP-2011-066, pp. 1–57, April 2015. DOI: https://reports.nlr.nl/xmlui/bitstream/handle/10921/117/TP-2011-066.pdf.

[7] A. J. Millican, "Bio-inspired trailing edge noise control: Acoustic and flow measurements," 2017.

[8] R. . Fox and A. T. McDonald, *Introduction to fluid mechanics*. John Wiley Sons, New York, NY, USA., 1988, ISBN: 9780511800955.

[9] G. K. Batchelor, *An Introduction to Fluid Dynamics*. Cambridge University Press, 1967, ISBN: 9780511800955.

[10] N. P. Kruyt, "Fluid mechanics of turbomachines 2, lecture notes," 2019, April 23. [Online]. Available: https://canvas.utwente.nl/courses/4902/pages/lecture-notes?module_item_id=143475.

[11] F. M. White, *Viscous fluid flow, 3rd edition*. McGraw-Hill, 2007, ISBN: 007-124493X.

[12] T. F. Brooks, D. S. Pope, and M. A. Marcolini, "Airfoil self-noise and prediction," *NASA Reference Publication*, no. 1218, pp. 1–146, 1989. DOI: https://ntrs.nasa.gov/citations/19890016302.

[13] Y. de Valk, "Msc thesis: A novel construction of wind tunnel models for wind energy applications," no. EFD-331, pp. 1–105, December 2019. DOI: http://essay.utwente.nl/81061/.

[14] J. D. Anderson, *Fundamentals of Aerodynamics*. McGraw-Hill Education, 1991, ISBN: 0-07-001679-8.

[15] C. H. Hansen, C. J. Doolan, and K. L. Hansen, *Wind Farm Noise: Measurement, Assessment and Control*. John Wiley and Sons Ltd, 2017, ISBN: 9781118826065.

[16] S. Glegg and W. Devenport, *Aeroacoustics of Low Mach Number Flows*. Academic Press, 2017, ISBN: 978-0-12-809651-2.

[17] D. T. Blackstock, *Fundamentals of Physical Acoustic*. John Wiley and Sons Ltd, 2000, ISBN: 9780471319795.

[18] P. J. Matuszyk, L. F. Demkowicz, and C. Torres-Verdin, "Solution of coupled acoustic–elastic wave propagation problems with anelastic attenuation using automatic hp-adaptivity," *Computer Methods in Applied Mechanics and Engineering,*, no. 213–216, pp. 299–313, 2012. DOI: https://doi.org/10.1016/j.cma.2011.12.004.

[19] T. F.Brooks, Schlinker, and H. Robert, "Progress in rotor broadband noise research," *NASA Reference Publication*, no. 4, vol. 7, pp. 287–307, 1983. DOI: https://www.researchgate.net/publication/23860113_Rotor_Broadband_Noise_Prediction_with_Comparison_to_Model_Data.

[20] L. A. Errasquin, "Airfoil self-noise prediction using neural networks for wind turbines," 2009.

[21] M. Drela, "Xfoil: An analysis and design system for low reynolds number airfoils.," 1989.

[22] M. P. J. Sanders, L. Botero-Bolivar, L. D. de Santana, and C. H. Venner, "Airfoil trailing edge noise measurements in an open-jet, hard-wall and kevlar®-wall test section: A benchmark exercise.," pp. 1–10, 2020.

[23] M. Gruber, P. Joseph, and T. Chong, "On the mechanisms of serrated airfoil trailing edge noise reduction," *17th AIAA/CEAS Aeroacoustics Conference*, no. AIAA 2011-2781, 2011. DOI: https://arc.aiaa.org/doi/abs/10.2514/6.2011-2781.

[24] F. Avallone, W. van der Velden, and D. Ragni, "Benefits of curved serrations on broadband trailing-edge noise reduction," *Journal of Sound and Vibration*, no. ISSN 0022-460X, 2017. DOI: https://doi.org/10.1016/j.jsv.2017.04.007..

[25] P. Kholodov and S. Moreau, "Optimization of trailing-edge serrations with and without slits for broadband noise reduction," *Journal of Sound and Vibration*, vol. Volume 490, no. ISSN 0022-460X, pp. 1–27, 2020. DOI: https://doi.org/10.1016/j.jsv.2020.115736..

[26] D. J. Moreau, L. A. Brooks, and C. J. Doolan, "On the noise reduction mechanism of a flat plate serrated trailing edge at low-to-moderate reynolds number," *18th AIAA/CEAS Aeroacoustics Conference (33rd AIAA Aeroacoustics Conference)*, no. AIAA 2012-2186, pp. 1–21, June 2012. DOI: file:///C:/1.\%20School/5.\%20Master\%20Thesis/3.Literature/Other/NoiseReductionTechniques/Moreau_AIAA_12.pdf.

[27] C. A. Leon, R. M. Martinez, D. Ragni, S. Pröbsting, F. Avallone, A. Singh, and J. Madsen, "Trailing edge serrations, effect of their flap angle on flow and acoustics," *7th International Conference on Wind Turbine Noise*, pp. 1–27, 2017.

[28] E. Llorente and D. Ragni, "Trailing-edge serrations effect on the performance of a wind turbine," *Renewable Energy*, 2019.

[29] A. Afshar, M. Azarpeyvand, A. A. Dehghan, and M. Szőke, "Effects of streamwise surface treatments on trailing edge noise reduction," *Researchgate*, 2017.

[30] I. A. Clark, W. N. Alexander, and W. Devenport, "Bioinspired trailing-edge noise control," *AIAA JOURNAL*, vol. 55, no. 3, March 2017.

[31] A. Finez, E. Jondeau, and M. Roger, "Broadband noise reduction with trailing edge brushes," *Researchgate, American Institute of Aeronautics and Astronautics*, 2010.

[32] M. Herr and W. Dobrzynsky, "Experimental investigations in low noise trailing edge design," *AIAA Paper No. 2004-2804*, 2004.

[33] M. Herr, "Design criteria for low-noise trailing edges," *AIAA Paper No. 2007-3470*, 2007.

[34] R. Atiénzar-Navarro, M. Bonet-Aracil, J. Gisbert-Payá, R. del Rey, and R. Picó, "Sound absorption of textile fabrics doped with microcapsules," *Applied Acoustics, Elsevier*, vol. 164, 2020.

[35] P. Segura-Alcaraz, J. Segura-Alcaraz, I. Montava, Marilés, and Bonet-Aracil, "The use of fabrics to improve the acoustic absorption: Influence of the woven fabric thread density over a nonwoven," *AUTEX Research Journal*, 2018.

[36] T. Kudo, K. Maeda, and M. Nishimura, "Techniques of reducing aerodynamic noises in a 3/4 open jet wind tunnel," *Journal of Environment and Engineering*, vol. 4, no. 2, 2009.

[37] C. Teruna, F. Avallone, D. Casalino, and D. Ragni, "Numerical investigation of leading edge noise reduction on a rod-airfoil configuration using porous materials and serrations," *Journal of Sound and Vibration*, 2020.

[38] L. D. de Santana, M. P. Sanders, C. H. Venner, and H. W. Hoeijmakers, "The utwente aeroacoustic wind tunnel upgrade," p. 3136, 2018.

[39] L. D. de Santana, "Fundamentals of acoustic beamforming," *Lecture Series Von Karman Institute for Fluid Dynamics*, p. 26, 2016-2017.

[40] R. Merino-Martınez, P. Sijtsma, and M. Snellen, "Inverse integration method for distributed sound sources," 2018.

[41] Knowles, "Frequency response and latency of mems microphones: Theory and practice," 2017. DOI: https://www.knowles.com/docs/default-source/default-document-library/frequency-response-and-latency-of-mems-microphones---theory-and-practice.pdf?sfvrsn=4.

Appendices

A Mathematical Notation

The **magnitude** of a 3D-vector vector $\underline{a} = (a_x, a_y, a_z)^T$ can be defined as,

$$\|\underline{a}\| = \sqrt{a_x^2 + a_y^2 + a_z^2} \tag{A.0.1}$$

The **inner product** of two 3D vectors $\underline{a} = (a_x, a_y, a_z)^T$ and $\underline{b} = (b_x, b_y, b_z)^T$ is a scalar and is defined by (A.0.2). Where θ is the angle between the two vectors. $\underline{a} \cdot \underline{b} = 0$ when the vectors are perpendicular (or orthogonal), the inner product is also called the dot product. Here $\|\underline{b}\| \cos(\theta)$ is the part of $\underline{b}$ in the direction of $\underline{a}$ ($\underline{b}_a$). Multiplying this by $\underline{a}$ and this gives the representation of $\underline{b}$ in the direction of $\underline{a}$, this is the inner product. This gives an indication of how much these two vectors are alike, $\underline{a} \cdot \underline{b} = 0$ when the vectors are orthogonal.

$$\underline{a} \cdot \underline{b} = a_x b_x + a_y b_y + a_z b_z = \|\underline{a}\| \|\underline{b}\| \cos(\theta) \tag{A.0.2}$$

The cross product or **outer product** of these two vectors $\underline{a}$ and $\underline{b}$ is a quantity defined by (A.0.3). The outer product is perpendicular to both vectors, and its magnitude can be given as $\|\underline{a}\| \|\underline{b}\| \sin(\theta)$. The magnitude of the cross product is the same as the area of the parallelogram of $\underline{a}$ and $\underline{b}$. It gives an indication of how much these two vectors differ from each other, $\underline{a} \times \underline{b} = 0$ when the vectors are parallel.

$$\underline{a} \times \underline{b} = \begin{bmatrix} a_y b_z - a_z b_y \\ a_z b_x - a_x b_z \\ a_x b_y - a_y b_x \end{bmatrix} \tag{A.0.3}$$

The **divergence** of a vector field $\underline{F}(x, y, z, t) = [F_x(x, y, z, t), F_y(x, y, z, t), F_z(x, y, z, t)]^T$ gives an insight in the difference between the inflow an outflow of the particles in a specified region. The particles diverge when $\nabla \cdot \underline{F} > 0$, when converging $\nabla \cdot \underline{F} < 0$ is true, when the inflow equals the outflow $\nabla \cdot \underline{F} = 0$. The divergence is a scalar field defined by,

$$\nabla \cdot \underline{F} = \left[\frac{\partial F_x}{\partial x} + \frac{\partial F_y}{\partial y} + \frac{\partial F_z}{\partial z} \right] \tag{A.0.4}$$

The **gradient** of a scalar field $p(x, y, z, t)$ gives you the partial derivatives of the field in all directions, and is mathematically defined as,

$$\nabla p = \begin{bmatrix} \dfrac{\partial p}{\partial x} \\ \dfrac{\partial p}{\partial y} \\ \dfrac{\partial p}{\partial z} \end{bmatrix} \tag{A.0.5}$$

The **rotation** or curl of a vector field $\underline{F}$, gives an indication of the curl/rotation of the particles in a specified region in $\underline{F}$ A rotation in counterclockwise direction gives $\nabla \times F > 0$, a clockwise rotation is defined as $\nabla \times F < 0$, and no rotation gives $\nabla \times F = 0$). This can be identified as,

$$\nabla \times F = \begin{bmatrix} \dfrac{\partial F_z}{\partial y} - \dfrac{\partial F_y}{\partial z} \\ \dfrac{\partial F_z}{\partial x} - \dfrac{\partial F_x}{\partial z} \\ \dfrac{\partial F_x}{\partial y} - \dfrac{\partial F_y}{\partial x} \end{bmatrix} \tag{A.0.6}$$

B Airfoils self-noise prediction by Brooks

In this section of the appendix additional information and equations for the prediction of the airfoil self-noise by Brooks is given.

Strouhal definitions
The experimentally determined Strouhal definitions are,

$$St_1 = 0.02M^{-0.6} \tag{B.0.1}$$

$$\overline{St_1} = \frac{St_1 + St_2}{2} \tag{B.0.2}$$

$$St_2 = St_1 \times \begin{cases} 1 & \alpha < 1.33° \\ 10^{0.0054(\alpha-1.33)^2} & 1.33° \leq \alpha \leq 12.5° \\ 0 & \alpha > 12.5° \end{cases} \tag{B.0.3}$$

Brooks found, that the ratio of the Strouhal number at multiple positions on the chord, can be used in the prediction of the Sound Pressure Levels for the TBL-TE noise (and other self-noise types).

Directivity
For low frequencies the behaviour can be represented as a pure dipole (Figure 19b), relating to the equation in (B.0.5). For a baffled dipole Equation (B.0.4) can be used.

$$\overline{D}_h = \frac{2\sin^2\left(\frac{\theta_r}{2}\right) sin^2\phi_r}{(1 + M\cos\theta_r)[1 + (M - M_c)\cos\theta_r]^2} \tag{B.0.4}$$

$$\overline{D}_l = \frac{2\sin^2\theta_r sin^2\phi_r}{(1 + M\cos\theta_r)^4} \tag{B.0.5}$$

Spectral shape
The *spectral shape* function (A) depends on the Reynolds number and is determined by an interpolation of the curves A_{min} (B.0.6) and A_{max} (B.0.6). This spectral shape function indicates 'the amount' of presence, for a spectrum of frequencies, in the noise.

$$A_{min}(a) \begin{cases} \sqrt{67.552 - 886.788a^2} - 8.219 & (\text{a} < 0.204) \\ -32.665a + 3.981 & (0.204 \leq \text{ a } \leq 0.244) \\ -142.795a3 + 103.656a2 - 57.757a + 6.006 & (\text{a} > 0.244) \end{cases} \tag{B.0.6}$$

$$A_{max}(a) \begin{cases} \sqrt{67.552 - 886.788a^2} - 8.219 & (\text{a} < 0.13) \\ -15.901a + 1.098 & (0.13 \leq \text{ a } \leq 0.321) \\ -4.669a^3 + 3.491a^2 - 16.699a + 1.149 & (\text{a} > 0.321) \end{cases} \tag{B.0.7}$$

Where a is the absolute value of the logarithm of the ratio of Strouhal number, where $St = St_p$ or St_s, to the peak value $St_{peak} = St_1, \overline{St_1}$, or St_2. When the AoA is zero (B.0.9) is used.

$$a = |\log(St/St_{peak})| \tag{B.0.8}$$

$$a_0(Re) \begin{cases} 0.57 & (Re < 9.52x10^4) \\ (-9.57x10^{-13})(Re - 8.57x10^5)^2 + 1.13 & (9.52x10^4 \leq Re \leq 8.57x10^5) \\ 1.13 & (Re > 8.57x10^5) \end{cases} \tag{B.0.9}$$

An interpolation factor $A_R(a_O)$ is determined from,

$$A_R(a_0) = \frac{-20 - A_{min}(a_0)}{A_{max}(a_0) - A_{min}(a_0)} \tag{B.0.10}$$

The spectrum shape A can now be evaluated for any frequency by computing St and the corresponding a, and using the interpolation factor $A_R(a_0)$. This spectrum shape is given in Figure 77a and results in,

$$A(a) = A_{min}(a) + A_R(a_0)[A_{max}(a) - A_{min}(a)] \tag{B.0.11}$$

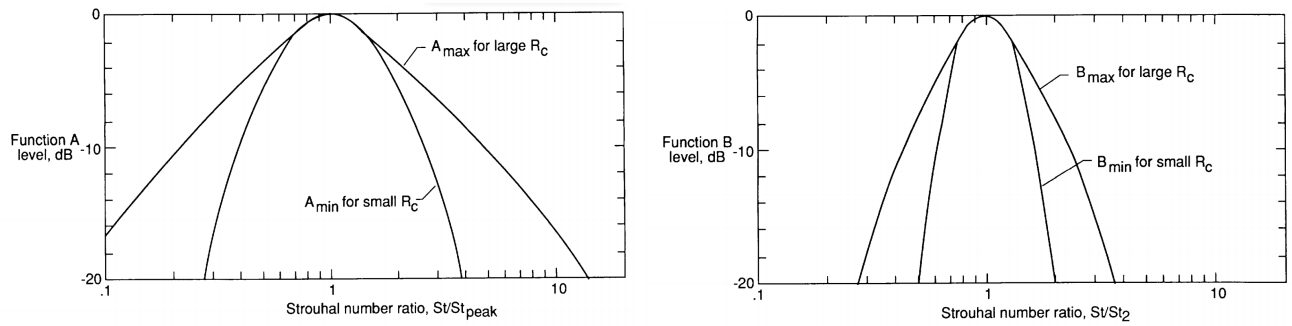

(a) Spectrum shape A. **(b)** Spectrum shape B.

Figure 77: Spectrum shape function for TBL-TE noise [12].

The spectral shape B related to SPL_α in (2.7.4), is build up in a similar way compared to A. Namely by an interpolation of the two curves B_{min} and B_{max},

$$B_{min}(b) \begin{cases} \sqrt{16.888 - 886.788b^2} - 4.109 & (\text{b} < 0.13) \\ -83.607b + 8.138 & (0.13 \leq \text{ b } \leq 0.145) \\ -817.810b^3 + 355.210b^2 - 135.024b + 10.619 & (\text{b} > 0.145) \end{cases} \tag{B.0.12}$$

$$B_{max}(b) \begin{cases} \sqrt{16.888 - 886.788b^2} - 4.109 & (\text{b} < 0.10) \\ -31.330b + 1.854 & (0.10 \leq \text{ b } \leq 0.187) \\ -80.541b^3 + 44.174b^2 - 39.381b + 2.344 & (\text{b} > 0.187) \end{cases} \tag{B.0.13}$$

where

$$b = |\log(St_s/St_2)| \tag{B.0.14}$$

The spectral shape B for intermediate values of Re have horizontal axis intercepts at -20 dB, shown in Figure 77b. Regarding values for $\alpha = 0°$,

$$b_0(Re) \begin{cases} 0.30 & (Re < 9.52x10^4) \\ (-4.48 \times 10^{-13})(Re - 8.57 \times 10^5)^2 + 0.56 & (9.52 \times 10^4 \leq Re \leq 8.57 \times 10^5) \\ 0.56 & (Re > 8.57 \times 10^5) \end{cases} \tag{B.0.15}$$

With the interpolation factor $B_R(b_o)$ defined in (B.0.16), and thus the final solution for $B(b)$ given in (B.0.17).

$$B_R(a_0) = \frac{-20 - B_{min}(a_0)}{B_{max}(b_0) - B_{min}(b_0)} \tag{B.0.16}$$

$$B(b) = B_{min}(b) + B_R(b_0)[B_{max}(b) - B_{min}(b)] \tag{B.0.17}$$

Empirical constants

The amplitude functions K, are used to correspond the SPL results from the executed empirical experiments with the output of the noise predicting SPL equations. K_1 is introduced to eliminate the dependency of the Reynolds number. This scaling factor requires a level adjustment (-3 dB) for consistency, and is defined as,

$$K_1 = \begin{cases} -4.31\log(Re) + 156.3 & (Re < 2.47 \times 10^5) \\ -9.0\log(Re) + 181.6 & (2.47 \times 10^5 \leq Re \leq 8.0 \times 10^5) \\ 128.5 & (Re > 8.0 \times 10^5) \end{cases} \tag{B.0.18}$$

The term ΔK_1 is an empirical level adjustment for the pressure-side contribution for non zero AoA. This is given by,

$$\Delta K_1 = \begin{cases} \alpha[1.43\log(Re_{\delta_p^*}) - 5.29] & (Re_{\delta_p^*} < 5000) \\ 0 & (R_{\delta_p^*} > 5000) \end{cases} \tag{B.0.19}$$

The amplitude function K_2 relates to SPL_α, and uses the function $K_2(K_1, M, \alpha)$. Resulting in,

$$K_2 = K_1 + \begin{cases} -1000 & (\alpha < -\gamma_0 - \gamma) \\ \sqrt{\beta^2 - (\beta/\gamma)^2(\alpha - \gamma_0)^2} + \beta_0 & (\gamma_0 - \gamma \leq \alpha \leq -\gamma_0 + \gamma) \\ -12 & (\alpha > +\gamma_0\gamma) \end{cases} \tag{B.0.20}$$

where

$$\left.\begin{array}{ll} \gamma = 27.094M + 3.31 & \gamma_0 = 23.43M + 4.651 \\ \beta = 72.65M + 10.74 & \beta_0 == -34.19M - 13.82 \end{array}\right\} \tag{B.0.21}$$

The scaled SPL for the amplitude functions K_1 are given in Figure 78a. This elimination of the Reynolds dependency, results in the solid line. First the line decays, which looks linear in this logarithmic plot ($1 \cdot 10^4 - 3 \cdot 10^5$). Around Re $= 3 \cdot 10^5$, the line drops even more, after $Re = 10^6$ the SPL values influenced by K_1 become rater constant. The other amplitude function (K_2), related to the AoA is given in Figure 78. The most interesting thing happens when $AoA > 12°$, where the line becomes constant. This means that after this critical AoA the SPL does not have any large changes due tot the angle of attack.

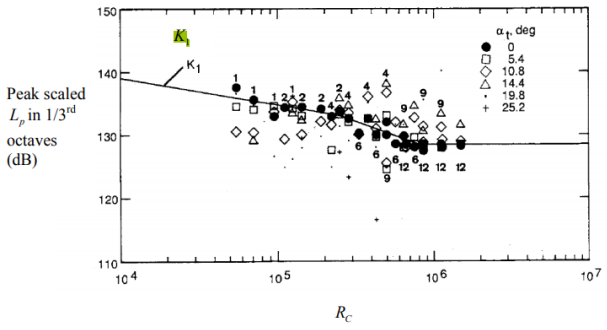

(a) Peak scaled SPL, with amplitude functions K_1.

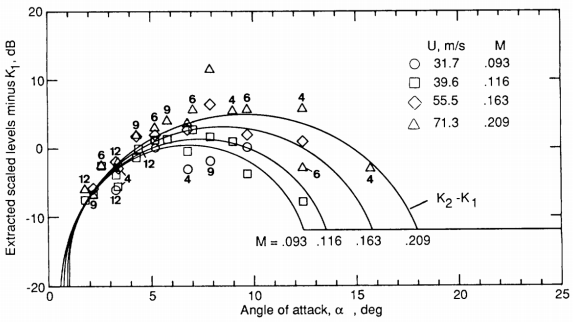

(b) K_2, expressed as $K_2 - K_1$.

Figure 78: Amplitude functions for the SPL_{TBL-TE} [12].

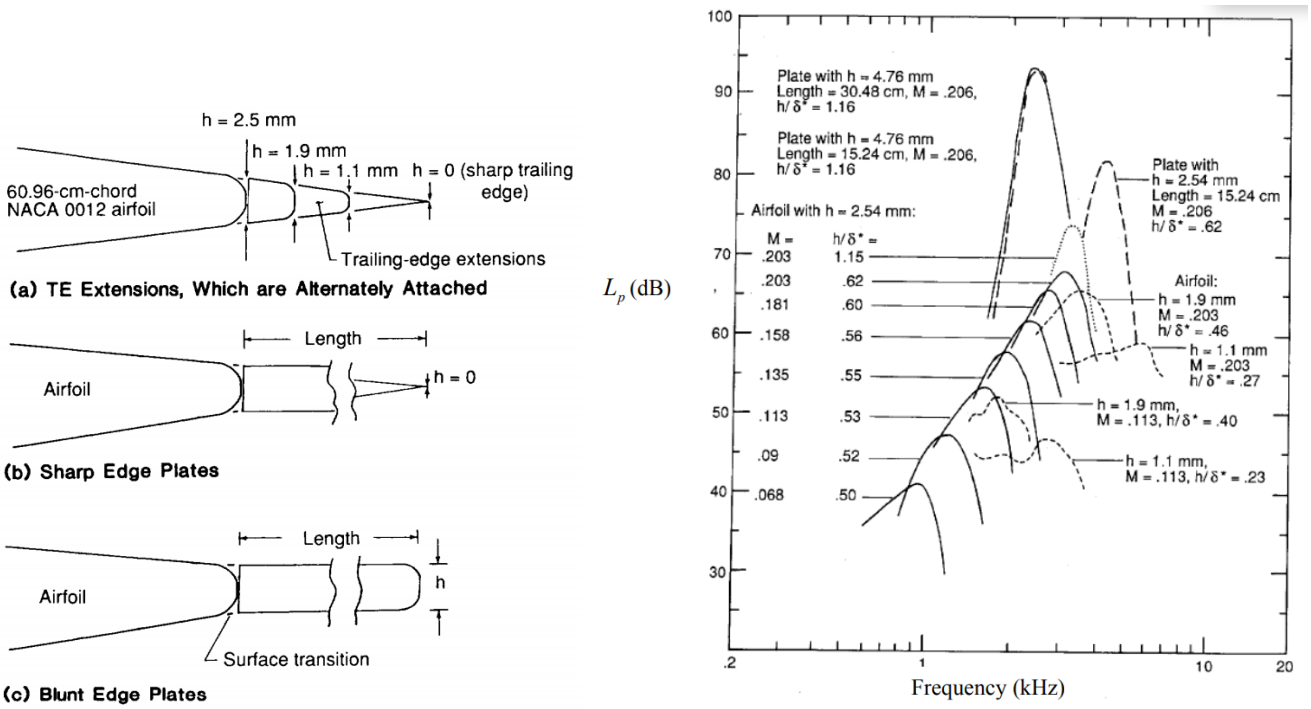

(a) Different TE. **(b)** SPL

Figure 79: Trailing-Edge-Bluntness-Vortex Shedding Noise [12].

C Microphone Array Hardware Configuration

Table 7: Hardware Configuration for the two microphone arrays.

OTS/HTS

Microphone Index	GRAS, serial number	DAQ Port
51	313900	1
38	313858	2
12	313843	3
17	313896	4
30	313887	5
64	313860	6
43	313875	7
22	313876	8
4	313857	9
9	313873	10
1	313868	11
14	313905	12
6	313869	13
3	313884	14
5	313849	15
8	313863	16
44	313891	17
52	313874	18
31	313902	19
18	313888	20
39	313881	21
60	313848	22
26	313844	23
47	313878	24
13	313904	25
34	313846	26
21	313890	27
55	313870	28
42	313847	29
29	313854	30
63	313855	31
50	313899	32
56	313901	33
35	313898	34
48	313879	35
27	313842	36
19	313885	37
40	313877	38
53	313845	39
32	313866	40
49	313871	41
57	313872	42

CTS

Microphone Index	GRAS, serial number	DAQ Port
55	313859	1
42	313882	2
50	313858	3
34	313849	4
47	313868	5
60	313857	6
21	313843	7
30	313897	8
59	313877	9
51	313866	10
46	313855	11
38	313870	12
43	313845	13
56	313847	14
35	313861	15
48	313905	16
26	313896	17
44	313853	18
31	313844	19
18	313848	20
13	313903	21
10	313871	22
5	313856	23
57	313902	24
58	313874	25
54	313881	26
37	313888	27
16	313850	28
8	313900	29
45	313865	30
24	313893	31
52	313895	32
33	313880	33
29	313852	34
17	313854	35
62	313904	36
41	313885	37
20	313901	38
12	313898	39
9	313899	40
49	313891	41
22	313889	42

Microphone Index	GRAS, serial number	DAQ Port
36	313886	43
15	313865	44
7	313897	45
23	313851	46
10	313903	47
2	313859	48
46	313850	49
20	313853	50
54	313892	51
33	313894	52
59	313895	53
25	313882	54
41	313893	55
28	313856	56
45	313889	57
24	313861	58
11	313883	59
16	313864	60
37	313880	61
58	313852	62

Microphone Index	GRAS, serial number	DAQ Port
28	313876	43
7	313873	44
4	313846	45
14	313875	46
27	313869	47
39	313890	48
36	313851	49
23	313892	50
15	313860	51
2	313878	52
25	313842	53
1	313863	54
3	313894	55
6	313864	56
40	313884	57
53	313887	58
19	313879	59
32	313886	60
11	313872	61
61	313883	62